Università degli Studi di Messina

DIPARTIMENTO DI SCIENZE MATEMATICHE E INFORMATICHE,
SCIENZE FISICHE E SCIENZE DELLA TERRA

DOTTORATO DI RICERCA IN FISICA (XXXV CICLO)
SSD FIS/04

Event multiplicity dependence production of $K^*(892)^{\pm}$ resonance in pp collisions at $\sqrt{s} = 13$ TeV with the ALICE detector at the LHC

Author:
Antonina Rosano

Supervisor:
Prof. **Giuseppe Mandaglio**
Dr.ssa **Angela Badalà**
Prof.ssa **Marina Trimarchi**

Coordinatore del dottorato:
Prof.ssa **Vincenza Crupi**

Anno accademico 2021/2022

Contents

Introduction

This thesis reports first measurements of $\mathrm{K}^{*}(892)^{\pm}$ produced in pp collisions at $\sqrt{s} = 13$ TeV as function of the event multiplicity. The results include, for each multiplicity class considered, the differential transverse momentum (p_{T}) spectrum, the mean transverse momentum $\langle p_{\mathrm{T}} \rangle$, the integrated yield ($\mathrm{d}N/\mathrm{d}y$), and the ratio of the $\mathrm{K}^{*}(892)^{\pm}$ yield to the $\mathrm{K}^{0}_{\mathrm{S}}$ one. The $\mathrm{K}^{*}(892)^{\pm}$ has been studied at the same energy and compared with the neutral K^{*} resonance production, as well as with results from different event generators.

Quantum ChromoDynamics (QCD) is the theory that describes the strong interaction between quarks and gluons. Because of the non-Abelian nature of the theory, the running coupling constant $\alpha_s(|q^2|)$ permits to identify two different regimes of the strong interaction: the perturbative domain and the non-perturbative one. The strength of the strong coupling decreases with increasing energy or momentum transfer q^2, and vanishes at asymptotically high energies. In the limit of very large q^2, quarks and gluons can be considered "free" (asymptotic freedom), allowing perturbative calculations. On the contrary, the confinement of the hadronic matter cannot be mathematically proven from first principles because of its non-perturbative nature. The Higgs mechanism has been essential in explaining the mass generation process, triggered by the spontaneous symmetry breaking. The question of the hadron mass generation can find an explanation in the chiral symmetry breaking process. Lattice QCD calculations suggest that for critical values of temperature and energy density the chiral symmetry can be restored, investigating the nature of the crossover from the confined chiral-symmetry-broken phase to the deconfined chiral-symmetry-restored phase. This deconfined state of matter is called Quark Gluon Plasma (QGP) and can be recreated in heavy ion collisions at the RHIC and LHC energies. The QGP study is interesting not only as a tool to probe QCD theory, but also in order to

investigate first instants of the early Universe, where at about 1 μs from the Big Bang, this state of matter should be present. Therefore the study of the QGP is necessary to solve the issues of the onset of confinement and the hadron mass generation as well as to understand the physics of strongly interacting matter under extreme conditions of temperature and energy density, as in the case of the early Universe. This can be done experimentally with ultra-relativistic heavy-ion collisions, where the suitable conditions for QGP formation are reached. Though recently, hints of collective effects and of features typical of heavy-ion collisions (such as strangeness enhancement or the suppression of the ratios of short-lived resonances to their non-resonant hadronic states) have been observed also in high multiplicity pp and p–Pb collisions.

ALICE (A Large Ion Collider Experiment) is one of the large CERN experiments installed at the Large Hadron Collider (LHC). The ALICE detector is mainly designed to study the physics of heavy-ion collisions at ultra-relativistic energies, collecting data also from pp and p–Pb collisions in order to establish a reference baseline. However recent results obtained from data collected by ALICE in small collision systems have sparked the interest not only as a trivial benchmark but also for the possible physical meaning hidden behind, as for example in the case of hadronic resonances analyses.

Short-lived hadronic resonances have been shown to be good probes to investigate the late-stage evolution of ultra-relativistic heavy-ion collisions. Their lifetimes are comparable with the time scale of the fireball generated in these collisions, therefore they are sensitive to the competing re-scattering and regeneration effects occurring during the hadronic phase, which modify particle momentum distributions and yields after hadronization. Recent measurements of resonance production in high-multiplicity proton-proton (pp) and proton-lead (p–Pb) collisions have shown the onset of phenomena typical of heavy-ion (Pb–Pb) collisions even in those smaller collision systems. In particular, there are hints of suppression of the $\mathrm{K}^{*}(892)^{0}/\mathrm{K}$ ratio with increasing charged-particle multiplicity, even though not very significant due to large systematic uncertainties. The study of $\mathrm{K}^{*}(892)^{\pm}$ production in pp collisions can be used as a baseline to study the Pb–Pb collisions at the LHC energy and to provide a reference for tuning event generators such as PYTHIA and EPOS-LHC. In addition it can provide further evidence to confirm the K^{*0} observed trend and even improve it reaching higher precision.

This thesis consists of three macro parts:

- **Part I: QUARK GLUON PLASMA**. A general description of the physics context is given in this part, with an introduction to the QCD and to the concept of the QGP. The description continues with some information about the peculiar characteristics of heavy-ion collision with the time evolution of the system created. Then the importance to study the resonances production as a tool for characterizing the properties of the hadronic phase is also discussed. Some of the main event generators and models as (PYTHIA and EPOS-LHC) are described, concluding with some new interesting results observed in small systems.

- **Part II: A LARGE ION COLLIDER EXPERIMENT**. In this part the description of the detection capabilities of the ALICE apparatus are provided, with a specific focus on the main sub-detectors involved in resonances reconstruction. In addition further information on the operational chain necessary to convert the signals from the detector into data suitable for the analysis procedure and on the tools provided by the ALICE collaboration are also presented.

- **Part III: MEASUREMENT OF $\mathrm{K}^{*}(892)^{\pm}$ PRODUCTION**. The multiplicity dependent analysis of $\mathrm{K}^{*\pm}$ resonance production in pp collisions at $\sqrt{s} = 13$ TeV is deeply described in this part. The event selection, the method used to estimate the raw yields and the necessary corrective factors, and the procedure followed to estimate the systematic uncertainties are reported here. Then the physics results obtained with the measurements of the $\mathrm{K}^{*\pm}$ differential p_{T} spectra, $\langle p_{\mathrm{T}} \rangle$, $\mathrm{d}N/\mathrm{d}y$, and ratios to $\mathrm{K}^{0}_{\mathrm{S}}$ as a function of charged-particle multiplicity are described. Finally the comparison with K^{*0} measurements obtained in the same collision system and energy as well as with different model predictions is also discussed.

Part I

Quark Gluon Plasma

Chapter 1

Quantum Chromodynamics

Quantum Chromodynamics (QCD) [1] is a gauge field theory that describes the strong interactions of quarks and gluons. Mathematically, QCD is a Yang-Mills non-Abelian theory, which has a SU(3) symmetry group where quarks are organized in triplets. Quantic numbers of QCD are flavour (up, down, strange, charm, top, and bottom) and colour (red, green, and blue). Gluons carry the colour charge, they have not flavour, but eight different colour states. Strong interaction is described by the α_s constant, its value expresses the force of the strong coupling between quarks and gluons. This constant depends on the transferred momentum q^2. For very small distances and high q^2 values (> 200 MeV), the inter-quark coupling decreases, vanishing asymptotically. In the limit of very large q^2, quarks can be considered "free" (asymptotic freedom), allowing perturbative calculations. On the other hand, the inter-quark coupling at large distances increases to a level that it is impossible to isolate individual quarks from hadrons (confinement). Therefore the value of α_s is not constant and it is usually defined as *running coupling constant*. Confinement cannot be mathematically proven from first principles because of its non-perturbative nature, but it is verified by lattice QCD calculations (l-QCD) [2]. The trend of α_s is shown in Fig. 1.1.

A first order perturbative QCD calculation gives:

$$\alpha_s(|q^2|) = \frac{\alpha_0}{1+\alpha_0}\frac{33-2n}{12\pi}\ln\frac{|q^2|}{\mu^2} \tag{1.1}$$

where n is the number of flavours, μ the energy scale and α_0 the constant calculated at μ energy.
Therefore, in the limit of high energy values, the QCD theory predicts the

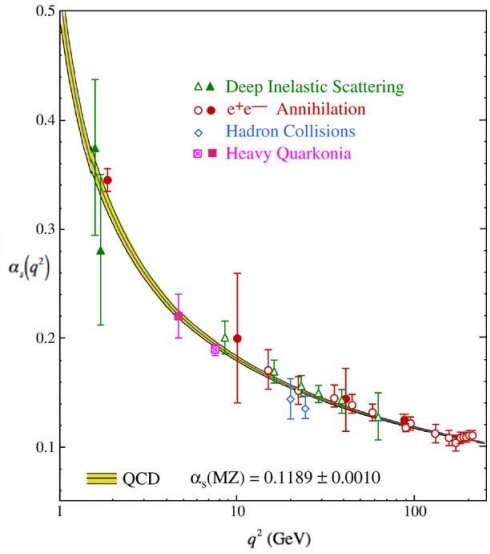

Figure 1.1: α_s as a function of the transferred momentum q^2.

progressive reduction of the strength of the strong force and the subsequent deconfinement of quarks and gluons. Matter will be in a new state of free quarks and gluons, the so called Quark Gluon Plasma (QGP).
An interesting aspect to consider when discussing the strong force is the *hadron mass generation mechanism*. It refers to the difference between the mass of a hadron and the total mass of its constituent quarks: the sum of the quarks bare masses is much lower than the hadron mass (e.g. in the case of a proton or neutron, only about 1% of the hadron mass is reached by simply summing *up* and *down* quark masses). This phenomenon finds an explanation in the *chiral symmetry breaking* process.

1.1 Chiral Symmetry Breaking

In the limit of massless quarks the QCD Lagrangian density can be written as:

$$\mathcal{L} = -\frac{1}{4} F^a_{\mu\nu} F^{a\mu\nu} + \sum_{f=1}^{6} \overline{\Psi}_f (i\gamma^\mu D_\mu) \Psi_f \tag{1.2}$$

where

$$D_\mu = \partial_\mu + ig\frac{\lambda^a}{2}A^a_\mu \tag{1.3}$$

is the covariant derivative in which λ_a are the 8 generators of the SU(3) group (the 3×3 Gell-Mann matrices) and

$$F^a_{\mu\nu} = \partial_\mu A^a_\nu - \partial_\nu A^a_\mu + g f^{abc} A^b_\mu A^c_\nu \tag{1.4}$$

is the gluon field strength tensor in which f^{abc} are the structure constants of SU(3). This term is very different from the QED force field tensor ($F_{\alpha\beta} = \partial_\alpha A_\beta - \partial_\beta A_\alpha$) due to the fact that SU(3) is a non-Abelian group. The key difference is that the gluon field strength has extra terms which lead to self-interactions between gluons and to the asymptotic freedom. The Ψ represents for each flavour, a vector (Ψ_{red}, Ψ_{green}, Ψ_{blue}) of the quark fermionic fields. The f index corresponds to the various quark flavours (u, d, c, s, t, b). In the zero mass limit the QCD Lagrangian is chirally symmetric, i.e. it is invariant under independent rotation of the left-handed and the right-handed quarks in the flavour space. This is a good approximation in the case of very light quarks as *up* and *down* quarks and it can be still partially valid in the case of the *strange* quark. However in nature quarks are not massless and once introducing the mass term, the Lagrangian density is replaced by:

$$\mathcal{L} = -\frac{1}{4}F^a_{\mu\nu}F^{a\mu\nu} + \sum_{f=1}^{6}\overline{\Psi}_f(i\gamma^\mu D_\mu - m_f)\Psi_f \tag{1.5}$$

Now the Lagrangian density is no longer invariant under chiral rotation: the quark mass terms introduce an explicit chiral symmetry breaking. However the hadron mass generation mechanism cannot be explained only considering the small violation due to the explicit symmetry breaking, especially when considering hadrons made of the lightest quarks, where in good approximation the chiral symmetry should be conserved. Indeed, beside the explicit breaking, the chiral symmetry is also spontaneously broken when considering quarks bound states (i.e. hadrons). In this scenario π, K, and η, that are much lighter than other hadrons, can be considered as the Goldstone bosons associated. According to the Goldstone theorem when a generic continuous symmetry is spontaneously broken, to each broken generator corresponds a massless (or light, if the symmetry is not exact) field (Goldstone boson). Therefore in the case of SU(3), the existence of eight pseudoscalar massless particles is expected and they can be identified with the octet of pseudoscalar

mesons. The π, K, and η mesons are actually not massless because of the explicit (small) symmetry breaking due to the presence of the quark mass term in the Lagrangian density. Under the effect of the additional explicit symmetry breaking, the eight Goldstone bosons acquire small masses, compared to the masses of other hadrons. As a consequence of the non-zero vacuum expectation value of the $\overline{\Psi}\Psi$ quark operator ($\langle\overline{\Psi}\Psi\rangle \neq 0$) the chiral symmetry is broken and a dynamically generated quark mass is seen to emerge. It means that the interaction potential is still symmetric but vacuum (i.e. the ground state) is not. From a classical point a view this situation can be depicted by Fig. 1.2.

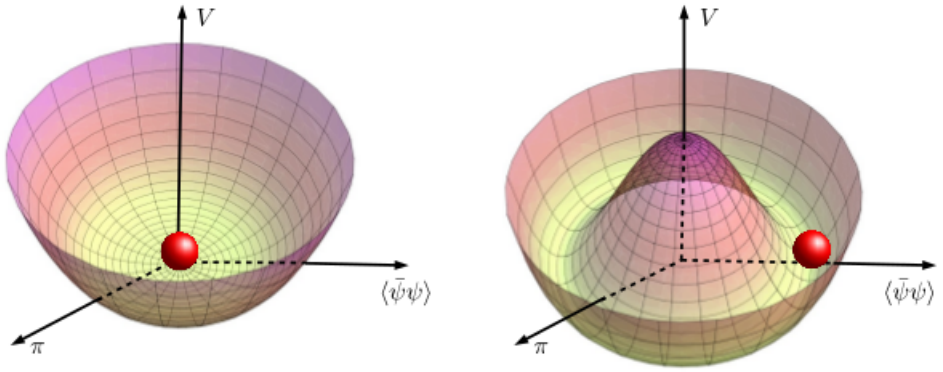

Figure 1.2: Schematic illustration of the spontaneous chiral symmetry breaking mechanism. **Left:** symmetric potential and symmetric ground state. **Right:** symmetric potential but non symmetrical ground state: spontaneous symmetry breaking.

The quark, represented as a sphere, tends to occupy the minimum energy state. Both potentials are symmetric but, unlike the left configuration, where the ground state is symmetric too, for the potential on the right the ground state is located around the centre and there is an infinite set of ground states. The sphere placed in the centre will be forced to choose one of these states breaking the intrinsic symmetry.
Lattice QCD calculations suggest that for critical values of temperature ($T_c \sim 170$ MeV) and energy density ($\epsilon_c \sim 1$ GeV/fm^3) the chiral symmetry can be restored ($\langle\overline{\Psi}\Psi\rangle \to 0$), investigating the nature of the crossover from the confined chiral-symmetry-broken phase to the deconfined,

chiral-symmetry-restored phase (Fig. 1.3). This is one of the main goals of the heavy-ion programs at the Relativistic Heavy Ion Collider (RHIC) at Brookhaven, and the Large Hadron Collider (LHC) at CERN, with several experiments devoted to analyze the QGP formation.

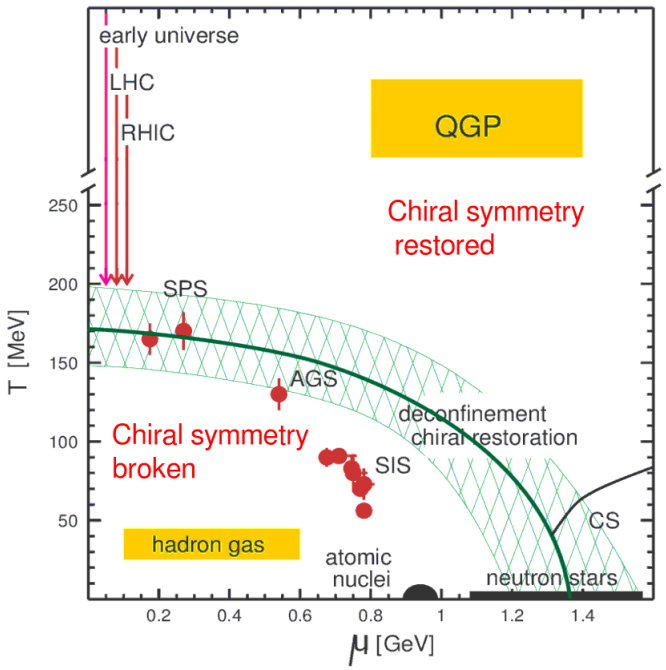

Figure 1.3: QCD phase diagram.

1.2 Relevance of Studying QGP

QGP study is interesting not only as a tool to probe QCD theory, but also in order to investigate first instants of the early Universe. According to the Big Bang theory, space, time, and all matter and radiation in the Universe were formed during the Big Bang some 15 billion years ago. A key challenge is to understand how the Universe evolved from the cosmic fireball created in the Big Bang. About 10^{-5} s after the Big Bang, temperature was high enough (T$>$ 100 GeV) that all the known particles (including quarks, leptons, gluons, photons, Higgs bosons, W and Z) were extremely relativistic. Even the strongly interacting particles, quarks and gluons, would interact fairly

weakly due to asymptotic freedom and therefore perturbation theory should be enough to describe them. Thus the Universe existed in a phase of quarks and gluons (Fig. 1.4) and it started to expand, becoming progressively colder. When temperature dropped to $\sim$ 170 MeV (*critical temperature*) and the energy density decreased until ~ 1 GeV/fm^3 (*critical energy density*), quarks and gluons began to bond together forming colour-less objects: the hadrons. After the hadronization, the primordial nucleosynthesis took place. The Universe was ionized and opaque to the electromagnetic radiation until nuclei and electrons began to combine in the first neutral atoms. Through this process, the whole Universe became transparent and photons were able to diffuse, forming what today is the *Cosmic Microwave Background* (CMB). This happened 380 000 years after the Big Bang, so the direct observation of the early Universe is intrinsically limited by this sort of "cosmic horizon". Therefore the characterization and the analysis of QGP may allow to break this limit and it could be very useful in order to confirm the Big Bang theory and understand the physics of strongly interacting matter under extreme conditions of temperature and energy density.

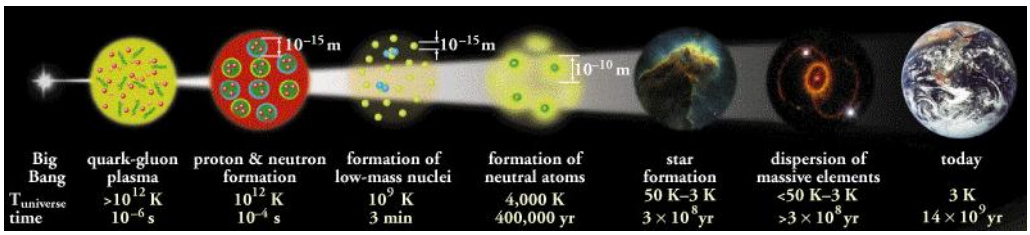

Figure 1.4: Steps of the Universe expansion

1.3 Lattice QCD

The perturbative approach to the QCD does not describe the long-distance behaviour (r $>$ 0.1 fm), which is essential for understanding the QGP–HG (Hadron Gas) transition. A more rigorous approach is needed in order to characterize the physical mechanisms at the origin of colour confinement, and the transition to the deconfined state of hadronic matter. A suitable non-perturbative approach is the numerical study of QCD on a lattice (l-QCD) [2]. In the l-QCD theory quark fields are represented by lattice sites, while gluons are the links between neighboring sites. The physical system

is restricted to a finite-size box. The continuous space-time is represented as a lattice, which introduces an ultraviolet cutoff (i.e. small distances) at the lattice spacing. Passing from the continuum to the lattice finite size, the derivatives are replaced by finite differences. This replacement has to be done in a gauge-invariant way, and hence one often refers to Lattice Gauge Theory (LGT).
This method predicts a phase transition from hadronic matter to a QGP state. Moreover it provides critical values of temperature and energy density of the transition, even though they crucially depend on simulation parameters and the extrapolation from lattice to continuum. Theoretical studies of QGP apply approximate models, perturbation theory, and non-perturbative simulations to understand the properties and to characterize the behaviour of quark-gluon matter at high temperature and density. The main phenomenological properties are:

- **Deconfinement.** At high temperature or energy density, quarks and gluons are no longer confined in colour singlet states. At zero baryonic chemical potential (μ_B), l-QCD calculations show that the transition to QGP occurs at the critical temperature $T_c \simeq 170$ MeV $\simeq 2 \times 10^{12}$ K.

- **Phase transition or crossover.** The transition between confined and deconfined matter at zero baryon density is a smooth crossover and not a true phase transition.

- **Phase diagram 1.** Figure 1.5 shows the QCD phase diagram as a function of temperature and baryonic chemical potential. The figure highlights two main regions separated by a phase boundary where matter is confined (hadron gas) and deconfined (QGP). The dotted lines sketch the nuclear matter evolution in heavy-ion collisions and in the first instants of the early Universe.

- **Phase diagram 2.** Figure 1.6 shows the phase structure as a function of quark mass at zero chemical potential. The QCD phase diagram depends on the interplay of chiral and center symmetry [3]. These symmetries are exact if the quark mass is considered equal to zero or infinite, respectively. Therefore varying the quark masses towards these two limit values, provides useful information on what kind of phase transition can be observed depending on specific values of the quark masses. The lower left corner corresponds to the special case of massless quarks

where the chiral symmetry is restored (**chiral limit**). The upper right corner represents the infinite mass limit where the center symmetry is achieved (**pure gauge limit**). In these cases (the green regions in the plot) a first-order transition occurs. For intermediate quark masses a smooth crossover takes place as a function of temperature. The first-order regions are bounded by red lines denoting a second-order (chiral or deconfinement) transition. The diagonal dashed line corresponds to the case where all the quark masses are degenerated.

Despite the excellent results achieved, which allow a direct comparison with the experimental data, numerical methods always show some limitation due to the inevitable approximations that has to be considered. For example lattice QCD is formulated to describe matter in thermal equilibrium applying only small perturbations. However the system formed by heavy-ions collisions is naturally dynamic. Therefore l-QCD is not designed to describe the evolution of QGP, but it can provide the equilibrium properties of the plasma, which can be used as inputs for the phenomenological models (e.g. hydrodynamic models) of the fireball expansion.

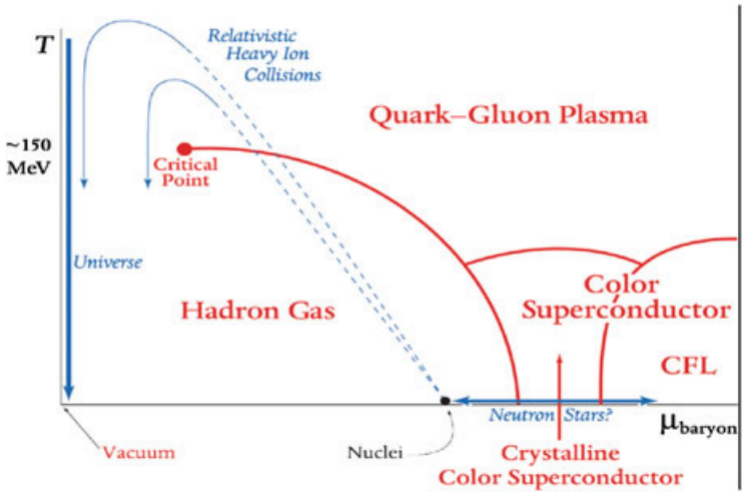

Figure 1.5: Nuclear matter phase transition.

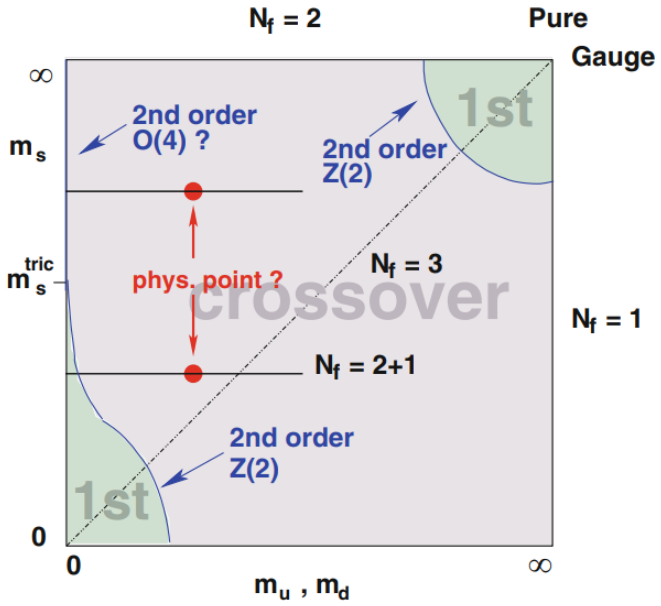

Figure 1.6: The QCD phase diagram in the plane of *strange* and degenerate (*up* and *down*) quark masses.

Chapter 2

QGP Study and Formation

In order to study and create a QGP state at a laboratory level, several conditions have to be satisfied. Since the system formed by strongly interacting particles (quarks and gluons) has to be studied through thermodynamics laws and macroscopic variables, it has to be spatially extended and long lasting. In particular:

- The system dimensions have to be much larger than the scale of strong interactions (~ 1 fm).
- The system has to consist of many particles.
- The system has to achieve thermal equilibrium ($\tau \gg 1$ fm$/c$).

In addition it needs enough energy density for the phase transition, so the estimation of the energy density corresponding to the critical temperature ($T_C = 170$ MeV) is fundamental.
Temperature and energy density are linked by the Stefan-Boltzmann's law:

$$\epsilon = g_* \frac{\pi^2}{30} (k_B T)^4 \tag{2.1}$$

where $g_* = \left(g_b + \frac{7}{8} g_f\right)$ with g_b and g_f indicating the total number of degrees of freedom, summed over the flavours, spins, charges, and colours of bosons and fermions, respectively.
For a gluon, there are 2 helicity states and 8 different colours, therefore $g_b = 16$. For each quark flavour, there are 2 spin states, 2 charge states (quark-antiquark) and 3 colours. By considering 2 quark flavours $g_f = 24$.

Thus the value of the energy density expected for the QGP formation is given by:

$$\epsilon_{QGP} = 37\frac{\pi^2}{30}(k_B T)^4 \tag{2.2}$$

Replacing T with $T_C \simeq 170$ MeV $\simeq 2 \times 10^{12}$ K it is possible to evaluate the numerical value for the critical energy density:

$$\epsilon_C \approx 0.9\,\frac{GeV}{fm^3} \tag{2.3}$$

2.1 High-Energy Heavy-Ion Collisions

The most suitable conditions for QGP study and formation are reached in high energy central heavy-ion collisions, as it happens at CERN LHC.
In the centre of mass reference frame, two colliding nuclei are Lorentz contracted in the longitudinal direction, so they can be considered as two thin disks of radius $R_A \simeq A^{1/3}$ fm. Some important quantities related to the collision are:

- **The impact parameter *b:*** is the distance between the centres of the two interacting nuclei. A smaller impact parameter indicates a more central collision (colliding nuclei almost head-on).

- **The number of participant nucleons:** is the number of protons and neutrons, within the colliding nuclei, which take part in the collision. Those which do not participate are called *spectators*. The number of participants and spectators depends on the impact parameter: collisions with a small impact parameter are characterized by a large number of participant, vice versa in the case of a large impact parameter (Fig. 2.1).

- **The number of interactions:** is the total number of nucleon-nucleon collisions.

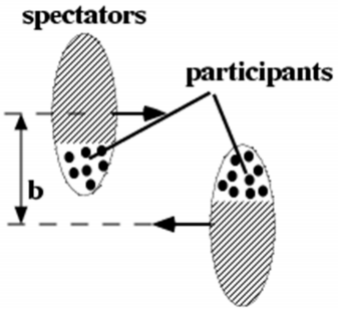

Figure 2.1: Geometry of a high-energy heavy-ions collision

2.2 The Glauber Model

The most used method for computing the quantities introduced above is the *Glauber Model*. It is a probabilistic model, where the starting point is the nucleons density $\rho(z, \vec{s})$ in a nucleus, for given longitudinal (z) and transverse ($\vec{s}$) positions. The model is based on the *optical limit* assumptions:

- Nucleons are considered point-like and independent particles (nucleons size much lower than nucleus size, and nucleons De Broglie wavelength much lower than the distance between two nucleons in a nucleus).
- Nucleus (and therefore nucleons that constitute it) travels along a straight-line path and it is not deflected during the interaction.
- Protons and neutrons are not discernible.
- The cross section of a nucleon-nucleon collision is the same during the whole process.

All these conditions are a good approximation for high-energy collisions (> 100 GeV).
The *nuclear thickness function* is the most relevant quantity in Glauber model calculations and is defined as:

$$T_A(\vec{s}) = \int_{-\infty}^{+\infty} dz \rho(z, \vec{s}) \tag{2.4}$$

with the normalization $\int d\vec{s} T_A(\vec{s}) = 1$. The nuclear thickness function represents the probability of finding a nucleon at a given transverse coordinate, in the nucleus A.

By considering a nucleus-nucleus collision, the probability of having a nucleon-nucleon inelastic interaction, at impact parameter $\vec{b}$ in an area d^2s is given by:

$$T_{AB}(\vec{b})\sigma_{NN}^{inel} = \int d^2\vec{s}T_A(\vec{s})T_B(\vec{b}-\vec{s})\sigma_{NN}^{inel} \tag{2.5}$$

$T_{AB}(\vec{b})$ is known as *nuclear overlap function*. The corresponding probability of n interactions is:

$$P(n,\vec{b}) = \binom{AB}{n}[1-T_{AB}(\vec{b})\sigma_{NN}^{inel}]^{AB-n}[T_{AB}(\vec{b})\sigma_{NN}^{inel}]^n \tag{2.6}$$

which gives the number of A-B nuclei collisions as:

$$N_{coll}^{AB}(\vec{b}) = \sum_{n=0}^{A} nP(n,\vec{b}) = ABT_{AB}(\vec{b})\sigma_{NN}^{inel} \tag{2.7}$$

While the number of participants in nucleus A is:

$$N_{part}^{A}(\vec{b}) = \int d^2\vec{s}BT_B(\vec{s})exp[-AT_A(\vec{b}-\vec{s})\sigma_{NN}^{inel}] \tag{2.8}$$

A similar expression can also be found for the participants in nucleus B, so the total number of participants is simply given by:

$$N_{part}(\vec{b}) = N_{part}^{A}(\vec{b}) + N_{part}^{B}(\vec{b}) \tag{2.9}$$

The geometry of the process described previously is sketched in Fig. 2.2. The number of particles produced in each interaction (multiplicity) can be related to the number of participants or collisions. Multiplicity gives information about energy density, centrality of the collision and the global properties of the created medium and it is one of the main parameters that are used to characterize the collisions.

2.3 The Hydrodynamical Evolution and the Bjorken Scenario

The Bjorken scenario is one of the models developed to characterize the hydrodynamical evolution of the fireball created by heavy-ion collisions. Two

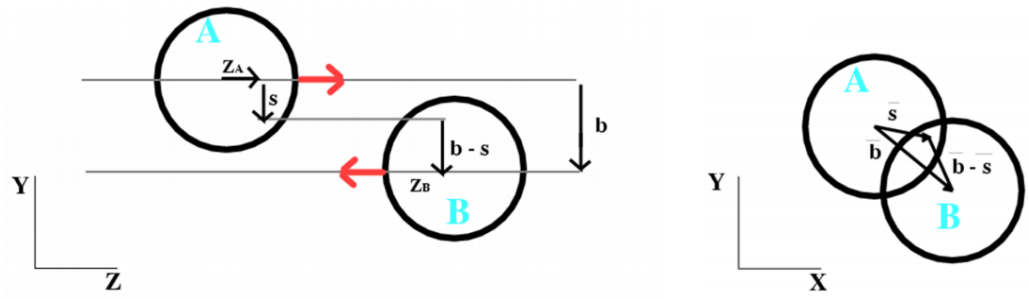

Figure 2.2: Geometry of A and B nuclei collision.

nuclei at high energy can be considered as thin disks due to the Lorentz contraction. The spatial rapidity is:

$$y = \frac{1}{2}\log\frac{t+z}{t-z} \tag{2.10}$$

At asymptotic collision energies, boost invariance is a good approximation in the central rapidity region. Indeed a boost corresponds to an additive term in the rapidity ($y' = y + y_{boost}$). Very large colliding energy corresponds to neglecting longitudinal boosts: the result does not depend on the rapidity. Particle production in the central rapidity region is symmetric under longitudinal boosts and thus produces a plateau in the particle rapidity distribution. In this scenario the secondaries produced by the collision, are simultaneously generated in an initial volume of limited longitudinal extension. This is essentially the Bjorken condition: $\tau_f \ll 2R/\gamma$ where τ_f is the formation time[1] of secondaries, R is the nuclear radius and γ is the Lorentz factor. In addition the nuclei crossing time has to be smaller than the characteristic time of the strong interaction (~ 1 fm/c). This condition implies that the secondaries are produced after the nuclei have crossed. Eventually, taking into the account previous hypothesis, the expression of the average energy density of produced particles can be found as:

$$\epsilon_{Bj} = \frac{1}{\tau_f A}\frac{dE_T(\tau_f)}{dy} \tag{2.11}$$

This is known as *Bjorken energy density* (A is a spatial parameter, it is the transverse section of the interested region and $E_T = m_T cosh y \simeq m_T$

[1] τ_f is evaluated as $\tau_f = \frac{\hbar}{m_T}$ according to the indeterminacy principle.

because $y \simeq 0$).
As long as the fireball expansion is predominantly longitudinal, the Bjorken formula can be used in order to evaluate the time evolution of ϵ_{Bj} as shown in figure 2.3.

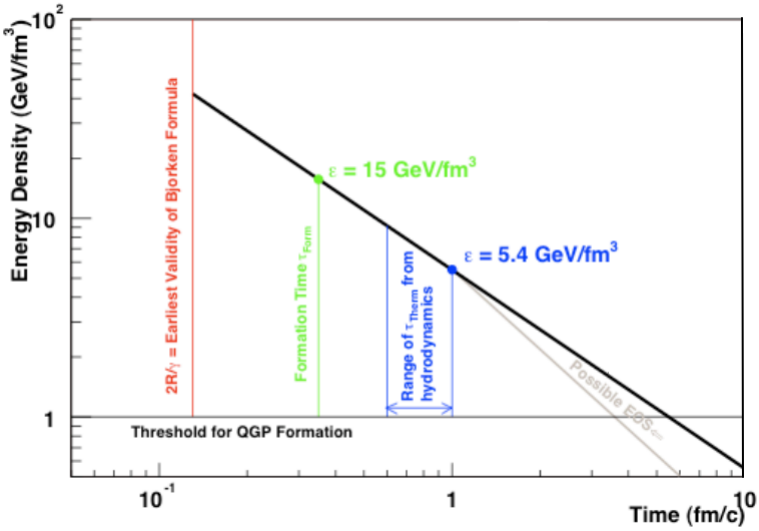

Figure 2.3: Time evolution of the energy density [4].

2.4 Fireball Evolution

The evolution of the system formed in a heavy-ion collision is commonly sketched as following:

1. **Pre-equilibrium:** in this phase secondaries, quarks and gluons are created and the thermalization occurs.

2. **QGP:** if the system reaches the critical value of temperature and energy density, quarks and gluons become free: QGP formation. Then, because of pressure gradients, the fireball expands following thermodynamic and hydrodynamic laws

3. **Mixed phase/Crossover:** the system cools down during its expansion. When the temperature drops below the critical value, the hadronization starts, therefore quarks and gluons turn confined into hadrons.

4. **Hadron Gas:** the system is now formed by an interacting hadron gas.

5. **Chemical freeze-out:** the energy of hadronic interactions is too low to allow inelastic processes, so they can only interact elastically: the chemical abundance is fixed.

6. **Kinetic freeze-out:** it occurs when the elastic interactions cease too. Eventually particles produced can be detected.

Fig. 2.4 shows a schematic view of the fireball space-time evolution.

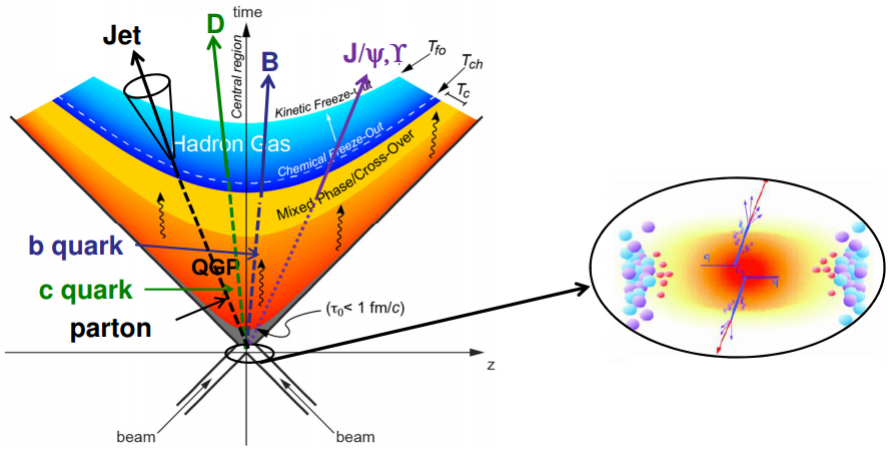

Figure 2.4: Space-time evolution of the fireball formed by heavy-ion collisions

2.5 Observables for Possible QGP Signatures

There are several probes used to investigate the phases of heavy-ion collisions: the initial stages, the QGP phase, and the final hadronic phase. Each of these measured observables are particularly sensitive to the conditions of the different stages. QGP signatures are usually divided into *hard probes* and *soft probes*. Hard probes are particles produced with high transferred momentum ($\gg 1$ Gev/c). They are created in the first instants of the collision so they may cross the deconfined medium. On the contrary soft probes have low transferred momentum. They are produced during the latest moments of the collisions, when the fireball is ending its expansion. In addition, photon

detection can also provide information on QGP formation. They are irradiated by the plasma and called *early probes*. However, since other photons are produced when the system evolves, it is difficult to recognize the early probes from the photons background.

2.5.1 Hard Probes

Hard probes are processes characterized by high transverse momentum and therefore they can be calculated with perturbative QCD (high $q^2 \Rightarrow$ small α_s). There are three kind of hard probes:

- **Jet quenching:** jet shower produced by partons fragmentation in the initial collision propagates through the QGP while it expands and cools. During this process the jet shower itself evolves and its modification depends on the properties of the medium. The energy loss of a high-energy jet in a hot QCD plasma appears to be much larger than in cold nuclear matter. Such a modification is called *jet quenching*.

- **Heavy flavour states:** due to their large masses, heavy quarks (like *charm* or *bottom*) are produced in hard-scattering processes at the early stages of the collisions. Therefore they undergo the full system evolution, interacting with the QGP constituents through both elastic and inelastic processes. This causes a significant energy loss and consequently the yields of particles containing heavy quarks are expected to be suppressed if a deconfined medium formed.

- **Quarkonium suppression:** Heavy quarks (c, b) produced by nucleon-nucleon interactions could form quarkonium states, particles composed of a heavy quark and anti-quark of the same type (like charmonium: $c\bar{c}$, and bottomonium: $b\bar{b}$). However, in presence of a deconfined medium, heavy quarkonium production is suppressed because of colour screening. The quarks of the previous quarkonium state appear later, after hadronization, as open charm or open beauty hadrons. This kind of suppression affects also other hadrons, but $c\bar{c}$ and $b\bar{b}$ states are particularly interesting since they are not easily recreated by recombination in the medium, because of their huge masses. Therefore the dissociation of heavy quarkonium ground states represents a clear evidence of deconfinement.

2.5.2 Soft Probes

Soft probes represent the major part of the observables and they are produced in the final stages of the collision. They keep indirect information of many fundamental QGP properties, such as chemical composition, system size, thermodynamic parameters, expansion velocity etc. Soft probes are:

- **Event characterization:** The energy density and the temperature of the initial phase of the collision are key physical quantities, since they are indicative of the possible QCD phase transition that occurred in the collision. Both can be in principle determined by mean of the centrality and the multiplicity of produced particles. Indeed from the measurements of the charged-particle pseudorapidity density, the Bjorken formula (eq. 2.11) can be also written as:

$$\epsilon_{Bj} = \frac{1}{\tau_f A}\frac{dE_T(\tau_f)}{dy} = \frac{1}{\tau_f A}\langle m_T\rangle\frac{dN_{ch}(\tau_f)}{dy} \tag{2.12}$$

  The charged-particle multiplicity per unit of (pseudo)rapidity ($\mathrm{d}N_{\mathrm{ch}}/\mathrm{d}\eta$) is studied as a function of centrality for different collision systems and energies in order to get insight on the role of the initial energy density and the mechanisms at the basis of particle production. To compare the particle production in different collision systems, the $\mathrm{d}N_{\mathrm{ch}}/\mathrm{d}\eta$ measured at mid-rapidity ($|\eta| < 0.5$) is scaled by the number of the collision participants pair, $\langle N_{part}\rangle/2$. Fig. 2.5 shows the trend of the charged particle density at mid-rapidity per participants pair for different collision systems as a function of the centre of mass energy $\sqrt{s_{\mathrm{NN}}}$. In the case of A–A collisions the curve increases faster than the one related to smaller systems. This means that in A–A collisions the mechanism of the initial energy conversion into particle production is more efficient than pp or p–A collisions and that A–A collision cannot be treated as a pure overlapping of pp collisions.

- **Particle yields and spectra:** Particle abundances and their momentum spectra provide information on the chemical composition of the system (fixed during the chemical freeze-out) and on its dynamical evolution. Indeed the presence of a collective flow is reflected in the soft part of the spectra (up to around 2.5 GeV/c), producing a hardening of the p_{T} spectra with increasing multiplicity and a shift in the

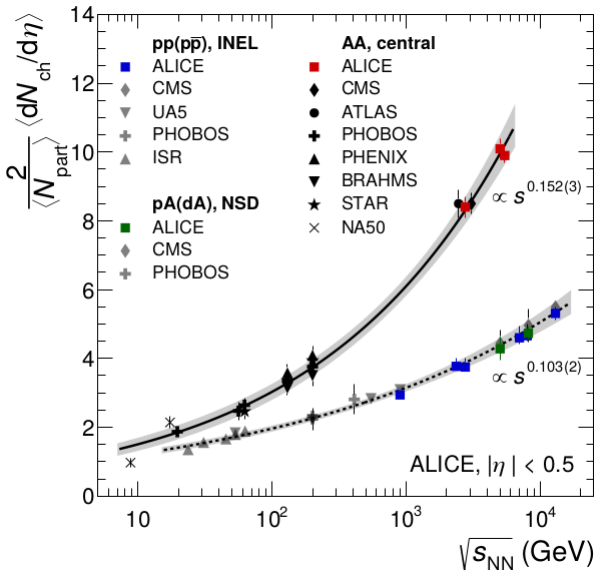

Figure 2.5: Particle density distribution at mid-rapidity per participant pair for various collision systems as a function of the centre of mass energy [5].

maximum of the distributions to larger p_{T} that depends on the hadron mass (Fig. 2.6). In this p_{T} region the random thermal motion and the collective motion of expanding system affect the p_{T} distribution. In particular the second effect is more pronounced for heavier particles because all hadrons acquire an additional term given by their mass multiplied by the common flow velocity.

- **Strangeness enhancement:** The enhanced production of hadrons containing multiple strange quarks is considered as a clear signature of QGP formation [6]. Indeed the initial strangeness content of the colliding nuclei is very small and there is no initial net strangeness. In the QGP the gluon density is high enough to promote the *strange* quark production from gluon fusion processes, leading to an abundance of *strange* quarks during the deconfined phase. This can be experimentally observed as an increase of the strange particles yields (like Ξ and Ω) thanks to the recombinantion mechanism. Strangeness enhancement is usually measured by considering the ratio of strange hadrons to pions. Recent results show a smooth evolution passing from high multiplicity pp collisions (where the increasing trend starts) up to a plateau in

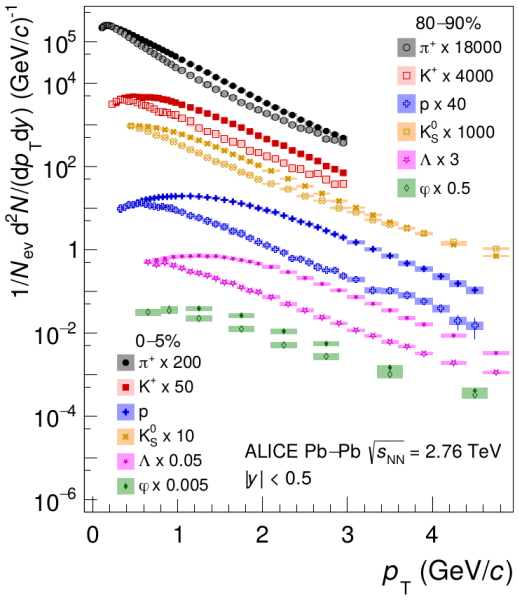

Figure 2.6: The p_{T} distributions of π^+, K^+, p [8], $\mathrm{K}^0_{\mathrm{S}}$, Λ [9], and ϕ [10] for the 0–5% and 80–90% centrality intervals in Pb–Pb collisions at $\sqrt{s_{\mathrm{NN}}} = 2.76$ TeV.

central heavy ion collision [7] (Fig. 2.7).

- **Collective flow:** A consequence of the QGP formation is the presence of collective flows: gradients of pressure produce acceleration of fluid elements that causes a collective expansion of the fireball. The collective flows modify the transverse momentum distribution of the particles produced. Anisotropic flow is the result of a directional dependence to these pressure gradients. In particular it is due to a correlation between the azimuthal angle and the reaction plane[2] (Fig. 2.8). The most interesting case concerns the non-central collisions (b $\neq$ 0), where the fireball created is almond-shaped. The early spatial anisotropy produces an anisotropy in the particles transverse momentum which is strongly dependent on the azimuthal angle and that can be detected.

[2]The reaction plane is the plane defined by the impact parameter and the beam direction.

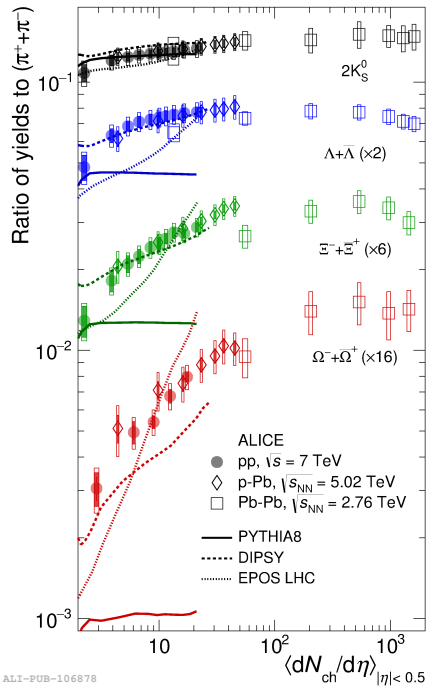

Figure 2.7: The p_{T}-integrated yield ratios of strange and multi-strange hadrons to pions as a function of charged-particle multiplicity density [7].

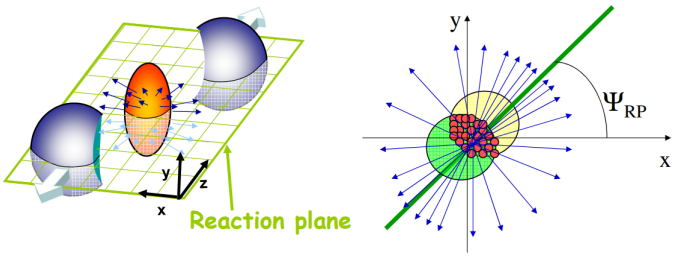

Figure 2.8: Anisotropic flow geometry scheme.

Chapter 3

Hadronic Resonance Production

After QGP formation, the created fireball expands, the system cools down and the energy density decreases. When its value drops below the critical one ($\epsilon_c \simeq 1$ GeV/fm^3, according to l-QCD calculations) the hadronization of the plasma starts and quarks and gluons return to be confined into hadrons. The result of this transition is the formation of an interacting hadron gas that has still collective behaviour. The hadronization process involves quark and gluon interactions with small momentum transfers and therefore large values of α_s. This implies that a perturbative approach is not possible in this phase and it is needed to refer to phenomenological models. The detailed description of some event generators and models, like PYTHIA and EPOS, can be found in sections 3.1.1 and 3.1.2.
After the hadronization the created hadrons can still interact inelastically until the temperature of chemical freeze-out is reached. Starting from this moment the abundances of the different hadron species are fixed (except for resonance decays). There are still significant elastic interactions between hadrons, affecting the momentum distributions of the different populations that persist until the kinetic freeze-out occurs, when also the elastic collisions cease. Then particles can be detected.
The phase between the chemical and the kinetic freeze-out is known as *hadronic phase* and its timescale at the LHC energies is $\sim$ 1-10 fm/c. Hadronic resonances with comparable lifetime are perfect probes to characterize the evolution of the late hadronic phase, indeed they may be sensitive to the competitive mechanisms of rescattering and regeneration. Resonances are reconstructed starting from the invariant mass distribution of their decay daughters, therefore if a resonance decays inside the hadronic medium, the

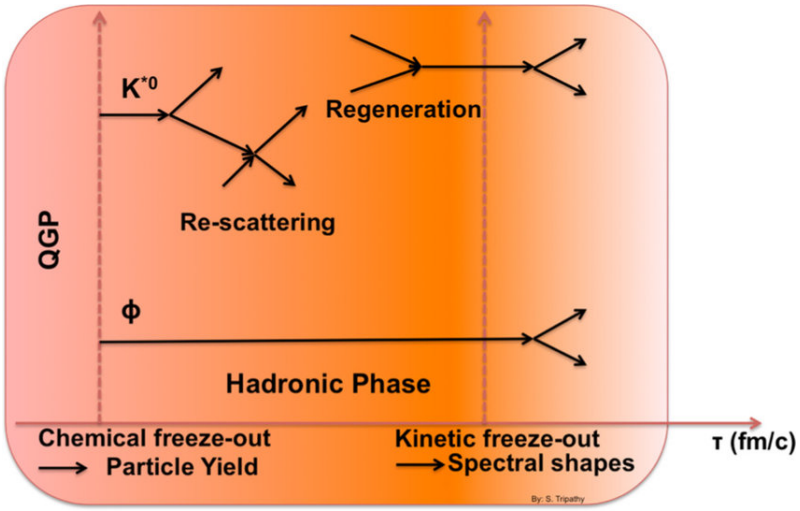

Figure 3.1: Schematic illustration of rescattering and regeneration processes during the hadronic phase [11].

decay products may interact with the other particles of the hadron gas. This causes a loss of contributions for the resonance reconstruction, leading to a suppression of the resonance measured yield with respect to the abundance produced at the chemical freeze-out. The process just described is known as re-scattering. Rescattering can be balanced by the regeneration mechanism. It occurs when the particles of the hadronic medium, as a consequence of pseudo-elastic collisions, regenerate a given resonance, resulting in an enhancement of the measured yield. Longer-lived resonances, decaying mainly at the end or after the hadronic phase, should not be affected by any of these processes. Fig. 3.1 offers a schematic view of such mechanisms, comparing the different expected behaviour for a short-lived resonance (K^{*0}) and a longer-lived one (ϕ), while the main resonances studied by ALICE in order to characterize the properties of the hadronic phase are listed in Tab. 3.1.

The quantity of suppressed or enhanced yields depends on the resonance lifetime, the cross sections for rescattering and regeneration processes, and the duration of the hadronic phase. In particular for central A–A collision the hadronic phase is expected to last longer than peripheral collisions, since a larger system volume is created. The best way to quantify the net effect is comparing resonance yields to ground-state hadrons with similar quark content. Indeed the yields of stable and long-lived hadrons reflect the con-

Table 3.1: List of hadronic resonances and their properties: lifetime (τ), quark composition, hadronic decay channel, and the corresponding branching ratio.

Resonance	$\rho(770)^0$	$\mathrm{K}^*(892)^\pm$	$\mathrm{K}^*(892)^0$	$\Sigma(1385)^\pm$	$\Lambda(1520)$	$\Xi(1530)^0$	$\phi(1020)$
τ(fm/c)	1.3	3.6	4.2	5-5.5	12.6	21.7	46.4
Quark content	$\frac{u\bar{u}+d\bar{d}}{\sqrt{2}}$	$u\bar{s}, \bar{u}s$	$d\bar{s}, \bar{d}s$	uus, dds	uds	uss	$s\bar{s}$
Decay	$\pi\pi$	$K^0_S\pi^\pm$	$\mathrm{K}\pi$	$\Lambda\pi^\pm$	pK	$\Xi\pi$	KK
B.R. (%)	100	33.3	66.6	87	22.5	66.7	48.9

ditions at the freeze-out, while the yield of short-lived resonances can be modified by the last interactions inside the hadronic medium. The rich variety of resonances (different mass, lifetime, decay daughters, etc.) allows to scan in a privileged way the interaction zone, following the evolution of the hadronic phase. Then the ratio of resonance integrated yields over the long-lived particle ones can provide valuable information about the properties of the hadronic phase, especially if performed with resonances of increasing proper lifetime and across different collision systems. Such a study done using ALICE and STAR data is shown in Fig. 3.2 where the ratios of p_{T}-integrated yields ρ^0/π [12], $\mathrm{K}^{*0}/\mathrm{K}$ [13–15], $\Sigma^{*\pm}/\Lambda$ [16–19], Λ^*/Λ [19–21], Ξ^{*0}/Ξ [16,17], and ϕ/K [13–15] are presented as function of the cubic root of the charged-particle multiplicity density. For central Pb–Pb collisions the yields of ρ^0, K^{*0}, $\Sigma^{*\pm}$, and Λ^* are suppressed with respect to peripheral Pb–Pb, pp and p–Pb collisions. This would indicate the dominance of re-scattering mechanism compared to the regeneration one. No centrality dependence is observed across the different systems for the Ξ^{*0}/Ξ and ϕ/K ratios. Since Ξ^* and ϕ live longer, it is expected they decay predominantly after the end of the hadron gas phase and therefore their yield should not be affected by regeneration or re-scattering effects.

3.1 QCD-inspired Event Generators

Event generators are fundamental in QCD modelling, especially for the soft hadronic phenomena, where theoretical computations cannot be performed from first principles (non perturbative theory), and they are widely used in order to make predictions for collider experiments. The generated events are then subjected to additional simulations of detector response, usually performed using Monte Carlo methods, being reconstructed as real data. Finally

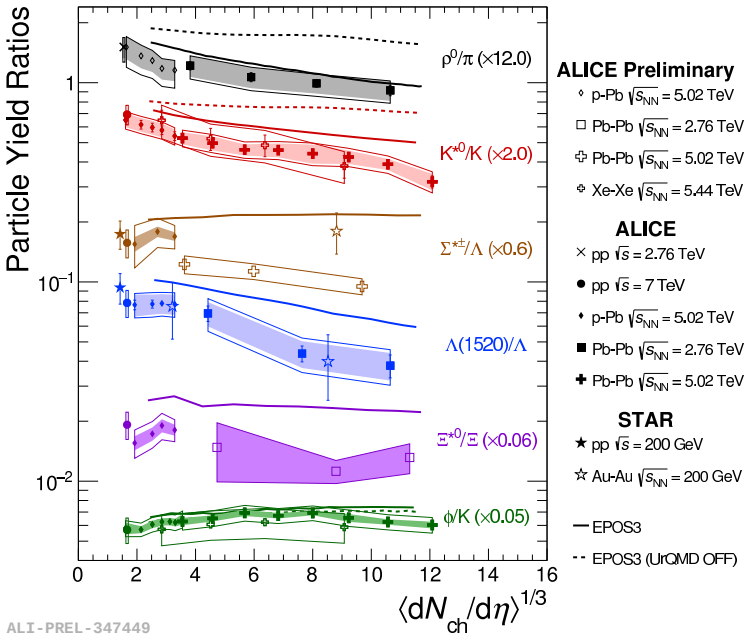

Figure 3.2: Ratios of p_{T}-integrated resonance yields to long-lived particle yields in increasing lifetime order: ρ^0/π [12], $\mathrm{K}^{*0}/\mathrm{K}$ [13–15], $\Sigma^{*\pm}/\Lambda$ [16–19], Λ^*/Λ [19–21], Ξ^{*0}/Ξ [16, 17], and ϕ/K [13–15] as a function of $\langle \mathrm{d}N_{\mathrm{ch}}/\mathrm{d}\eta \rangle^{1/3}$ for different collision systems. Data are compared to EPOS3 predictions with and without UrQMD [22].

simulated reconstructed events can be compared to experimental measurements. A large set of event generators is used in high energy physics both for small (pp, p–Pb) and heavy-ion collisions. Predictions of the particle yields and momentum distributions are very useful tools in data analysis and they are offered by several models. The event generators that provided the most intriguing point to ponder for the results shown in this thesis, i.e. PYTHIA and EPOS-LHC, are described in the following sections.

3.1.1 PYTHIA

PYTHIA [23] is a General Purpose Monte Carlo (GPMC) event generator used for the description of several types of high energy collisions (electrons, protons, photons and heavy nuclei). It investigates a large variety of physics aspects including hard and soft interactions, parton distributions, initial and

final state parton showers, multiple partonic interactions (MPIs), fragmentation and decay.

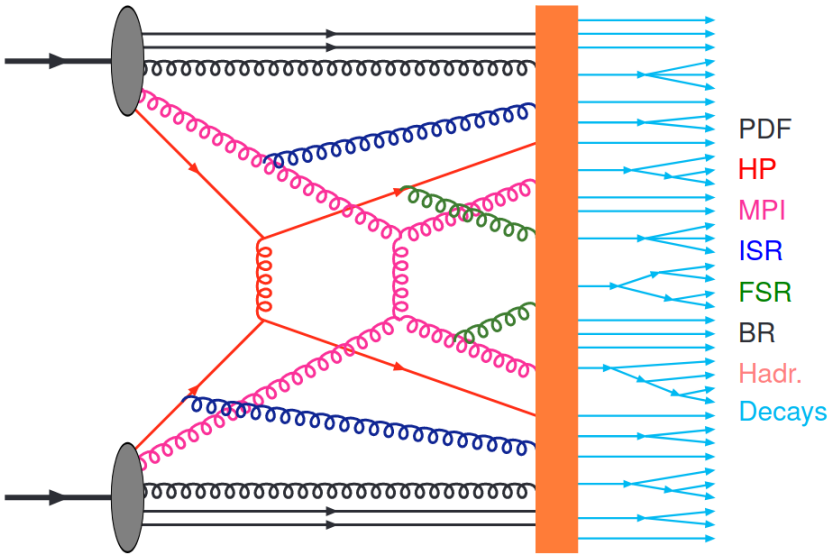

Figure 3.3: Sketch of a hadron-hadron collision as simulated by PYTHIA. Legend: PDF = Particle Distribution Function; HP = Hard Process; MPI = Multiple Partonic Interaction; ISR = Initial State Radiation; FSR = Final State Radiation; BR = Beam Remnant; Hadr. = Hadronization; Decays = decay products [24].

Referring to Fig. 3.3 the simulation begins with the hard collision of the incoming beams where the parton densities are described by the Parton Distribution Functions (PDFs). This is followed by the parton shower phase, due to colour radiation of incoming (Initial State Radiation) and outcoming (Final State Radiation) partons (gluons themselves are also coloured, therefore an emitted gluon can trigger a new radiation leading to a very extended shower). At the end of the parton shower phase the hadronization begins. The model used by PYTHIA for converting the partonic medium into hadrons is based on the Lund string model [25]. The QCD field is described in terms of phenomenological strings which break to produce hadrons. The last step of the simulation chain involves the decay of unstable hadrons, whose products are the particles that will be detected. In parallel to this main sequence multipartonic interactions may also occur as a consequence of the

composite nature of hadrons. Indeed if hadrons are considered as a cluster of the incoming partons, the probability of several separate parton scatterings in the same event is not trivial. This additional component gives a significant contribution to the beam remnant and the underlying event structure that cannot be neglected.
PYTHIA model has been updated over the years implementing different new tunings. In particular the results shown in this thesis are compared to PYTHIA6 (Perugia 2011 tune) [26] and PYTHIA8 (Monash 2013 tune, both with and without colour reconnection) [27, 28] predictions. Colour reconnection (CR) is a mechanism known to reproduce the collectivity-like signals in small systems [29]. Models including the "colour ropes" effect base their calculation on the probability to connect partons by colour flux tubes in such a way that the length of the string is as short as possible. Therefore the fragmentation of two independent hard scatterings becomes dependent due to the colour link and induces the rise of the mean p_{T} as a function of multiplicity. In particular in PYTHIA the string connecting two partons follows the evolution of the partonic endpoints resulting in a common boost of the string fragments (i.e. the hadrons). The effect of this boost is similar to the one observed for the collective flow that affects the hadrons spectra in heavy-ion collisions but the origin in this case is different. In addition since the colour reconnection produces shorter and less energetic strings, the formation by their fragmentation of more massive hadrons for a given quark content becomes disadvantaged. This could be the explanation for the resonance suppression (such as K^*/K and ρ^0/π) measured in high multiplicity small collisions systems.

3.1.2 EPOS-LHC

EPOS [30] is a MC event generator based on the parton-based Gribov-Regge theory [31]. It applies a common approach for pp, p–A and A–A collisions using the same formalism. Fig 3.4 shows the typical description of pp and A–A collisions used in high energy physics models. The labels "projectile" and "target" refer only to the two opposite directions along the beam axis.

EPOS-LHC [32] is a tune of the EPOS model that introduces a different type of flow in the case of the quick expansion of a very dense system compressed in a small volume with respect to the large volume created in heavy-ion collisions, as could happen in high multiplicity pp collisions, where the critical energy density may be reached as a consequence of MPI. In EPOS

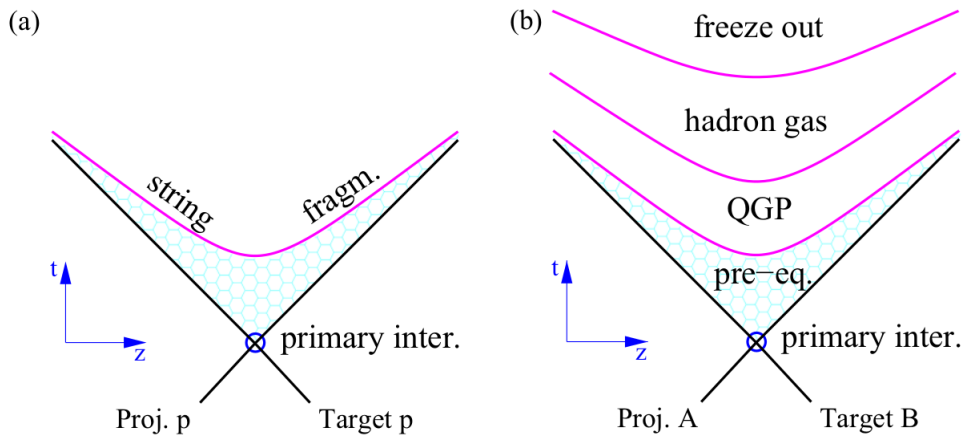

Figure 3.4: Space-time evolution of the system formed in pp **(a)** following the standard approach and heavy-ion **(b)** collisions with a more complex treatment. The hyperbolas represent particles with the same proper time.

the initial conditions for hadronization are based on strings fragmentation. Before hadrons are formed, the string segments are grouped into two different regions: low density area ($\ll \epsilon_c$) known as corona and high density one referred as core. In each event a part of the string fragments hadronizes normally (corona), while a part undergoes to a collective hadronization (core) as shown in Fig. 3.5.

Core can form only if the value of the local density of the string segments increases to the critical one. This threshold is easily reached in central heavy-ion collisions, but density could be high enough also in the case of pp collisions because of multiple scattering between partons in a single pair of nucleons, where many strings which will overlap are created. Fig. 3.6 offers a schematic view of core and corona interplay for different collision systems, as modelled in EPOS.

The main innovation introduced with the EPOS-LHC version is that both parametrizations of flow depend only on the total mass of the high density core formed by the overlap of the string fragments as a consequence of multiple parton interactions in the case of pp collisions or for multiple nucleon interactions for A–A system. The difference is in the volume and in the speed of the core expansion, that permits to use two different flow parametrizations for the two different systems.

In EPOS has been also introduced the possibility to integrate a hadronic

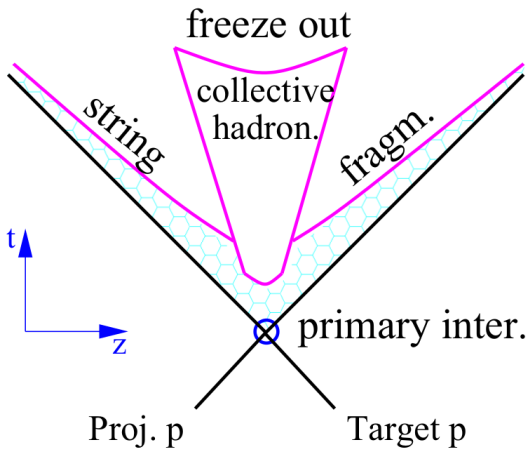

Figure 3.5: Schematic representation of the space-time evolution of the particle production in a hadronic interaction with EPOS LHC. The same treatment is used for pp or A–A but the collective hadronization is simplified in the case of pp collisions with respect to the full evolution of heavy-ion collisions.

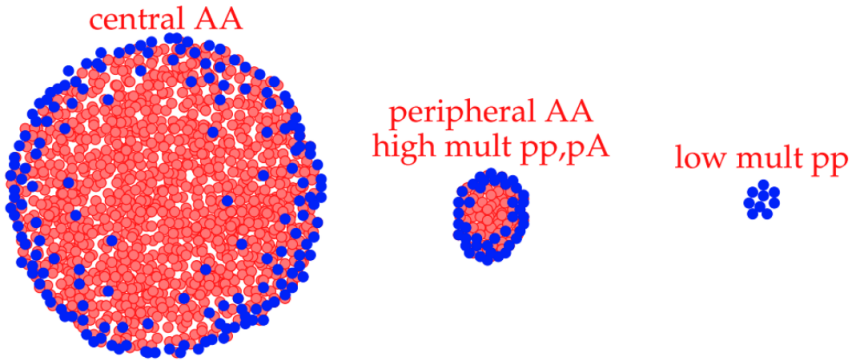

Figure 3.6: Core and corona picture for different collision systems.

cascade stage modelled with the UrQMD (Ultra-Relativistic Quantum Molecular Dynamics) [33] hadronic afterburner for the description of the hadronic phase. After the hadronization, hadrons from core and corona are fed into UrQMD, which describes hadronic interactions with a microscopic approach [34, 35].

3.2 Signals for Deconfinment in Small Systems

In heavy-ion analyses observables are studied as a function of the centrality of the collision, defined by mean of the charged particle event multiplicity. Besides heavy-ion collisions, in the ALICE experiment data from small collision systems, like pp and p–Pb collisions, have been collected too and used as a baseline for A–A collisions. Indeed in such systems the suitable conditions to form QGP should not be reached. However recent studies of pp and p–Pb collisions at LHC energies with high charged-particle multiplicities, where the number of produced particles is of the same order as that in peripheral A–A collisions, showed some patterns that are reminiscent of phenomena observed in heavy-ion collisions. For example double-ridge structure [36], strangeness enhancement [37], hardening of hadron p_{T} spectra [38–41], and suppression of short-lived resonance yields with increasing multiplicity [41] have been recorded even in small collision systems.
Fig. 3.7 shows the $\mathrm{K}^{*}(892)^{0}$ differential p_{T} distributions measured in Pb–Pb at 5.02 TeV (Fig. 3.7.a), p–Pb at 8.16 TeV (Fig. 3.7.b), and pp collisions at 13 TeV (Fig. 3.7.c) nucleon-nucleon centre of mass energies, for different multiplicity classes. The lower panels of the p–Pb and pp plots show respectively the ratios of the p_{T} spectra to the non-single diffractive (NSD) and to the inclusive (INEL>0) ones. The hardening of p_{T} spectra with increasing multiplicity, that as explained in section 2.5.2 in heavy-ion collisions is usually considered as a signature of collective flow, can be observed not only in the plot obtained for Pb–Pb collisions, but also in p–Pb as well as in pp ones. In addition for $p_{\mathrm{T}} < 5$ GeV/c the slopes clearly increase from low to high multiplicity both for p–Pb and pp collisions. For $p_{\mathrm{T}} > 5$ GeV/c the spectral shape are quite the same for all multiplicity classes, therefore the process causing the spectra variation is dominant at low p_{T}.

Fig. 3.8 show the p_{T}-integrated yields ratios of K^{*0} and ρ^{0}, both having very short lifetimes (see Tab. 3.1) and of the longer-lived ϕ resonance to their non-resonant hadronic states as a function of the cubic root of the

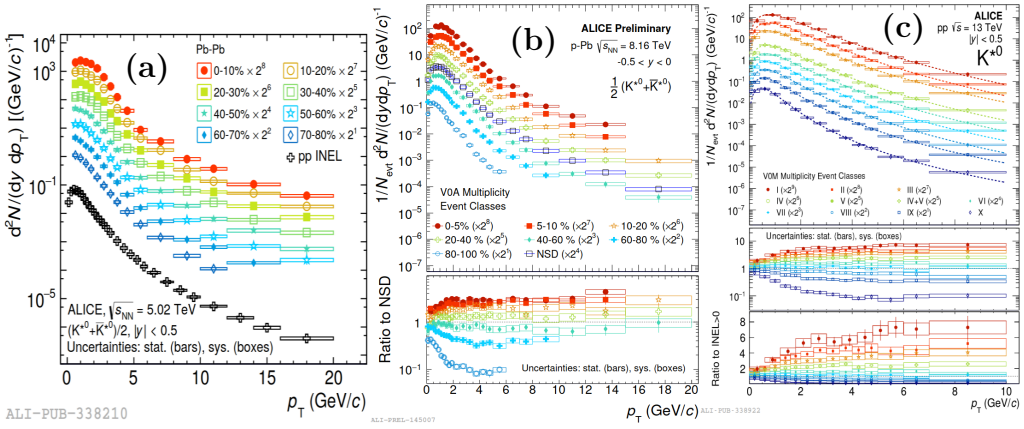

Figure 3.7: Differential p_{T} spectra of $\mathrm{K}^*(892)^0$ in Pb–Pb at $\sqrt{s_{\mathrm{NN}}} = 5.02$ TeV **(a)** [13], in p–Pb at $\sqrt{s_{\mathrm{NN}}} = 8.16$ TeV **(b)**, and in pp collisions at $\sqrt{s} = 13$ TeV **(c)** [41], for different multiplicity classes, scaled by the indicated factors. Lower panels in **(b)** and **(c)** show respectively the ratios of the p_{T} distributions to the non-single diffractive (NSD) and to the inclusive (INEL>0) spectra.

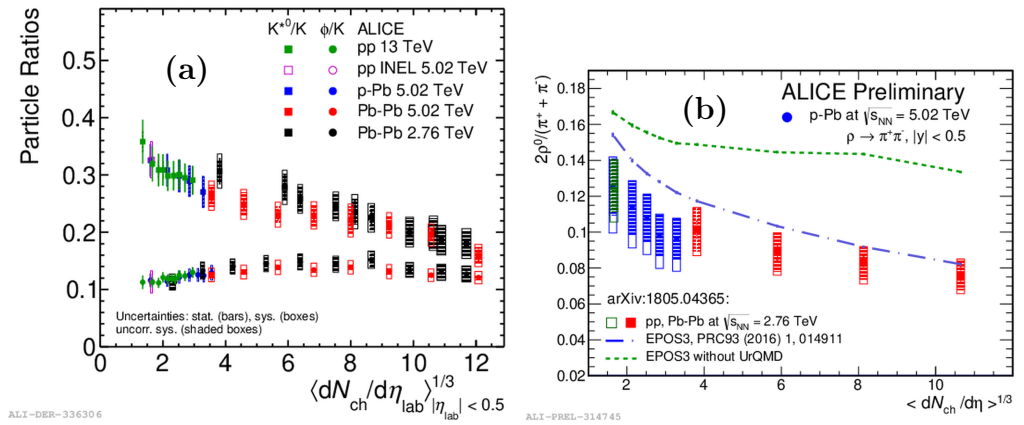

Figure 3.8: Ratios of $\mathrm{K}^{*0}/\mathrm{K}$, ϕ/K **(a)** [13, 14, 41, 42], and ρ^0/π **(b)** [12] p_{T}-integrated yields as a function of $\langle \mathrm{d}N_{\mathrm{ch}}/\mathrm{d}\eta \rangle^{1/3}$ for different collision systems. ρ^0 data are also compared to EPOS3 predictions with and without UrQMD [22].

charged-particle multiplicity density ($\langle \mathrm{d}N_{\mathrm{ch}}/\mathrm{d}\eta \rangle^{1/3}$). In particular Fig. 3.8.a shows the $\mathrm{K}^{*0}/\mathrm{K}$ and ϕ/K ratios [13, 14, 41, 42] while Fig. 3.8.b shows the

ρ^0/π ratios [12] for the indicated collision systems and energies. For central Pb–Pb collisions the K^{*0}/K and ρ^0/π ratios are suppressed with respect to peripheral Pb–Pb, pp and p–Pb collisions, as expected with the assumption of rescattering effect during the hadronic phase (see chapter 3). However a hint of suppression can be noticed also for high multiplicity pp and p–Pb collisions, even though not really significant due to large uncertainties. This could suggest the presence of a hadron-gas phase with a non zero lifetime even in these smaller systems. Instead no centrality dependence is observed for the ϕ/K ratio, due to ϕ longer lifetime. Fig. 3.9.a shows the p_T dependence of K^{*0}/K for low and high multiplicity classes (X and II, respectively) in pp collisions at $\sqrt{s} = 13$ TeV [41]. The ratios increase at low p_T and saturate for $p_T \gtrsim 2.5$ GeV/c, however for $p_T \lesssim 2.5$ GeV/c the ratio in the high multiplicity class (II: red spectrum) is smaller than the one computed in the lowest class (X: blue plot). This trend is qualitatively consistent with that observed in Pb–Pb collisions at $\sqrt{s_{NN}} = 2.76$ TeV [42], where the K^{*0}/K ratio in central Pb–Pb collisions is compared to the pp reference (Fig. 3.9.b). Since a stronger suppression at low p_T is considered in heavy-ion collisions as a signature of rescattering effects, this evidence could be a hint of a possible hadronic phase in pp collisions too.

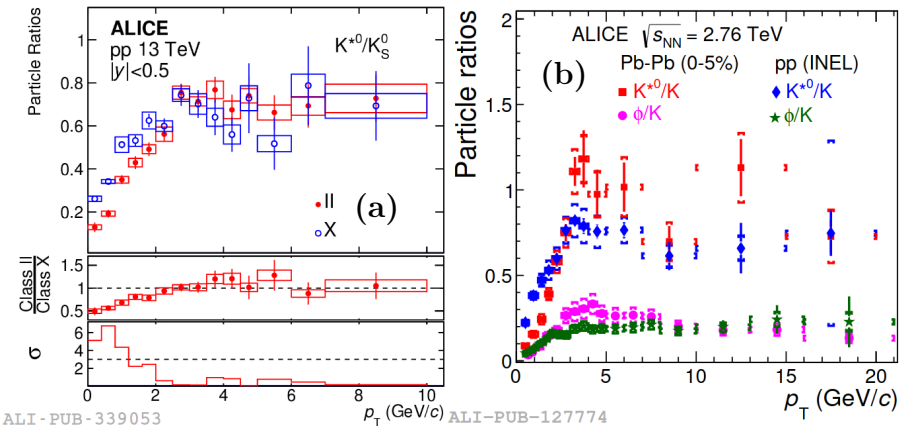

Figure 3.9: **Left panel (a):** The p_T-differential K^{*0}/K ratios for low (X) and high (II) multiplicity classes in pp collisions at $\sqrt{s} = 13$ TeV [41]. Middle panel shows the high multiplicity spectrum divided by the low multiplicity one, with the significance of the deviations from unity reported in the lower panel. **Right panel (b):** ratios of particle yields K^{*0}/K together with ϕ/K results in pp and 0-5% central Pb–Pb collisions at $\sqrt{s_{NN}} = 2.76$ TeV [42].

Part II

A Large Ion Collider Experiment

Chapter 4

ALICE Overview

ALICE (A Large Ion Collider Experiment) [45] is one of the large experiments installed at the Large Hadron Collider (LHC) at CERN. This project involves an international collaboration of more than 2000 members, from 173 institutes in 40 different countries. ALICE is mainly designed in order to study the physics of strongly interacting matter created in heavy-ion collisions (A–A) at ultra-relativistic energies. However, pp and p–A collisions are also studied as a comparison with A–A collisions. The ALICE detector is 26 m long, with a transversal section equal to 16×16 m^2. The detector sites in a vast cavern 56 m underground, receiving beams from the LHC. To deal with the increased luminosity planned by LHC [43] for Run 3 and Run 4 (a factor 10 increase of the Pb–Pb integrated luminosity is expected), ALICE during the Long Shutdown 2 (LS2) has undergone a major upgrade and replacement of sub-detectors as well as of trigger and data-acquisition systems. Fig. 4.1 shows the LHC schedule, starting from the LS2 (2018-2021).

During this upgrade [44], a smaller beam pipe has been installed in place of the existing one, passing from a radius of 29.8 mm to one of 19.2 mm. The need for a new beam pipe is linked to the replacement of the Inner Tracking System (ITS), which surrounds it. The new ITS is completely based on monolithic active pixel sensors fast-acting and fine-grained to handle the higher collision rates expected. The Time Projection Chamber (TPC) was equipped with GEM-based readout chambers, and the muon system was upgraded and extended by the Muon Forward Tracker (MFT). In addition, a new fast interaction trigger detector (FIT) will detect particles that scatter with a small angle relative to the beam direction. As a consequence of the increased luminosity and interaction rate, a significantly larger amount of

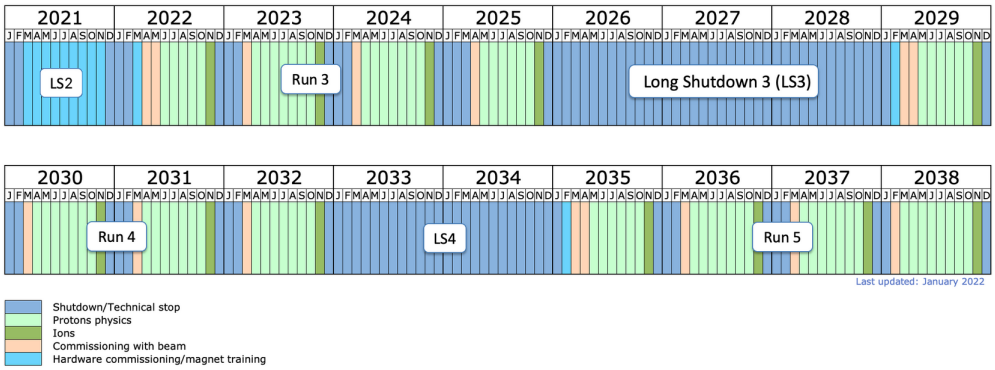

Figure 4.1: Long term LHC schedule.

data will be processed and selected, therefore the readout of all detectors was upgraded together with the online and offline systems.
However, since the results shown in this thesis work have been obtained processing data collected during the LHC Run 2 (2015-2018), the following sections provide a description of the configuration ALICE had in that period, and therefore before the upgrades occurred.

4.1 The ALICE Detector

The full description of the ALICE apparatus and its performance (before LS2) can be found in [45, 46]. In general the ALICE detector can be divided into two parts: the central barrel, composed of detectors mainly devoted to the study of hadronic signals, and the forward muon spectrometer, devoted to the study of quarkonia states. A schematic view of the ALICE detector is shown in Fig.4.2. The main sub-detectors involved in resonance analyses are the Inner Tracking System (ITS), the Time Projection Chamber (TPC), the Time Of Flight detector (TOF), and the V0A and V0C scintillators. Therefore they need a more specific description.

4.1.1 The Inner Tracking System (ITS)

The ITS [47] is the detector closest to the interaction point, directly surrounding the beam pipe. It is essential in the determination of the primary and secondary vertices, covering the region of radius between 4 and 43 cm (the

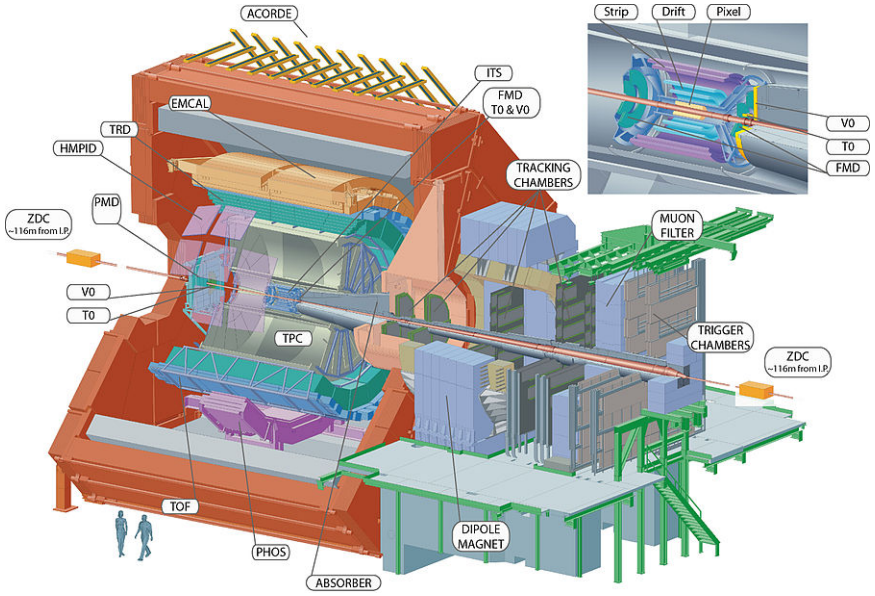

Figure 4.2: ALICE detector layout.

beam pipe is 800 μm thick and has a radius of 2.9 cm). The ITS consists of three concentric cylindrical detectors, each one composed of two layers, based on three different types of silicon detectors: pixels (SPD), drifts (SDD), and strips (SSD), passing from the inner layer to the outer one (Fig. 4.3). It allows fast response (of the order of tens of μs) and spatial resolution around 100 μm. It is also devoted to track and identify particles with momentum below 200 MeV/c, and to improve the momentum and angle resolution for particles reconstructed by the TPC. With the exception of the two innermost pixel planes, all layers have analog readout for particle identification (PID) via energy loss ($\mathrm{d}E/\mathrm{d}x$) measurement in the non-relativistic region.

The Silicon Pixel Detector (SPD)

The ITS innermost planes have to operate in a region where the track density could exceed 50 tracks/cm^2. The granularity required to cope with this challenge is achieved with the Silicon Pixel Detector (SPD). The SPD is based on hybrid silicon pixels, consisting of a two-dimensional matrix (sensor ladder) of reverse-biased silicon detector diodes bump-bonded to readout chips. The price to pay for the use of a silicon detector with very high segmentation is a large increase in the number of connections and electronics channels.

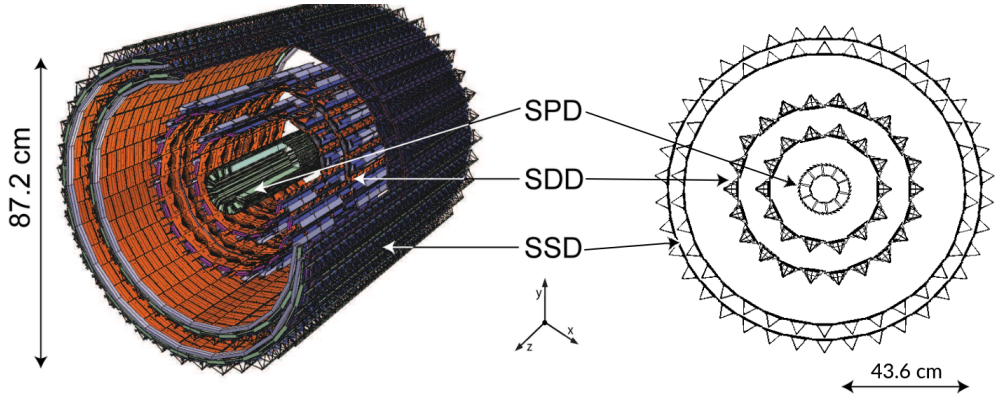

Figure 4.3: The ALICE ITS made up of Silicon Pixel Detector (SPD), Silicon Drift Detector (SDD), and Silicon micro-Strip Detector (SSD).

Each diode is connected through a conductive solder bump to a contact on the readout chip corresponding to the input of an electronics readout cell. Usually, the information provided is binary: a threshold is applied to the preamplified and shaped signal, and a true digital output is given if the threshold is exceeded. The basic detector module is the half-stave which consists of two ladders, one Multi-Chip Module (MCM) and one high density aluminium/polyimide multi-layer interconnect. The ladder consists of a silicon sensor matrix bump bonded to 5 front-end chips. The sensor matrix includes 256×160 cells measuring 50 μm (rφ) by 425 μm (z). Longer sensor cells are used in the boundary region to ensure coverage between readout chips. The sensor matrix has an active area of 12.8 mm (rφ) × 70.7 mm (z). The front-end chip reads out a sub-matrix of 256 (rφ) × 32 (z) detector cells. In total, the SPD (60 staves) includes 240 ladders with 1200 chips for a total of 9.8 × 10^6 cells. The inner (outer) SPD layer is located at an average distance of 3.9 cm (7.6 cm) from the beam pipe.

The Silicon Drift Detector (SDD)

The Silicon Drift Detector (SDD) forms the two intermediate ITS layers, with an expected charged particle density of 7 tracks/cm^2. It has a very good multitrack capability and provide two out of the four dE/dx samples needed for the PID with the ITS. The SDD, like gaseous drift detectors, exploits the measurement of the transport time of the charge deposited

by a travelling particle in order to identify the interacting point in one of the dimensions. The SDD is based on modules with a sensitive area of 70.17 (rφ) $\times$ 75.26 (z) mm^2, which is divided into two drift regions where electrons move in opposite directions under a drift field of $\sim$ 500 V/cm. The SDD modules are mounted on a linear structure called a ladder that has a series of parallel implanted p^+ field strips, connected to a voltage divider on both surfaces of the high-resistivity n-type silicon wafer. The voltage divider is integrated on the detector substrate itself. The field strips provide the bias voltage to fully deplete the volume of the detector and they generate an electrostatic field parallel to the wafer surface, creating a drift region. The coordinate perpendicular to the drift direction is given by the centroid of the collected charge. The coordinate along the drift direction is obtained from the measured drift time with respect to the trigger time. To obtain this information, a precise knowledge of the drift speed is needed. It has been measured during frequent calibration runs, given its strong dependence from the humidity and temperature gradients in the SDD volume. The SDD inner layer is made of 14 ladders with 6 modules each, the outer layer has 22 ladders, each of them with 8 modules.

Silicon micro-Strip Detector (SSD)

At larger radii, the requirements in terms of granularity are less stringent, therefore double-sided Silicon Strip Detectors (SSD) are used for the outermost ITS layers. The SSD is crucial for matching the track information from the TPC. In addition it provides $\mathrm{d}E/\mathrm{d}x$ measurement to help in the PID of low-momentum particles. In both SSD layers the detector modules are supported by lightweight carbon fibre structures, similar as those supporting the SDD. Each module is composed of a double-sided SSD connected to the front-end electronics (FEE). The FEE chips are hosted on a ceramic hybrid which serves as a mechanical support and conducts the heat produced by the chips to the cooling system. The sensors are 300 μm thick and count 768 strips on each side with a pitch of 95 μm with an active area of 73 (rφ) $\times$ 40 (z) mm^2. The innermost SSD layer consists of 34 ladders, each of them containing 22 modules while the other SSD layer has 38 ladders with 25 modules each.

In summary the Inner Tracking System (ITS) of ALICE is one of the central detectors used for tracking purpose, particle identification, and vertexing. Track finding is done combining the information by both the TPC and the

ITS. The PID is performed by different detectors in different momentum regions. In particular the $\mathrm{d}E/\mathrm{d}x$ measurement of the outer four layers of the ITS contributes to PID in the lower momentum range (i.e. up to 200 MeV/c). Finally vertex finding is unique to the ITS, as this detector was optimized to provide the measurement of the distance of the closest approach between the track extrapolation and the primary vertex (track impact parameter) with high resolution. Figure 4.4 shows an example of the PID capabilities of the ITS for Pb–Pb at $\sqrt{s_{\mathrm{NN}}} = 5.02$ TeV.

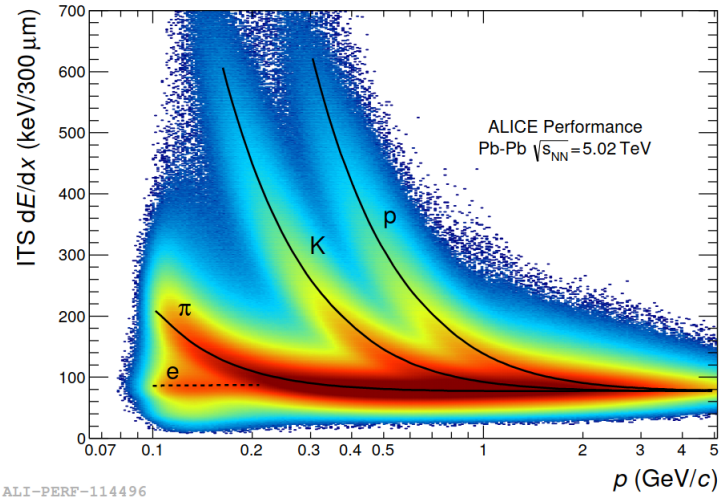

Figure 4.4: Charged particles $\mathrm{d}E/\mathrm{d}x$ distribution as a function of their momentum for ITS pure standalone tracks, measured in Pb–Pb collisions at $\sqrt{s_{\mathrm{NN}}} = 5.02$ TeV. The lines are a parametrization of the detector response based on the Bethe-Bloch formula.

4.1.2 The Time Projection Chamber (TPC)

Track finding in heavy-ion collisions is a big challenge, because of the extremely high track density. The need for a large number of points on each track has led to the choice of a Time Projection Chamber (TPC) as the main tracking detector, covering the pseudorapidity range $|\eta| < 0.9$. The inner radius ($\mathrm{r_{in}} \simeq 90$ cm) of the ALICE TPC [48] is given by the maximum acceptable hit density, while the outer radius ($\mathrm{r_{out}} \simeq 250$ cm) is determined by the minimum length required for a $\mathrm{d}E/\mathrm{d}x$ resolution better than 10%.

At smaller radii, and therefore larger track densities, tracking is performed by the ITS. The TPC has a cylindrical shape with an overall length along the beam direction of 500 cm. Thanks to its resolution the TPC, in addition to track finding, can be used for PID in the region of the relativistic rise, up to momenta of order of tens GeV/c. The detector design, as well as the choice of the operating gas-mixture, are optimized to guarantee a good double-track resolution and to keep as low as possible the material budget in order to ensure minimal multiple scattering and low secondary-particle production. The detector volume was filled with a gas-mixture of Ne/CO_2 (90%/10%), then Neon has been replaced by Argon during Run 2 [49]. The TPC field cage provides a uniform electrostatic field to transport primary charges towards the end-plates, where Multi Wire Proportional Chambers (MWPCs) with cathode pad readout are mounted. For reasons of symmetry in colliding beam arrangements, back-to-back field configuration is chosen in the common gas volume and with a common central high-voltage (HV) electrode that separates the detector into two halves (see Fig. 4.5).

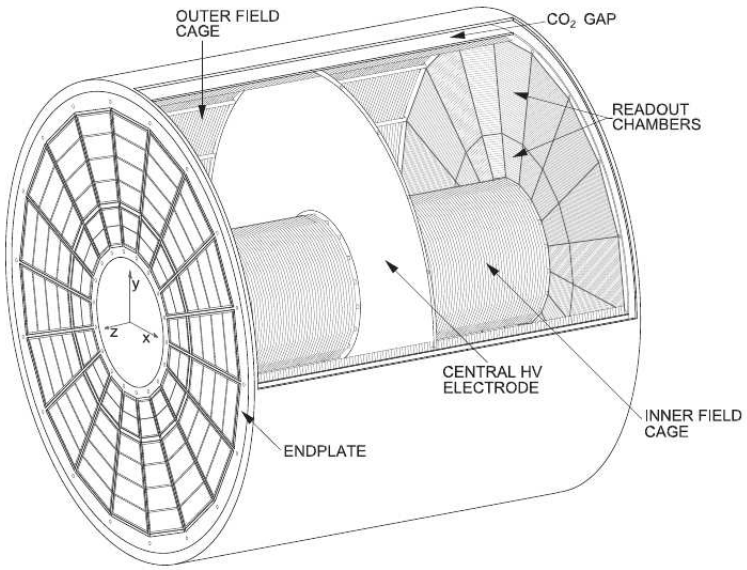

Figure 4.5: Schematic drawing of the ALICE TPC.

Because of the gas mixture used and the high rate capability needed, the field cage of the TPC has to run at voltage gradients of 400 V/cm, implying HV of 100 kV at the central electrode (250 cm drift length), which results in

a maximum drift time of about 90 μs (electron drift velocity $\sim$ 2.7 cm/s). The charge collected in the TPC readout pads is used to measure particle energy loss. An example of the TPC PID performance is shown in Fig. 4.6.

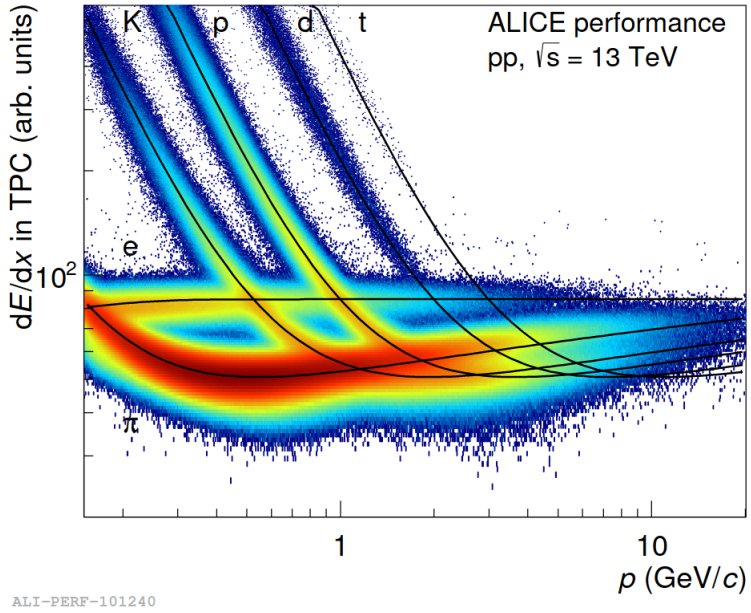

Figure 4.6: Charged particles $\mathrm{d}E/\mathrm{d}x$ distribution as a function of their momentum for TPC tracks measured in pp collisions at $\sqrt{s} = 13$ TeV. Lines are the Bethe-Bloch fits (see section 4.2.4).

4.1.3 The Time Of Flight (TOF) Detector

The Time-Of-Flight (TOF) detector [50] is a large area array that covers the central pseudo-rapidity range ($|\eta| < 0.9$) for PID in the intermediate momentum range, below 2.5 GeV/c for pions and kaons, up to 4 GeV/c for protons. The TOF, coupled with the ITS and the TPC, is able to identify event-by-event a large samples of pions, kaons, and protons in the low-momentum range. TOF employs Multigap Resistive Plate Chambers (MRPCs), gaseous detectors with glass resistive electrodes and multiple gas gaps. The electric field in these chambers is high and uniform in the whole sensitive gaseous volume of the detector. Any ionization produced by a traversing charged particle immediately starts an avalanche process which generates the ob-

served signals on the pick-up electrodes. The whole detector is embed in a cylindrical structure with an internal radius of 370 cm and an external one of 399 cm. The basic unit of the TOF system is a 10-gap double-stack MRPC strip (see Fig. 4.7) that measures 122 cm length and and 13 cm width, with an active area of 120×7.4 cm^2 divided into two rows of 48 readout pads of 3.5×2.5 cm^2.

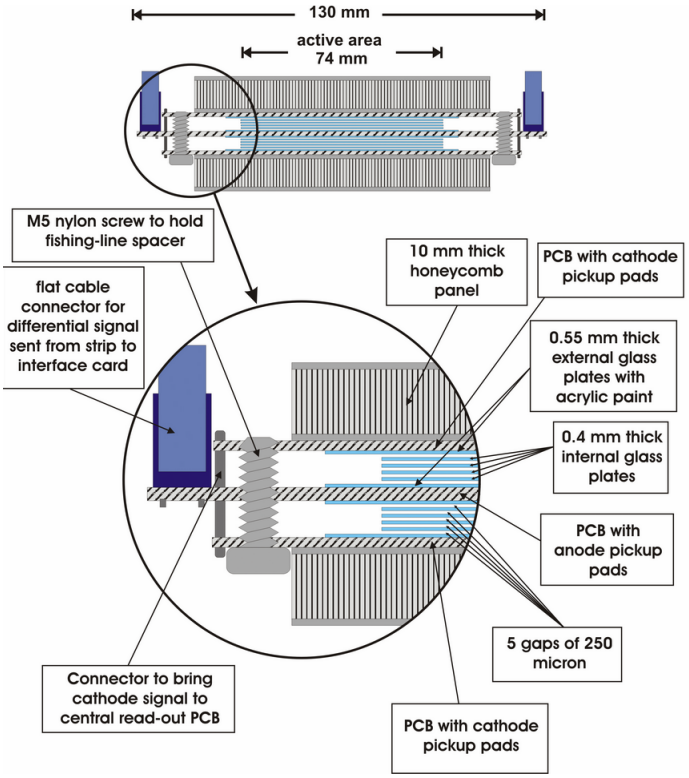

Figure 4.7: Schematic cross section of a 10-gap double-stack MRPC strip of the ALICE TOF detector.

The overall TOF length is 741 cm (active region) and consists of 90 modules. Each module of the TOF detector includes a group of MRPC strips closed inside a box that isolates the gas volume and supports the external front-end electronics. The total number of MRPC strips is 1638 for a total of 157248 readout pads covering an active area of 141 m^2. This highly segmented structure allows to have low occupancy and good performance also in a high multiplicity environment. The intrinsic time resolution of the MRPC is

lower than 50 ps with an efficiency close to 100%. The gas mixture flowing in the detector is composed of $C_2H_2F_4$/i-C_4H_{10}/SF_6 (90%/5%/5%) with an operating voltage equal to 13 kV. An example of TOF performance is shown in Fig. 4.8.

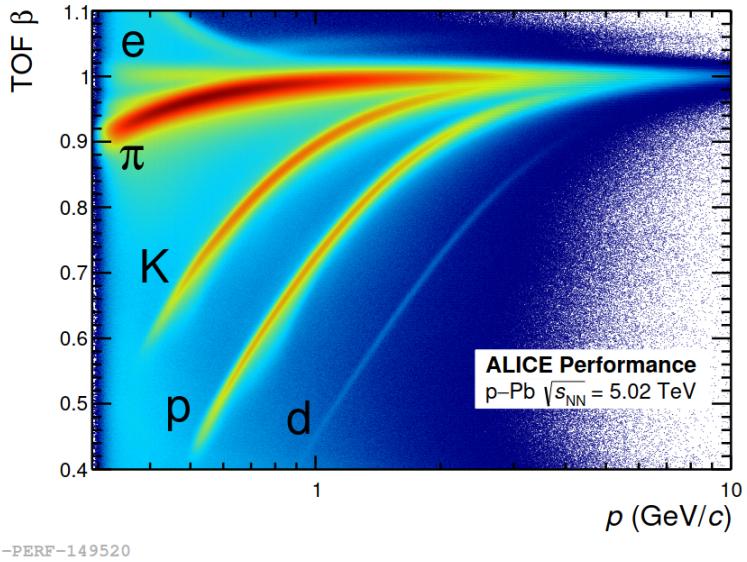

Figure 4.8: TOF β vs momentum performance plot in p–Pb at $\sqrt{s_{\rm NN}} =$ 5.02 TeV. The visible bands are from e, π, K, p and d.

4.1.4 The V0 Detector

The V0 detector [51] is a small angle detector consisting of two arrays of scintillator counters, called V0A and V0C, that are placed on either side of the ALICE interaction point (IP) used for global event characterization and triggering. The detector system has several functions: it provides minimum-bias (MB) triggers for the central barrel detectors, derives the collision centrality, and gives information about the beam luminosity. The triggers are obtained from particles created in the initial collisions and from secondaries produced in the vacuum chamber elements. Therefore the trigger efficiency and the charged-particle multiplicity distributions are slightly different from those expected considering pure collisions. However, since there is a monotone dependence between the number of particles detected by the V0 arrays and the number the primaries emitted, the V0 provides an indicator of the collision

centrality through the multiplicity measured in the event [52]. There are three centrality triggers: multiplicity (MT), semi-central (CT1), and central (CT2). They are selected applying cuts on the number of the fired counters and the total charge deposited. In normal operation both arrays are required (AND mode) to provide the triggers: MB, MT, CT1 and CT2. An OR mode can also be used. In pp collisions, the efficiency for the detection of at least one charged particle detected in both sides is about 77% when no secondary particle is taken into account. It raises up to 83% when the ALICE environment effects are introduced. Finally, the V0 detector participates in the measurement of luminosity in pp collisions with a precision of about 10%. V0 system plays also an important role in rejecting undesired background. Indeed it is able to discriminate beam-gas from beam-beam events by measuring the time-of-flight difference between the V0A and V0C arrays. A cut at $\sim$ 10 ns allows to reject $\sim$ 99% of the background triggers. Fig. 4.9 shows an example of the time correlation between the two V0 arrays.

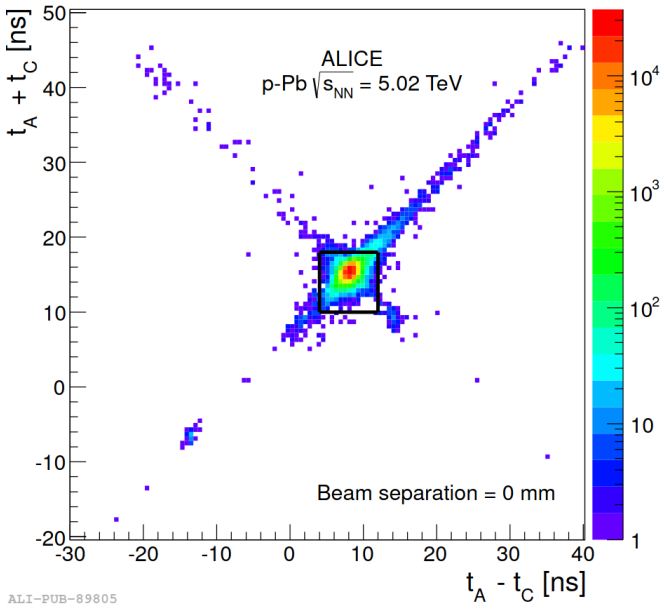

Figure 4.9: Correlation between the sum and difference of arrival times (relative to the bunch crossing) on the two V0 arrays in p–Pb collisions at $\sqrt{s_{\rm NN}} = 5.02$ TeV. Events inside the squared region are considered as beam-beam interactions [53].

The V0A detector is placed 340 cm from the IP on the side opposite

to the forward muon spectrometer (FMS), while the V0C is located 90 cm from the IP in a opposite position to the V0A and in front of the hadronic absorber of the FMS. They cover the pseudo-rapidity ranges $2.8 < \eta < 5.1$ (V0A) and $-3.7 < \eta < -1.7$ (V0C) and each array consists of 32 counters distributed in 4 rings (Fig. 4.10).

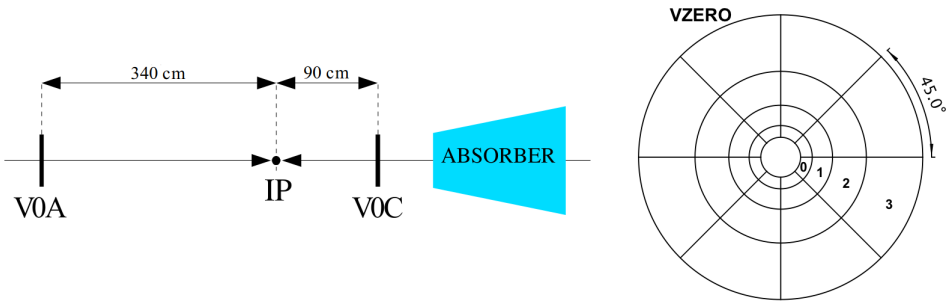

Figure 4.10: Plane view of the placement of V0 on both sides of the ALICE IP; the hadronic absorber of the FMS is also shown (**left**). Segmentation of the V0A/V0C arrays (**right**).

The material consists of BC4041 scintillating material (2.5 and 2.0 cm in thickness for V0A and V0C respectively) with 1 mm in diameter BCF9929A Wave-Length Shifting (WLS) fibres. The time resolution of each counter is better than 1 ns. Two types of triggers are provided from each array. The first one is based on pre-adjusted time windows in coincidence with the time signals from the counters. MB and MT triggers are obtained using this method. The second type of triggers is based on the total charge collected by the arrays. The two Centrality Triggers are built starting from these quantities.

Centrality/Multiplicity measurement

The determination of the multiplicity of a given collision is fundamental to achieve information on the impact parameter b. It will be large when b is small, with a large numbers of N_{part} and therefore a large number of particles produced, vice-versa when b is large. Collisions with small b are referred as central, i.e. head-on events, while collisions with large b are referred as peripheral. Centrality is used to characterize the amount of nuclear overlap in the collisions. It is commonly expressed in percentiles of the total nucleus-nucleus cross section. Small (large) percentiles, like 0-5% (80-100%),

correspond to central (peripheral) collisions (Fig. 4.11). The particle multiplicity measured at forward rapidity in the V0 is strongly correlated with the multiplicity of charged particles measured at midrapidity. The V0 estimator is the most common choice for centrality classification for the purpose of studying particle production at midrapidity, alternatively centrality can be measured by the energy deposited by the spectator nucleons in the Zero Degree Calorimeter (ZDC) [54]. As shown in Fig. 4.11, the centrality classes are defined by slicing the V0M signal amplitude distribution, fitted with a Glauber model coupled to a model for particle production based on a negative binomial distribution (NBD).

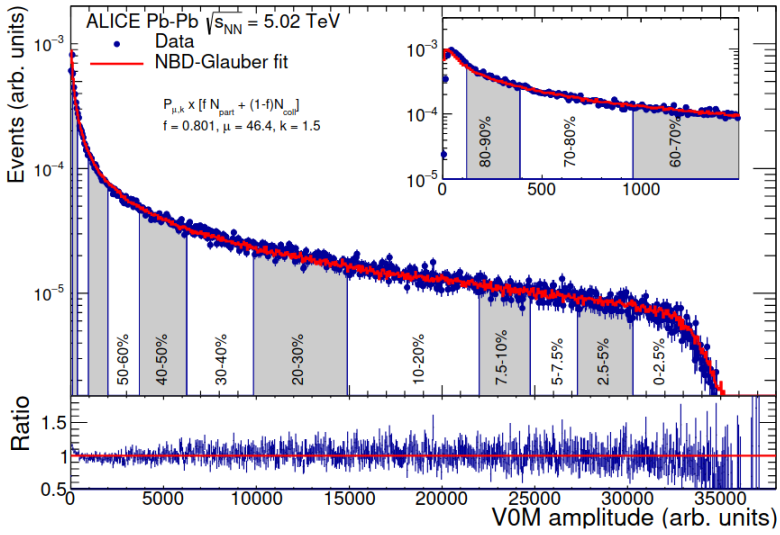

Figure 4.11: Summed signal amplitude in the V0 scintillators in Pb–Pb collisions at $\sqrt{s_{\mathrm{NN}}} = 5.02$ TeV. The red line is the fit to the V0M distribution with a Glauber model coupled to a negative binomial distribution (NBD). Gray and white bands indicate the classification of the events into centrality classes, with centrality expressed in percentile of the hadronic cross section [55].

Unlike heavy-ion collisions, high multiplicity events in pp and p–Pb collisions are not expected to come from an increase in the amount of matter involved in the collision. This is obvious in the case of pp collisions where N_{part} is always 2. Instead, since the initial volume is roughly fixed, high multiplicity events may result as a consequence of another mechanism. Con-

sidering pp collisions, it is generally accepted in models that initial scatterings give rise to some number of subnuclear interactions (MPIs) that produce the observed hadrons. They can vary from hard partonic interactions producing many particles, to soft interactions resulting into few hadrons. Therefore a specific event multiplicity can result from several different combinations depending on the number of MPIs, their hardness and the hadronization effects. In summary nucleus-nucleus colisions are usually considered as multiple interactions of individual nucleons, while pp collisions are characterized by multiple interactions of partons. The p–Pb collisions act as a bridge between this two limit cases.
Fig. 4.12 shows the event multiplicity distribution in pp collisions sliced into multiplicity classes expressed in percentiles, as for centrality classes in Pb–Pb collisions. In this case low (high) percentiles, like 0-1% (70-100%), refers to high (low) event multiplicity.

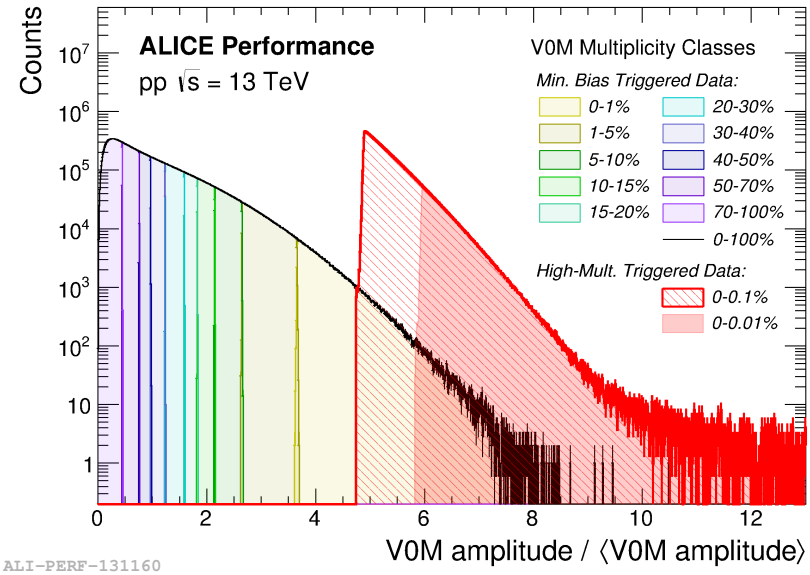

Figure 4.12: V0M/<V0M> distributions for V0M multiplicity classes compared between MB and High Multiplicity triggers in pp collisions at $\sqrt{s} = 13$ TeV [56].

The measurement of the charged-particle pseudorapidity distribution is performed thanks to the reconstruction of tracklets, built considering the positions of the reconstructed primary vertex and two hits (one on each layer)

in the SPD layers of the ITS. Thanks to this technique, charged particles with $p_{\mathrm{T}} > 50$ MeV/c are reconstructed. This cut-off is determined by particle absorption in the material. The charged-particle pseudorapidity density is obtained from the measured distribution of the tracklets $\mathrm{d}N_{\mathrm{tracklets}}/\mathrm{d}\eta$ as:

$$\frac{dN_{ch}}{d\eta} = \alpha(1-\beta)\frac{dN_{tracklets}}{d\eta} \tag{4.1}$$

where α accounts for the acceptance and efficiency for a primary particle to produce a tracklet, and β is the contamination of reconstructed tracklets from combinations of hits not produced by the same primary particle [57]. In order to classify the collisions in percentiles of the hadronic cross section using the charged particle multiplicity, it is necessary to know the particle multiplicity at which the purity of the event sample and the efficiency of the event selection becomes 100%. Then the Anchor Point (AP) is defined: it represents the amplitude of the VZERO detector equivalent to 90% of the hadronic cross section, which determines the absolute scale of the centrality. The percentile of the hadronic cross section is determined for any value of the VZERO amplitude by integrating the measured VZERO amplitude distribution normalized at the anchor point V0AP (i.e. 90% of the hadronic cross section). For example if V is the VZERO amplitude, the top 10% central class is defined by the boundary $\mathrm{V0}_{10}$ which satisfies [58]:

$$\frac{\int_{\mathrm{V0}_{10}}^{\infty}(dN_{\mathrm{evt}}/dV)dV}{\int_{\mathrm{V0}_{\mathrm{AP}}}^{\infty}(dN_{\mathrm{evt}}/dV)dV} = \frac{1}{9} \tag{4.2}$$

4.2 ALICE Offline Software Framework

Thanks to the offline framework data processing is possible. This includes tasks as calibration, alignment, simulation, reconstruction and analysis of the raw data. This is the final step of the experimental chain, the time of interpreting the collected data and understanding the physical meaning associated. In an experiment of the complexity and dimension of ALICE the amount of data recorded are such that the computing power of a single computing centre is not enough to process them. For this reason institutes that are part of the ALICE collaboration created a Grid [59] of several computing sites located worldwide, working as an integrated computing centre whose resources can be shared and employed by the entire collaboration. Fig. 4.13

shows the worker nodes of the ALICE Grid sites located around the Globe. Currently the ALICE Grid consists of about 170 sites located in more than 40 countries.

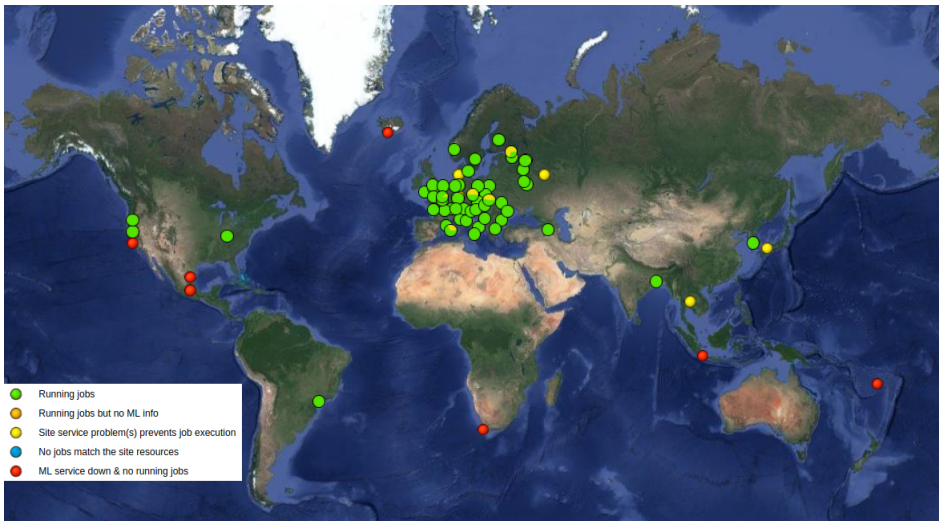

Figure 4.13: ALICE Grid computing centers.

4.2.1 The ALICE Environment (AliEn) Framework

Softwares that makes the Grid concept possible are called middleware. Since 2001, ALICE has developed a Grid middleware called AliEn ((Alice Environment). It permits to the ALICE users to connect to the ALICE Grid, guarantying transparent access to the computing resources distributed worldwide through a single interface. Users interact with the Grid through the AliEn User Interface (UI) shielding them from the Grid complexity and heterogeneity. AliEn consists of the following components and services:

- **Authentication:** AliEn supports various authentication schemes, implemented using the Simple Authentication and Security Layer (SASL) protocol, in particular GLOBUS GSI/GSSAPI that makes it compatible with the Worldwide LHC Computing Grid (WLCG) security model.

- **Authorization and auditing services:** The authorization in AliEn is similar to any UNIX-like system. Files have read, write and execution

permissions, and they can be set for the owner of the file, group, or world. Every task (namely *job*) submitted and executed in AliEn is tracked with a unique identifier. The information on all active jobs can be found in the AliEn task queue database. Then all completed jobs are moved to an archive database.

- **Workload and data management:** A central service manages all the tasks, while computing elements can provide access to a single machine, a cluster of computers, or even an entire foreign Grid. When jobs are submitted, the workload manager optimizes the queue of the tasks taking into account job requirements, depending on input files, CPU time, architecture, disk space, etc. When a job requires several files, the workload management systems splits the job into several sub-jobs, each of them referring files that are located in the same Storage Element (SE). The workload management system still treats the job as a single task keeping track of each individual sub-job.

- **File and metadata catalogues:** Input and output associated with any job are registered in the AliEn File Catalogue, a virtual file system in which a file or data set are identified by a Globally Unique IDentifier (GUID). The file catalogue does not own the files, it only keeps an association between the Logical File Name (LFN) and the Physical File Name (PFN) on a real file or mass storage system. PFNs describe the physical location of the files and include the name of the AliEn storage element and the path to the local file. Usually data in the File Catalogue are organized by year, accelerator period and run.

- **Information service:** The Information Service (IS) keeps track of the status, type and capabilities of all AliEn services, central and at the sites. This way, the clients can figure out the best place to store files according to their needs.

- **Job monitoring services:** Monitoring in AliEn is based on the MonALISA (Monitoring Agents in A Large Integrated Services Architecture) framework [60]. A global view of the entire AliEn Grid, as well as long term persistence of the data is assured by the MonALISA repository. This service subscribes to general interest data and stores them into a database. It offers both near real-time and history views, with different levels of detail, down to individual user jobs.

Fig. 4.14 offers a schematic view of the AliEn services.

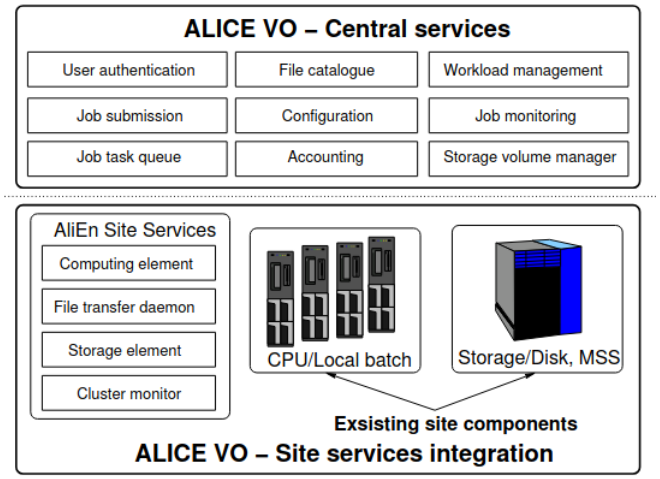

Figure 4.14: Schematic view of the AliEn basic components.

AliEn provides a functional computing environment fulfilling the needs of the ALICE experiment. As the first step, the analysis framework extracts a subset of the dataset from the File Catalogue using meta-data selection. Then the framework negotiates with dedicated Grid services the balancing between local data access and data replication. Once the distribution is decided, the analysis framework creates sub-jobs. The framework collects and merges the results from all completed sub-jobs on request. An analysis object associated with the analysis task remains persistent in the Grid environment so the user can go offline and reload an analysis task at a later date, check the status, merge current results, or resubmit the same task with a different analysis code.

4.2.2 The AliRoot Framework

Usually data are processed using an Object-Orientated (OO) framework called ROOT [61] developed at CERN since 1994. It is based on C++ language and it was designed as a specific tool for high energy physics analysis. The ALICE experiment in particular uses an extension of ROOT called AliRoot, that includes all the geometrical and working features of ALICE. The AliRoot framework is shown schematically in Fig. 4.15 and it is used for sim-

ulation, alignment, calibration, reconstruction, visualization and analysis of the experimental data.

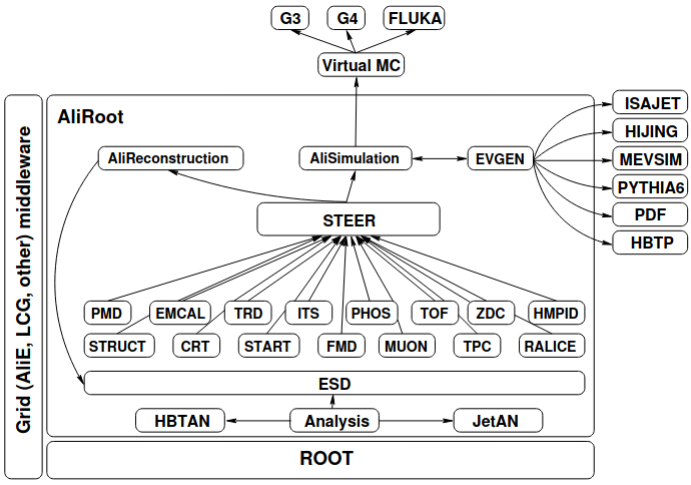

Figure 4.15: Schematic view of the AliRoot framework

The basic design features of the AliRoot framework are modularity and re-usability. Modularity allows to replace parts of the system minimizing or even eliminating the impact on the rest. For example, it is possible to change the event generator, the transport Monte Carlo or the reconstruction algorithms for each sub-detector without affecting the code by mean of abstract interfaces. In addition the codes for each sub-detector are independent so that different detector groups can work simultaneously on the system with minimum interference. Re-usability guarantees the protection of the large amount of scientific knowledge achieved thanks to the ALICE programmers. It is meant to maintain the maximum amount of backward compatibility as the system evolves. For example in the context of event simulation, the role of the AliRoot framework can be schematized as following:

- **Event generation:** data produced by the event generators interfaced with AliRoot are stored in a tree container, where all the information related to the generated particles (such as type, momentum, charge, originating particle and decay products) are hierarchically ordered.
- **Transport and detector response:** during the transport, the motion of the particles through the detector structure and its response

are simulated. For all interactions of the traversing particle with the detector active areas, the hits (energy deposition at a given point and time) are stored for each sub-detector. Then particles information is completed by the *track references*, a tag for the tracks they belong to.

- **Digitization:** the hits are converted into digital outputs, taking into account the detector response function. Then the digits are stored in the specific hardware format of each sub-detector as raw data.

At this point the reconstruction chain can start and finally the reconstructed particles are compared to the Monte Carlo generated ones.

4.2.3 Event Reconstruction

The ALICE reconstruction code is part of the AliRoot framework. The input for the reconstruction sequence are the digits in the form of raw data, coming from the real detector or generated from MC simulation. The reconstruction chain is identical, both for simulated and real data (Fig. 4.16).

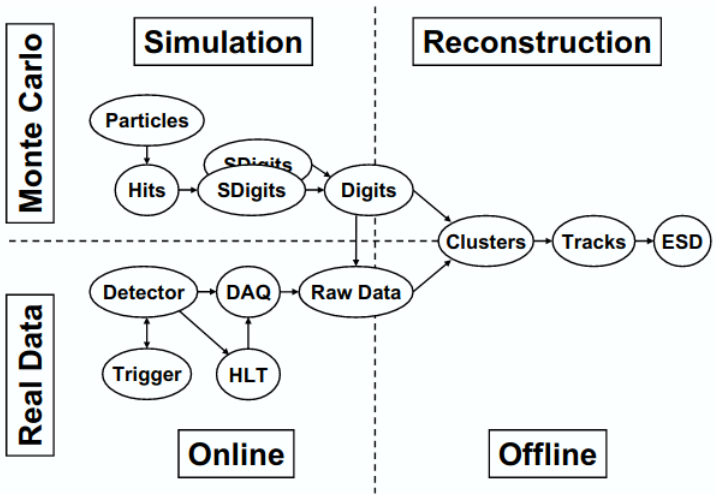

Figure 4.16: Interplay between the reconstruction phase and the other parts of AliRoot.

The output of the whole reconstruction operation is the Event Summary Data (ESD) that contains all the information about the charged particle tracks and identification, particle decays with their vertex (V^0), and neutral

particles reconstructed in the calorimeters. The full sequence consists of the following main steps:

- **Primary vertex reconstruction:** a charged particle going through the detectors leaves a number of discrete signals that measure the position of the points in space where it has passed. These space points are reconstructed by a detector specific cluster-finding procedure. To the estimation of each space point position is associated the corresponding uncertainty, parameterized in detail for all the central detectors (ITS, TPC, TRD). The space points and the associated uncertainties are then passed to the track reconstruction. The position of the primary vertex can be computed before track finding by a correlation of the space points reconstructed in the two pixel layers of the ITS. A precision of ~ 5 μm along the beam direction and ~ 25 μm in the transverse plane is achieved for the high multiplicity events [62]. The information on the primary vertex position and its uncertainty is then used during the track finding (seeding and applying the vertex constraint) and for the secondary vertex reconstruction.

- **Track selection and particle identification:** track reconstruction in ALICE is based on the Kalman filter[1] approach [63]. The seed for starting the Kalman process is built from the primary vertex information of the previous step. Track finding starts from the outermost pad rows of the TPC, proceeding to the inner part. Different combinations of the pad rows are used with and without a primary vertex constraint. Usually more than one pass is done, starting with a rough vertex constraint, imposing the primary vertex with a resolution of a few centimetres and then releasing the constraint. Then the prolongation of each track reconstructed in the TPC is searched in the ITS, from the SSD layers down to the innermost SPD. If the prolongation is found, the track is then back-propagated and refitted from the innermost ITS layer proceeding with the Kalman filter in the outward direction, releasing the vertex constraint. In this way the track parameters and their covariance matrix at the outer TPC radius are obtained. If the

[1]The Kalman filter is a recursive algorithm that works as a two-phase process. In the first phase the Kalman filter produces estimates of the current state variables with their uncertainties. Once the next measurement is performed together with other uncertainties, these estimates are updated using a weighted average. The result is the new state estimate.

prolongation is not found, another pass is considered, in order to reconstruct the tracks coming from the secondary vertices well separated from the main interaction point. The Kalman filter continues into the TRD and then the tracks are matched toward the outer detectors: the TOF, HMPID, PHOS and EMCAL. The task of the final track reconstruction pass is to refit the primary tracks back to the primary vertex or, in the case of the secondary tracks (related to the decay products of unstable particles), as close as possible to the vertex. This is done again with the Kalman filter using the clusters found in all the detectors at the previous reconstruction passes. During this pass the secondary vertices are also reconstructed. Figure 4.17 shows the combined track finding in the central ALICE detectors.
If, in addition to the space point position, the detector is also able to measure the produced ionization, this information can be used for the particle identification. Using the PID information coming from the outer detectors (TRD, TOF, HMPID) and $\mathrm{d}E/\mathrm{d}x$ measured by TPC and ITS, ALICE is able to identify charged particles. The neutral particles in the central-rapidity region are identified by the calorimeters (PHOS and EMCAL). There is also the possibility to count photons in the forward region using the PMD.

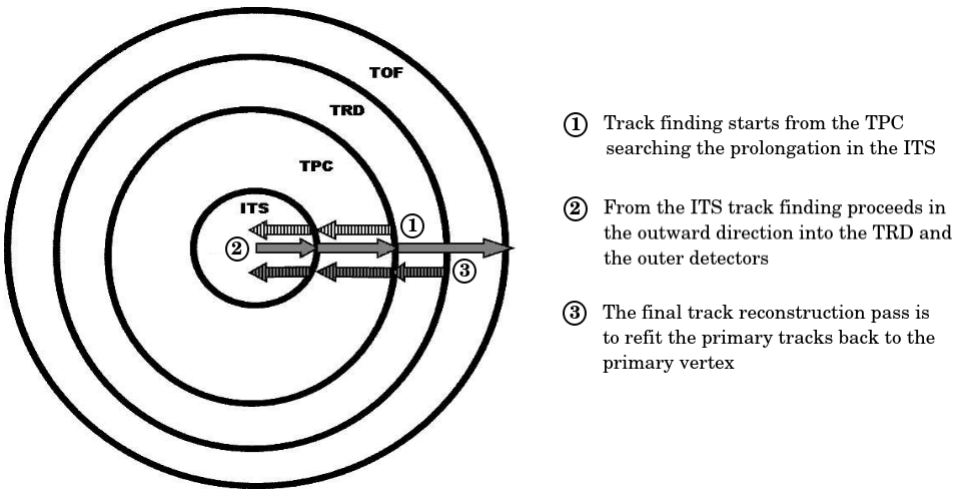

Figure 4.17: Schematic view of the track reconstruction in the central ALICE detectors.

- **Secondary vertex reconstruction:** once the tracks and the interaction vertex have been found, the search for secondary vertices from particle decays can be performed (Fig. 4.18). Secondary tracks are selected applying cuts on the distance of closest approach (DCA) with respect to the primary vertex. In particular tracks with DCA lower than a certain minimum value (0.5 mm in pp and 1 mm in Pb–Pb) are rejected. Then combination of each selected track with all other having opposite charge (unlike-sign pair) are considered applying further cuts. The DCA between the two tracks is calculated and if its value is too large (> 1.5 cm) the pair is rejected. The half-point at the minimum DCA, called also point of closest approach (PCA), is the localization of the secondary vertex of the V^0 candidates. Only vertices inside a fiducial volume are kept and the PCA is requested to be closer to the interaction vertex than the innermost hit of either of the two tracks. Then a cut on the cosine of pointing angle θ between the V^0 momentum vector ($\vec{p}_{\mathrm{pair}}$) and the straight line connecting the primary and secondary vertices is applied (usually > 0.9).

For events with low track multiplicity, the track reconstruction efficiency is close to 100% for tracks with momentum above 0.2 GeV/c. For high track densities ($\mathrm{d}N_{\mathrm{ch}}/\mathrm{d}\eta \geq 6000$), the efficiency is lower and decreases with decreasing momentum. The possibility of fake-track reconstruction is considered to be the main cause of this decrease, reaching a probability of 10% at 0.2 GeV/c for wrong cluster assignment. The overall software track finding efficiency, neglecting detectors dead zones and particle decays and interactions in the material is higher than 90% over the full momentum range. The real track-finding efficiency, including these effects, is lower and depends on the combination of detectors used in the reconstruction chain [64].

4.2.4 Particle identification with the TPC

The ALICE detector employs different subsystems for identifying charged hadrons. The ITS (the outer four layers), the TPC, the TOF, and the HMPID detectors are used for hadrons identification each with a different momentum-dependent performance and with different techniques: energy loss ($\mathrm{d}E/\mathrm{d}x$), time of flight, and Cherenkov radiation characteristics. The hadron identification systems is also used to identify electrons. In addition, the calorimeters (PHOS and EMCal) and the TRD provide a dedicated elec-

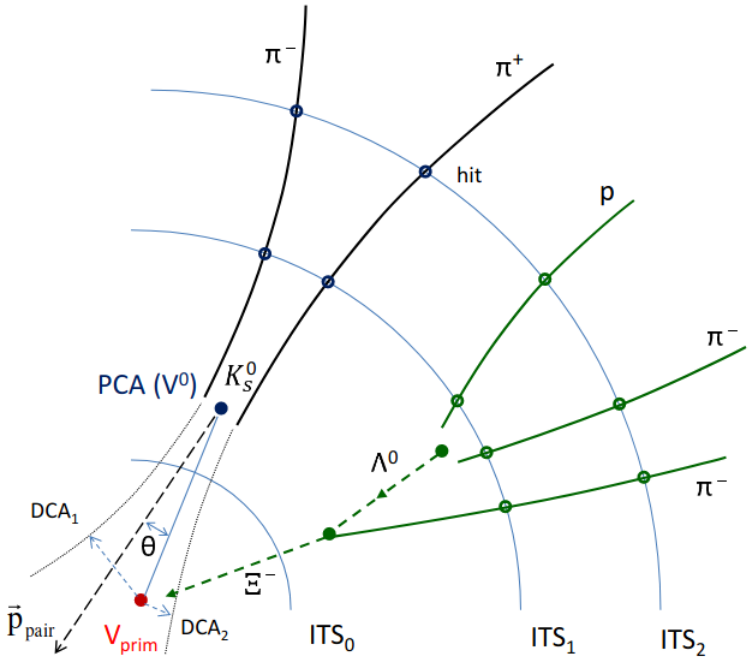

Figure 4.18: Example of secondary vertex reconstruction procedure for K^0_S and Ξ^- decays. For simplicity the decay points are arbitrarily placed between the first two ITS layers (radii are not to scale). The solid lines are the reconstructed charged particle tracks, extrapolated to the secondary vertex candidates. The dashed lines represents the extrapolations to the primary vertex and auxiliary vectors. [46].

tron identification. The information provided by each detector can be used individually or combined. The ALICE experiment is able to identify particles with a very low momentum, from about 0.1 GeV/c where the ITS is used for standalone tracking, up to tens GeV/c by using the dE/dx in the TPC [46]. Particles can be directly identified or reconstructed. In the first case more stable particles like $e^{\pm}$, $\pi^{\pm}$, $K^{\pm}$, $p^{\pm}$ are identified at track level using mass-dependent signals such as dE/dx, TOF and Cherenkov radiation. Instead unstable particles are identified through their decay topology and reconstructed via invariant mass computation of their decay products. This technique is used for strange hadrons, such as K^0_S, Λ, and the multi-strange baryons Ξ and Ω, as well as for hadronic resonances. In this scenario the direct identification of the daughter particles plays an important role in order to reduce

the background contribution.
The TPC provides information for particle identification over a wide momentum range. Charged particles traversing the gas-filled volume of the TPC ionize the gas molecules. The mean energy loss per path length is given by the Bethe-Bloch equation:

$$-\left\langle \frac{dE}{dx} \right\rangle = k_1 \frac{Z}{A} \frac{z^2}{\beta^2} \left[\frac{1}{2} \ln(k_2 m_e c^2 \beta^2 \gamma^2) - \beta^2 + k_3 \right] \tag{4.3}$$

where:

- Z and A are the atomic and the mass number of the ionized gas, respectively;
- m_e is the electron mass;
- z is the electric charge of the ionizing particle in unit of the electron charge e;
- β is the ionizing particle velocity normalized to the light velocity c;
- $\gamma = 1/\sqrt{1-\beta^2}$ is the Lorentz factor;
- $\beta\gamma = p/Mc$ where M and p are the mass and the momentum of the ionizing particle, respectively;
- k_1, k_2, and k_3 are constants depending on the ionized medium.

As expressed in eq. 4.3, the energy loss of a charged particle crossing the detector depends on its velocity β which in turn depends only on the momentum and the mass of the ionizing particle. Since the momentum is known from the track curvature, the measured $\mathrm{d}E/\mathrm{d}x$ value allows to determine the particle mass and therefore its identity.
The general way to quantify the identification power of the TPC is to consider the difference of the mean energy loss in unit of resolution between the specific energy loss measured by the detector and the corresponding expected value predicted by the Bethe-Bloch parameterization:

$$N_\sigma = \frac{(dE/dx)_{measured} - (dE/dx)_{Bethe-Bloch}}{\sigma_{TPC}} \tag{4.4}$$

This permits also to choose the strictness for the particle identification by varying the value of N_σ.

4.2.5 Analysis Procedure

The analysis of experimental data is the final stage of event processing, devoted to extract the physics information. The analysis starts from the Event Summary Data (ESD) produced during the reconstruction process. The size of the ESD is about one order of magnitude lower than the corresponding raw data. During an analysis task, selected sets of events are processed. Their selection depends on the event topology and characteristics. This is done by choosing among the tag list in the database. Tags are created after the reconstruction step, they represent the physics quantities that characterize each run and event, containing also a unique ID of the ESD file. The analysis typically proceeds with a loop over all the events in the list with the calculation of the desired physics variables. Usually, for each event, there is a set of internal loops running on several reconstructed quantities such as tracks, V^0s, clusters, etc., in order to select the signal candidates. Inside each loop a number of criteria (cuts) are applied to limit undesired background combination together with the selection of the signal. The cuts can be based on geometrical aspects such as impact parameters of the tracks with respect to the primary vertex, distance between the cluster and the closest track, distance of closest approach between the tracks, angle between the momentum vector of the particle combination and the line connecting the production and decay vertices. They can also be based on kinematics quantities such as momentum ratios, minimal and maximal transverse momentum, angles in the rest frame of the combination. Other common cuts are also the particle identification criteria. After the optimization of the selection criteria, combined acceptance of the detector is taken into account. This is a analysis-specific quantity which depends on the geometrical acceptance, the trigger efficiency, the decays of particles, the reconstruction efficiency, the efficiency of the particle identification and of the selection cuts. Finally the last part of the analysis usually involves quite complex mathematical treatments and statistical tools, as the correction for systematic effects with the estimation of statistical and systematic uncertainties. In the next part the multiplicity dependent analysis of the $K^{*\pm}$ resonance production in pp collisions at $\sqrt{s} = 13$ TeV is discussed in detail.

Part III

MEASUREMENT OF $K^*(892)^{\pm}$ PRODUCTION

Chapter 5

Charged K* Resonance Reconstruction

The $K^*(892)^{\pm}$ is a resonance particle with a small lifetime (~ 4 fm/c), thus it can be used to study the competing re-scattering and regeneration effects occurring in the hadronic phase, which modify particle momentum distributions and yields after hadronization. Measurements of $K^{*\pm}$ in pp collisions can be used as a baseline to study the Pb–Pb collisions at the LHC energies and to provide a reference for tuning event generators. Moreover a particular interest in studying $K^{*\pm}$ as a function of charged-particle multiplicity arises from recent measurements of other resonance production in high-multiplicity pp and p–Pb collisions, which have shown the onset of phenomena typical of heavy-ion collisions even in those smaller collision systems (see section 3.2). In particular, there are hints of suppression of the $K^*(892)^0$/K ratio with increasing multiplicity [41], and the study of $K^{*\pm}$ production as a function of charged-particle multiplicity can provide further evidence to corroborate the observed trend. Indeed the inclusive analysis of $K^{*\pm}$ production in inelastic pp collisions [65] showed lower systematic uncertainties on $K^{*\pm}$ than K^{*0} results because of the different strategies used for the K^0_S and $K^{\pm}$ identification in ALICE ($K^{*\pm} \to \pi^{\pm} + K^0_S$ while $K^{*0} \to \pi^{\pm} + K^{\mp}$). Therefore $K^{*\pm}$ measurements can even improve the previous results for K^{*0} reaching higher precision thanks to smaller systematic uncertainties. In Tab. 5.1 the main identifying properties of $K^*(892)^{\pm}$ and $K^*(892)^0$ are listed.

This thesis describes the measurement of $K^*(892)^{\pm}$ mesons (in the following simply $K^{*\pm}$) produced at mid-rapidity ($|y| \leq 0.5$) in pp collisions at $\sqrt{s} = 13$ TeV as a function of the charged-particle multiplicity.

Table 5.1: Comparison between $K^*(892)^{\pm}$ and $K^*(892)^0$ properties [66].

Particle	$K^*(892)^{\pm}$	$K^*(892)^0$
Mass (MeV/c^2)	891.67 ± 0.26	895.55 ± 0.20
Width (MeV/c^2)	51.4 ± 0.8	47.3 ± 0.5
Decay	$K^0_S\pi^{\pm}$	$K^{\pm}\pi^{\mp}$
Branching Ratio	0.33	0.66
Lifetime (fm/c)	3.6	4.2

In this analysis, $K^{*\pm}$ has been reconstructed via its hadronic decay channel $K^{*\pm} \rightarrow \pi^{\pm} + K^0_S$ with the K^0_S (V^0) identified by its decay: $K^0_S \rightarrow \pi^+ + \pi^-$ (Fig. 5.1). The yields of $K^{*\pm}$ are extracted from πK^0_S invariant-mass distributions as a function of transverse momentum and for different multiplicity classes. The p_T spectra are integrated to obtain a measurement of the total dN/dy, and the mean transverse momentum $\langle p_T \rangle$ values are extracted from the spectra. Finally results are compared with the previous K^{*0} measurements obtained for the same collision system and energy, and with results from model calculations.

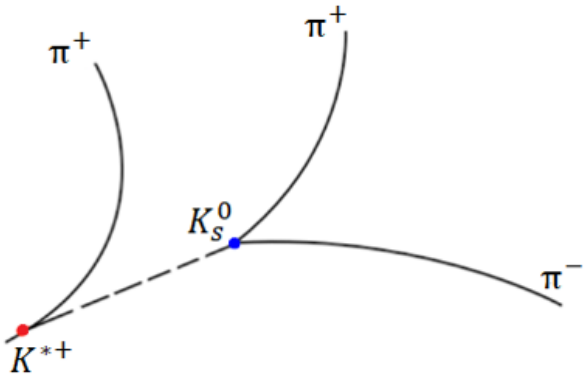

Figure 5.1: Decay topology of the $K^{*\pm}$ into a K^0_S and a charged π. The subsequent K^0_S decay into an oppositely charged pion pair is also shown.

Chapter 6

Data-set and event selection

The analysis has been done using the data of pp collisions at center-of-mass energy $\sqrt{s} = 13$ TeV collected during 2016, 2017, and 2018 (Run II). Data from each year production are merged together into a single full-statistic sample, in order to minimize the statistical fluctuations. The events are selected with the minimum bias trigger called kINT7, which is given by the logical AND of the V0A and V0C detectors. For the multiplicity dependent analysis the "INEL> 0" class has been used. This is defined as the set of inelastic collisions with at least one charged particle in the pseudo-rapidity range $|\eta| < 1$ [67]. The event sample belonging to INEL> 0 refers to the total charge deposited in both V0 detectors, and can be divided into several multiplicity classes (called V0M classes) [39]. The average charged-particle multiplicity densities corresponding to the different multiplicity classes are indicated in Tab. 6.1. The first class is related to high multiplicity events, while the last one refers to low multiplicity ones.

The total number of events selected for this analysis is $\sim 1.3 \times 10^9$. In Fig. 6.1 is reported the number of accepted events as a function of multiplicity, that exhibits a flat behaviour. Events were also selected with z-vertex within ± 10 cm from the nominal interaction point. In addition, the following event-selection cuts were used, many of them are considered as standard within the ALICE experiment for the resonances analysis.

- Standard Physics Selection: the AliRoot framework provides a class (called AliPhysicsSelection) that automatically selects the requested

Table 6.1: Average charged-particle multiplicity densities for each multiplicity class.

Multiplicity (%)	V0M Class	$\langle \mathrm{d}N_{\mathrm{ch}}/\mathrm{d}\eta \rangle_{\lvert\eta\rvert < 0.5}$
0-100	INEL>0	6.94 ± 0.10
0-1	I	26.02 ± 0.35
1-5	II	20.02 ± 0.27
5-10	III	16.17 ± 0.22
10-15	IV	13.77 ± 0.19
15-20	V	12.04 ± 0.17
20-30	VI	10.02 ± 0.14
30-40	VII	7.95 ± 0.11
40-50	VIII	6.32 ± 0.09
50 -70	IX	4.50 ± 0.07
70-100	X	2.55 ± 0.04

events just before the starting of the real physical analysis, avoiding the inclusion of non physical data taking runs (i.e. calibration runs) or events without the interaction trigger, i.e. trigger on bunch crossings, or events flagged as beam-gas by either V0A or V0C detectors

- The AliESDEvent::IsInCompleteDAQ check is used to reject events for which the event building does not work
- Pile-up events have been rejected using AliAnalysisUtils::IsPileUpEvent()
- Correlation between SPD clusters[1] and tracklets (pairs of SPD points) checked using AliAnalysisUtils::IsSPDClusterVsTrackletBG() with default parameters
- By default the track vertex is chosen. If it is missing, the vertex from the SPD is selected or at least event needs to have a track. Only events with vertex-z position $|v_{\mathrm{z}}| < 10$ cm have been taken into account
- SPD vertex-z resolution < 0.25 cm
- z-position difference between track and SPD vertex < 0.5 cm

[1] A cluster is a group of adjacent detector cells firing. It corresponds to a hit (energy deposition) produced by a crossing particle.

The SPD vertex is the interaction point identified with data from the only SPD detector. Primary vertex can be also determined from reconstructed TPC+ITS tracks or using only TPC information.

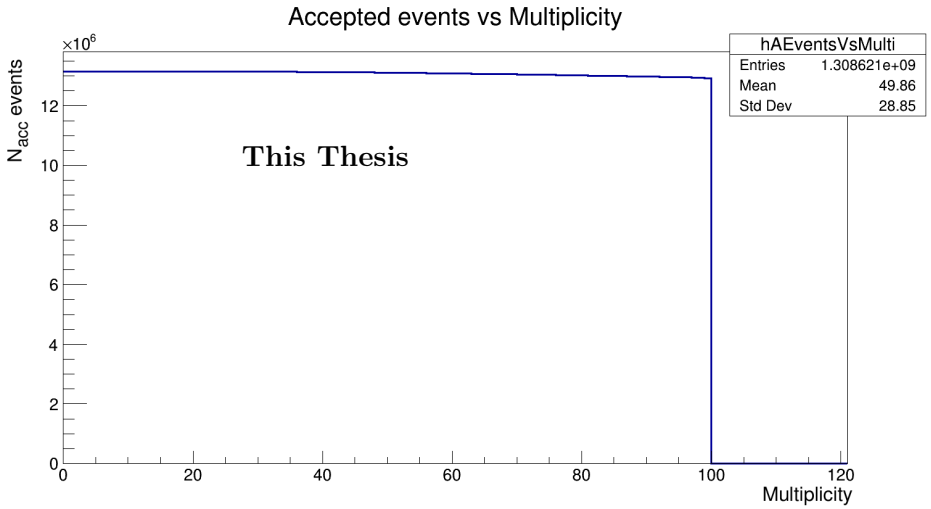

Figure 6.1: Number of accepted events after minimum bias selection as a function of multiplicity class intervals.

6.1 The $\pi^{\pm}$ and K^0_S selection

The Distance of Closest Approach (DCA) to the primary vertex is used to discriminate between primary and secondary particles. Primary particles are those produced directly in the interaction and all decay products from particles with a proper decay length $c\tau < 1$ cm. Secondary particles are all other particles observed in the experiment e.g., particles produced through interactions with the detector material and coming from weak decays.

6.1.1 Primary pion selection

For the primary pion selection, tracks have been accepted only in the range $|\eta| < 0.8$ (i.e. well within the TPC acceptance) and with $p_{\mathrm{T}} > 0.15$ GeV/c to improve the global resolution. Tracks were required to have at least 70 reconstructed clusters in the TPC. The ALICE TPC provides up to 159 space points (clusters) corresponding to the number of pad rows. This ensured

high efficiency and good $\mathrm{d}E/\mathrm{d}x$ resolution, limiting the contamination from secondary and fake tracks. In order to reduce secondary particles, tracks were required to have at least one hit in the SPD layers of the ITS detector and to have a DCA to the primary vertex less than 2 cm along the beam direction. The DCA in the transverse plane was required to be smaller than $7\sigma_{\mathrm{DCA}}(p_{\mathrm{T}})$ of the impact parameter resolution. Other additional criteria for quality control are the following:

- Ratio of number of crossed rows to number of findable clusters in TPC > 0.8. Due to limited efficiency, not all pad rows the track crosses gives a signal, the number of pad rows the track passes will be higher than the number of clusters. A pad row that does not give a signal is added to the number of clusters to obtain the number of crossed rows if the pad rows on both neighbouring sides do give a signal. A findable cluster is a pad row which based on the geometry of the track is a possible cluster.
- Require TPC refit
- Require ITS refit
- TPC χ^2 track fit per clusters < 4.0
- ITS χ^2 track fit per clusters < 36.0
- χ^2 per clusters in TPC-Constrained global fit < 36.0: χ^2 difference between TPC only track parameters extrapolated to the primary vertex and global track parameters. It removes fake high p_{T} tracks due to wrong association of ITS clusters

In addition the primary pions were identified through their energy loss $\mathrm{d}E/\mathrm{d}x$ in the TPC (see section 4.2.4). A 3σ p-dependent PID selection cut has been applied ($|\mathrm{N}\sigma_{\mathrm{TPC}}| < 3$).

6.1.2 V^0 and secondary tracks selection

The $\mathrm{K}^0_{\mathrm{S}}$ decays into an oppositely charged pion pair: ${K^0}_{\mathrm{S}} \to \pi^+ + \pi^-$. It is reconstructed by applying topological cuts on the tracks of the decay products (secondary pions). The following selection criteria were applied to select the secondary tracks.

Secondary tracks selection criteria

- Tracks were selected only in the range $-0.8 < \eta < 0.8$ to improve the resolution
- Require TPC refit
- Reject Kink[2] Daughters
- Number of rows crossed in TPC > 70
- Ratio of number of crossed rows to number of findable clusters in TPC > 0.8
- TPC χ^2 per clusters < 4.0
- A strict cut on the impact parameter of tracks to the primary vertex $>$ 0.06 cm was applied to make sure the track does not originate from the primary vertex

Furthermore secondary pions were identified through their energy loss $\mathrm{d}E/\mathrm{d}x$ in the TPC by a wide PID cut $|\mathrm{N}\sigma_{\mathrm{TPC}}| < 5$.

Only V^0 reconstructed in an offline procedure were selected for the analysis. The V^0 reconstructed by the identified secondary tracks have to fulfill the following topological cuts:

V^0 selection criteria

- V^0 candidates should decay at a radial distance from the interaction point larger than 0.5 cm.
- The V^0 cosine of pointing angle[3] was required to be greater than 0.97, to be sure that the V^0 particle arrives from the primary vertex.
- Distance of closest approach of the V^0 from the primary vertex was fixed to be less than < 0.3 cm

[2]A kink is a topological signature of charged particles decaying into 1 charged + 1 neutral particles.

[3]The pointing angle is the angle between $\vec{p}$ and a vector connecting the primary vertex and the V^0 position.

- Distance of closest approach between the two daughter tracks of V^0 was fixed to be less than 1.0 σ

In addition the following conditions were required to consider the selected V^0 as K^0_S candidates.

- Rapidity $|y| < 0.8$
- V^0 Mass Tolerance < 0.03 GeV/c^2: tolerance in the difference between computed and expected mass
- Proper Lifetime $(mL/p) < 20$ cm. This is a very loose cut since $c\tau_{K^0_S} = 2.7$ cm [66]
- Competing V^0 rejection ($|M_{\pi p} - M_\Lambda| < 4.3$ MeV/c^2): the competing V^0 rejection cut is used to select only pairs that have an invariant mass incompatible with the hypothesis to be originated from a Λ or $\overline{\Lambda}$ decay ($|M_\Lambda - 1115.683| > 4.3$ MeV/c^2 or $|M_{\overline{\Lambda}} - 1115.683| > 4.3$ MeV/c^2).

Chapter 7

Data analysis

The raw yield of $K^{*\pm}$ for the I V0M class has been estimated in the following 12 p_T bins (GeV/c): 0, 0.6, 1.2, 1.8, 2.4, 3.0, 3.6, 4.2, 4.8, 5.4, 6.0, 7.0, 10.0. For all the other multiplicity classes the following 14 p_T bins (GeV/c) have been considered: 0, 0.4, 0.8, 1.2, 1.6, 2.0, 2.5, 3.0, 3.5, 4.0, 4.5, 5.0, 6.0, 7.0, 10.0. The binning used for all the V0M classes is the same of the one considered in the K^{*0} multiplicity dependent analysis performed for the same collision system and energy [41]. To extract the signal of $K^{*\pm}$ mesons in each p_T bin, the following procedure was used for each multiplicity interval. First the invariant mass distribution of ${K^0}_S\pi^\pm$ pairs belonging to the same event was computed. The distribution obtained is a signal peak over a large combinatorial background. The background shape was estimated via the event-mixing technique, evaluating the invariant mass distribution of pairs taken from different events. The possibility for event mixing is provided in AliRoot thanks to the fact that the ESDs are stored in trees and one can chain and access simultaneously many ESD objects. The events are ordered according to the desired criterion of "similarity" assigning a specific index that can be used to access the similar events in the embedded analysis loops. In particular to assure a similar event structure and to avoid mismatch due to different acceptance, each ${K^0}_S\pi^\pm$ pair was selected with some similarity criteria on vertex position ($\Delta z < 1$ cm) and track multiplicity ($\Delta n < 5$). Then, in order to reduce statistical uncertainties, each event was mixed with other 10 events. The mixed-event distribution was finally normalized to the same event distribution in the invariant mass region of $1.1 < M < 1.2$ GeV/c^2.
The signal is obtained by subtracting the normalized mixed-event combinatorial background from the same event invariant mass distribution. An ex-

ample of the spectra obtained before and after the combinatorial background subtraction is shown in Fig. 7.1.

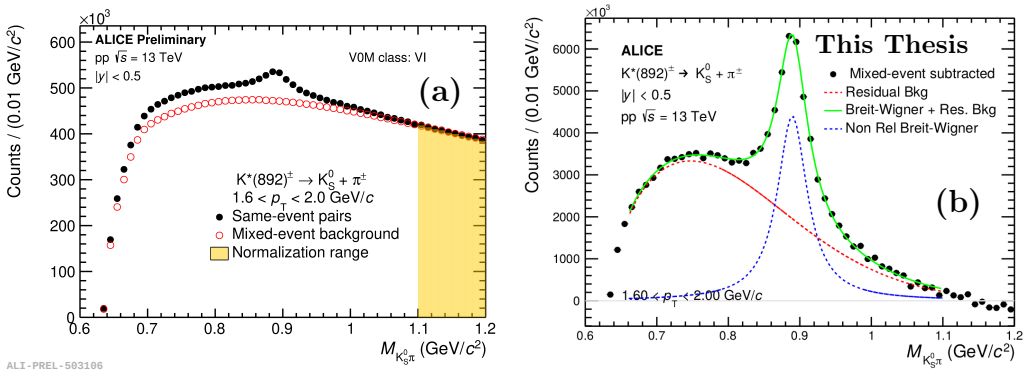

Figure 7.1: The $K^0_S\pi^{\pm}$ invariant mass distribution for the $1.6 < p_T < 2.0$ GeV/c bin in the VI V0M class (black full circles), before **(a)** and after **(b)** the uncorrelated background subtraction. **Left panel:** the red open circles describe the background shape evaluated via the event-mixing technique, while the yellow-filled area is the normalization region. **Right panel:** the solid green curve is the result of the final fit, the dashed red line represents the residual background, while the dashed blue line is the non-relativistic Breit-Wigner function.

7.1 Yield extraction and raw p_T spectra

The invariant mass distribution obtained after the combinatorial background subtraction was fitted with a non-relativistic Breit-Wigner function (f_{NRBW}) to identify the resonance peak and a proper function for the residual correlated background:

$$\frac{D}{2\pi}\frac{\Gamma_0}{(M_{K\pi}-M_0)^2+\frac{\Gamma_0^2}{4}}+F_{BG}(M_{K\pi}) \tag{7.1}$$

D is the integral of the peak function from 0 to ∞, while M_0 and Γ_0 are the mass and the width of $K^{*\pm}$. To have a good fit the width was fixed to the PDG value [66].
As for the inclusive analysis on $K^{*\pm}$ production in inelastic pp collisions [65],

the residual background shape for the different p_{T} bins was parameterized with the following function:

$$F_{BG}(M_{K\pi}) = [M_{K\pi} - (m_\pi + m_K)]^n \, e^{(A+BM_{K\pi}+CM_{K\pi}^2)} \tag{7.2}$$

where $m_\pi = 139.57$ MeV/c^2 [66] and $m_K = 497.61$ MeV/c^2 [66] are the pion and $\mathrm{K}^0_{\mathrm{S}}$ masses, while n, A, B and C are fit parameters.
The fitting range used was 0.66 - 1.10 GeV/c^2 for every p_{T} bin of each multiplicity class.
The raw yield of $\mathrm{K}^{*\pm}$ was calculated using two different methods: the function integration ($\mathrm{Y_{FI}}$) and the bin counting ($\mathrm{Y_{BC}}$), where the second was used as default and the first was used for systematic study.

Function Integration ($\mathbf{Y_{FI}}$):

The parameter D of the fit is the integral of the peak function from 0 to ∞, but the mass region $0 < M_{K\pi} < (m_\pi + m_K)$ is kinematically forbidden. Therefore:

$$Y_{FI} = D - \int_0^{m_\pi+m_K} f_{NRBW}(m_{inv})\, dm_{inv} \tag{7.3}$$

The integral in the kinematically forbidden region is about 2.5% of the total integral, with the exact ratio depending on the peak parameters.

Bin Counting ($\mathbf{Y_{BC}}$):

The raw yield ($\mathrm{N_{raw}}$) was extracted by integrating the invariant mass histogram ($\mathrm{N_{counts}}$) over the region $\mathrm{I_{min}} < M_{K\pi} < \mathrm{I_{max}}$ (where $\mathrm{I_{min}} = M_0 - 2\Gamma_0$, and $\mathrm{I_{max}} = M_0 + 2\Gamma_0$), subtracting the integral of the residual background portion estimated over that same interval ($\mathrm{N_{RB}}$), and adding the integral of the tails of the non-relativistic Breit-Wigner fit on both ends ($\mathrm{N_{tails}}$). In particular:

$$N_{raw} = N_{counts} - N_{RB} + N_{tails} \tag{7.4}$$

where:

$$N_{tails} = N_{low} + N_{high} = \int_{m_\pi+m_K}^{M_0-2\Gamma_0} f_{NRBW}(m_{inv})\, dm_{inv} + \int_{M_0+2\Gamma_0}^{\infty} f_{NRBW}(m_{inv})\, dm_{inv} \tag{7.5}$$

The error on N_{RB} was calculated by using the root function **IntegralError()**: fBgOnly → IntegralError(I_{min}, I_{max}, Par[4], a), where a is the covariance matrix, fBgOnly is the residual background function and Par[4] is a vector containing the values of the parameters of the residual background function. The same function was used to compute the error on N_{low} and N_{high} too. The statistical uncertainties of the yields in the tail regions are assumed to be fully correlated with each other and with the statistical uncertainty of the yield calculated from the histogram.
In Fig. 7.2 an example of the $K^0_S\,\pi^{\pm}$ invariant mass distribution fits after the uncorrelated background subtraction is shown with the highlighted integral regions to better visualize the bin counting technique.

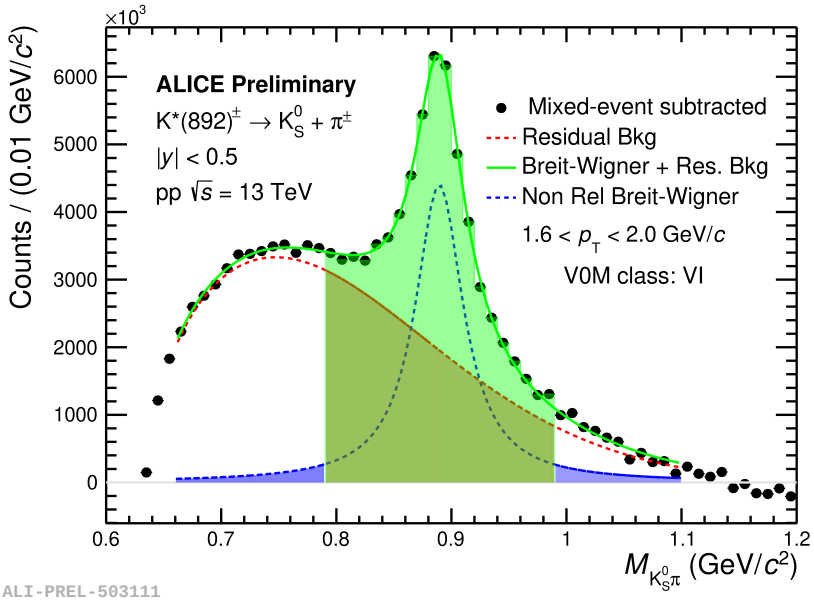

Figure 7.2: The $K^0_S\pi^{\pm}$ invariant mass distribution fits for the $1.6 < p_T < 2.0$ GeV/c bin in the VI V0M class. Colored regions show the areas interested in the bin counting method: the green one represents the integral of the invariant mass histogram over the region $I_{min} < M_{K\pi} < I_{max}$ (N_{counts}); the brown coloured area is the integral of the residual background portion estimated over that same interval (N_{RB}); the blue coloured areas are the integrals of the Non-Relativistic Breit-Wigner function in the tail regions (N_{low} and N_{high}).

In Fig. 7.3 the raw yield p_T distributions obtained with the two methods

(function integration and bin counting) are compared for the INEL> 0 class.

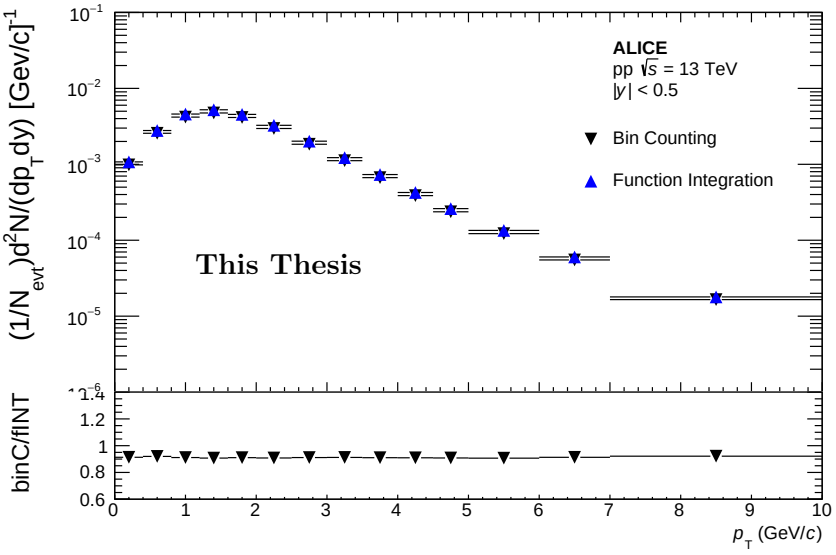

Figure 7.3: The p_{T} yield distributions estimated with the bin counting method (black inverted triangles) and with function integration (blue triangles). The ratio of the two distributions (bin counting/function integration) is shown in the lower panel.

7.2 The K*± Mass and Width determination

In Fig. 7.4 the mass and the width values obtained in the INEL> 0 class in the different p_{T} intervals fitting the invariant mass distribution by eq. 7.1 are shown. In this case the parameter associated to the width was set as free, while in the whole analysis it has been fixed to the PDG value [66] (except for the systematic study). However, as shown in Fig. 7.4.b, also in the case of a free parameter, the values of the width are equal, within the statistical uncertainties, to the PDG value ($\Gamma_0 \sim 51$ MeV/c^2) [66]. Considering Fig. 7.4.a a lower mass value is observed for $p_{\mathrm{T}} < 3$ GeV/c while an almost constant value of about 893 MeV/c^2 has been obtained for $p_{\mathrm{T}} > 3$ GeV/c, slightly higher than the PDG reference ($\mathrm{M}_0 \sim 892$ MeV/c^2) [66]. The same trend at

low p_{T} has been observed also for the K^{*0} mass determination in Pb–Pb at $\sqrt{s_{\mathrm{NN}}} = 2.76$ TeV [42] and pp at $\sqrt{s} = 7$ TeV [15] collisions, as well as in Au–Au collisions at $\sqrt{s_{\mathrm{NN}}} = 200$ GeV at RHIC with the STAR detector [68] (see Fig. 7.5). In these cases the deviation from the vacuum value observed at low p_{T} was not attributed to an effect of the medium but to detector and kinematic cuts effects [68, 69].

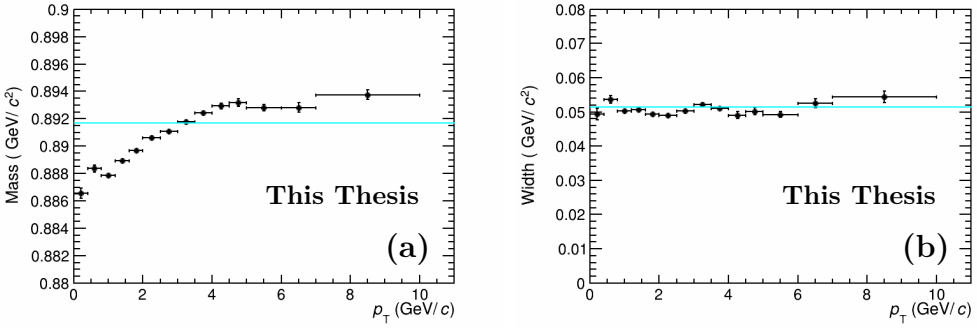

Figure 7.4: Mass **(a)** and width **(b)** of the $\mathrm{K}^{*\pm}$ as a function of p_{T} obtained in the INEL$>$ 0 class fitting the $\mathrm{K}^0_{\mathrm{S}}\pi^{\pm}$ invariant mass distribution with a non-relativistic Breit-Wigner and the residual background function (eq. 7.1). The PDG reference values are also shown as cyan lines.

Resonances that decay when chiral symmetry is (partially) restored, as it should happen near the QGP-HG phase transition (see section 1.1), may exhibit mass shifts or width broadening with respect to the vacuum values [70, 71]. Therefore, in general, any difference between the measured masses and widths in Pb–Pb collisions with respect to those in pp collisions could be interpreted as a possible signature of chiral symmetry restoration. However since also high multiplicity pp collisions have shown patterns that are reminiscent of phenomena observed in A–A collisions, it could be interesting to investigate mass and width evolution from low to high multiplicity classes.
Figure 7.6 shows the values of the width obtained as a function of p_{T} in the various multiplicity classes. The distributions exhibit an almost flat behaviour as highlighted by the constant fit performed.
Figure 7.7 shows the $\mathrm{K}^{*\pm}$ mass computed in the low (blue) and high (red) multiplicity intervals as a function of p_{T} (Fig. 7.7.a), and the width results obtained as a weighted mean of width values from each multiplicity class as

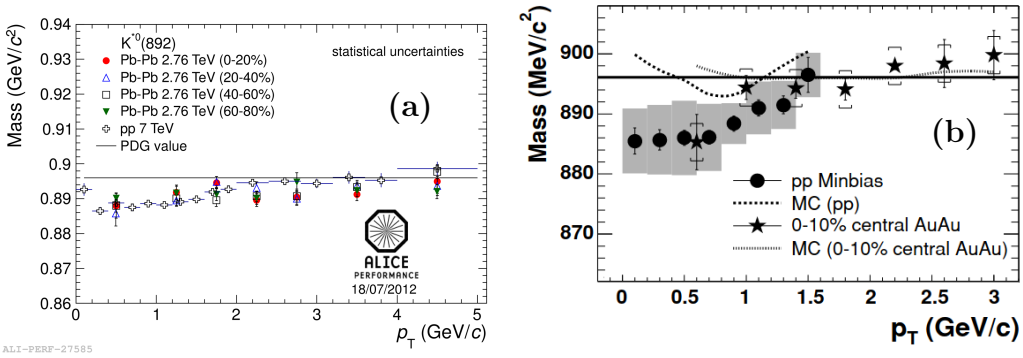

Figure 7.5: **Left panel:**(ALICE) mass of K^{*0} as a function of p_T in Pb–Pb collisions at $\sqrt{s_{NN}} = 2.76$ TeV [42] for different centrality classes. Results for pp collisions at $\sqrt{s} = 7$ TeV [15] are also shown. **Right panel:** (STAR) the K^{*0} mass as a function of p_T for minimum bias pp interactions and for central Au–Au collisions [68].

a function of the charged-particle multiplicity (Fig. 7.7.b). The results of the weighted mean computation of the width are listed in Tab. 7.1.

No multiplicity dependence of width is observed within the statistical uncertainties. A slight shift of the mass values (considering only statistical uncertainties) is measured at low p_T. No conclusion can be extracted before the estimation of the systematic uncertainties. However the K^{*0} analysis in Pb–Pb collisions at $\sqrt{s_{NN}} = 2.76$ TeV [42], where a major effect should be expected, showed no mass shift nor width broadening as a function of centrality [72]. In this case the lack of the expected signatures of chiral symmetry restoration has been attributed to the loss of resonances produced early in the collision, due to re-scattering and the regeneration of additional resonances late produced in the collision [73].

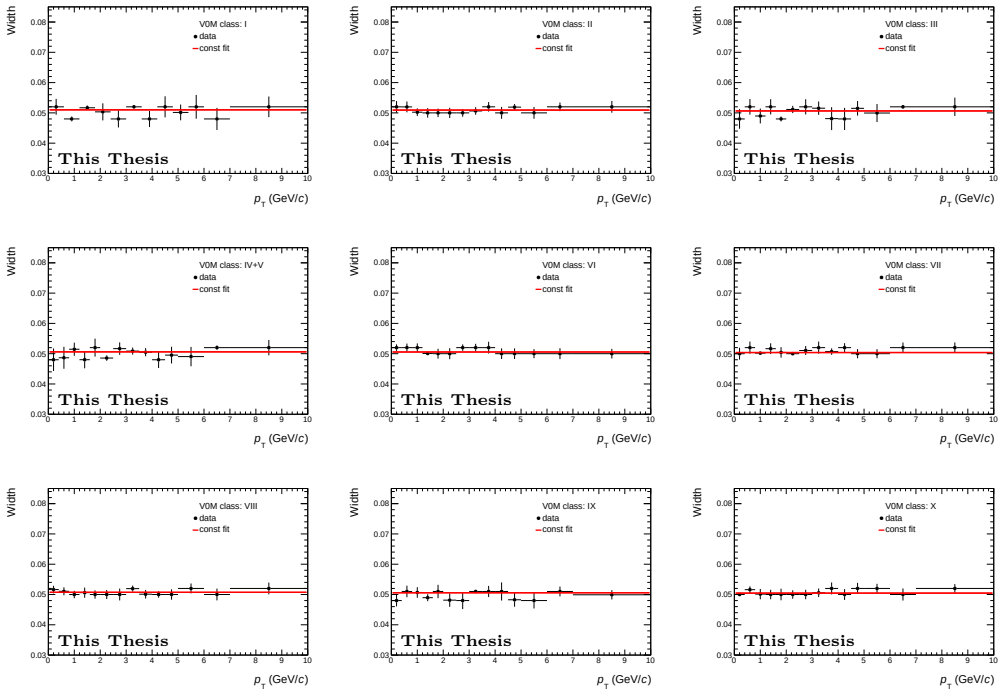

Figure 7.6: The p_{T} distributions of the $\mathrm{K}^{*\pm}$ width for the different multiplicity classes. Red lines are the constant fits.

Table 7.1: Values of the $\mathrm{K}^{*\pm}$ width obtained from each V0M class, listed in increasing event multiplicity. Results are in agreement within the uncertainties with the PDG value: $\Gamma_0 = (0.0514 \pm 0.0008)$ GeV/c^2 [66].

V0M Class	Width ± stat. err. (GeV/c^2)
X	0.050451 ± 0.000314
IX	0.050575 ± 0.000296
VIII	0.050714 ± 0.000374
VII	0.050380 ± 0.000248
VI	0.050558 ± 0.000264
IV+V	0.050610 ± 0.000409
III	0.050645 ± 0.000392
II	0.050922 ± 0.000394
I	0.051006 ± 0.000339

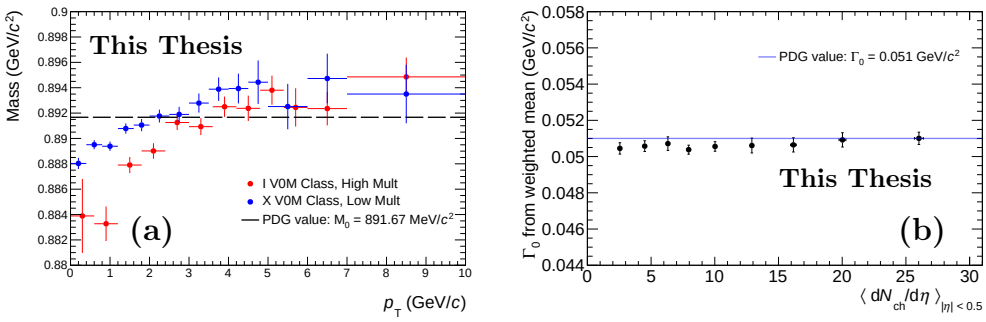

Figure 7.7: **Left panel:** Mass of the K*± as a function of p_{T} for low (blue) and high (red) multiplicity intervals. The dashed black line is the PDG value [66]. A slight mass shift (considering only statistical uncertainties) is measured at low p_{T}. No conclusion can be extracted before the estimation of the systematic uncertainties. **Right panel:** Width of the K*± as a function of the charged-particle multiplicity density. The blue line is the PDG value [66]. No width broadening is observed across the different event multiplicities.

Chapter 8

Monte Carlo correction estimates

A simulated data set was analyzed in order to evaluate the $K^{*\pm}$ reconstruction acceptance×efficiency of the detector and systematic studies. Particle production is simulated using the event generator (PYTHIA8) while particle interactions with the ALICE detector are simulated using GEANT3 [74]. The same event selection, track quality cuts, and topological cuts were used for the real and simulated data. The $K^{*\pm}$ produced by the event generator which decay to $\pi^{\pm}$ and $K^0{}_S$ are referred to as the "generated" particles. These particles are the input for the GEANT3 detector simulation. The tracks and the V^0 which are identified by the reconstruction algorithms and which pass track and topological selection and PID cuts are referred to as the "reconstructed" tracks and V^0. A reconstructed $K^{*\pm}$ meson is a $K^{*\pm}$ for which both daughters ($\pi^{\pm}$ and $K^0{}_S$) have been reconstructed.

8.1 Acceptance×Efficiency

The reconstruction acceptance×efficiency (ϵ_{rec}) was calculated using the simulation set mentioned above. In each p_T bin and for each multiplicity class, ϵ_{rec} is given by:

$$\epsilon_{rec} = \frac{N_{reconstructed}(K^{*\pm} \to \pi^{\pm} + K^0{}_S)}{N_{generated}(K^{*\pm} \to \pi^{\pm} + K^0{}_S)} \tag{8.1}$$

where $N_{generated}$ and $N_{reconstructed}$ are respectively the number of generated and reconstructed $K^{*\pm}$ mesons with $|y| < 0.5$ that decay into a $K^0{}_S$ and a charged pion ($\pi^{\pm}$). Since the events of numerator and denominator

are correlated, the uncertainty on ϵ_{rec} was calculated following the Bayesian approach. Considering an efficiency defined as $\epsilon = k/n$, where the numerator k is a subset of the denominator n, the standard deviation is:

$$\sigma = \sqrt{\frac{k+1}{n+2}\left(\frac{k+2}{n+3} - \frac{k+1}{n+2}\right)} \tag{8.2}$$

The ϵ_{rec} distributions as a function of p_{T} for each multiplicity class are shown in Fig. 8.1.

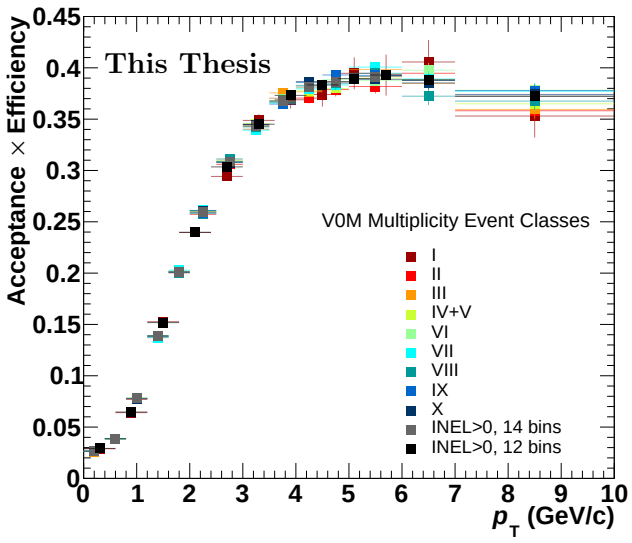

Figure 8.1: Acceptance×efficiency distributions as a function of p_{T} for each multiplicity class obtained with the merged LHC16, LHC17, and LHC18 periods simulated production.

The distributions show a strong dependence on transverse momentum at low p_{T}, while no significant multiplicity dependence is observed. This can be seen more clearly from the ratios of the acceptance×efficiency of each single multiplicity interval over the inclusive acceptance×efficiency (i.e. the one relative to the INEL$>$ 0 V0M class, which includes the entire data set with respect to multiplicity) and fitting them with constants. As shown

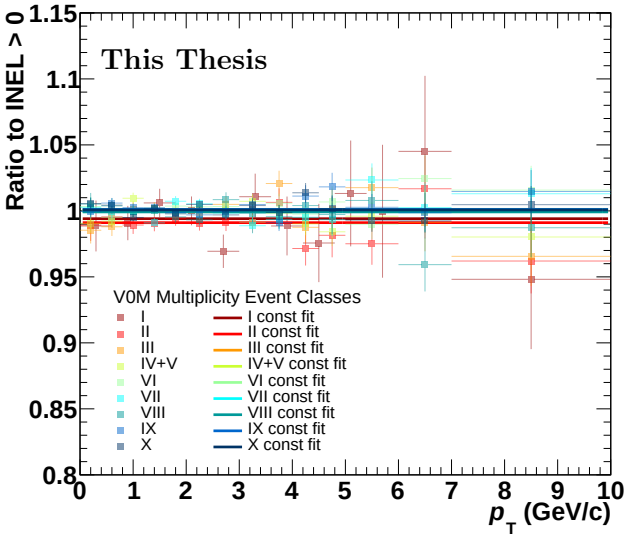

Figure 8.2: Ratios of the ϵ_{rec} of each multiplicity class over the inclusive one. The result of the fits with constants are also shown.

in Fig. 8.2 and in Table 8.1 the fitting procedure gives for all the ratios values close to 1, assuring no multiplicity dependence. Therefore the inclusive acceptance×efficiency has been used as correction factor for all multiplicity classes.

8.2 Signal-Loss correction

The signal-loss correction factor (f_{SL}) accounts for the loss of $K^{*\pm}$ mesons incurred by selecting events that satisfy the kINT7 trigger, rather than all inelastic events. This correction is the ratio of the p_T spectrum in inelastic events to the p_T spectrum in kINT7 events. The p_T spectrum in inelastic events were generated without any trigger selection and with a check that the generated vertex is inside $\pm$ 10 cm (SetCheckGeneratedVertexZ option was used). The obtained p_T distributions of the signal-loss corrections for each multiplicity class studied are reported in Fig. 8.3. They are slightly different especially at low p_T, in particular the X V0M class exhibits the

Table 8.1: Values of constant parameter fit of each multiplicity class ϵ_{rec} ratios over the inclusive one.

Class	const. par.	par. error
I	0.994082	0.00500064
II	0.991076	0.00223149
III	0.999596	0.00198073
IV+V	1.00024	0.00140435
VI	1.0012	0.00145292
VII	0.999484	0.00151211
VIII	0.999214	0.00176267
IX	1.00109	0.00121265
X	1.00071	0.00103318

largest values. This correction is a p_{T}-dependent factor which is peaked at low p_{T}, indicating that events which fail the kINT7 selection have softer $\mathrm{K}^{*\pm}$ p_{T} spectra than the average inelastic events.

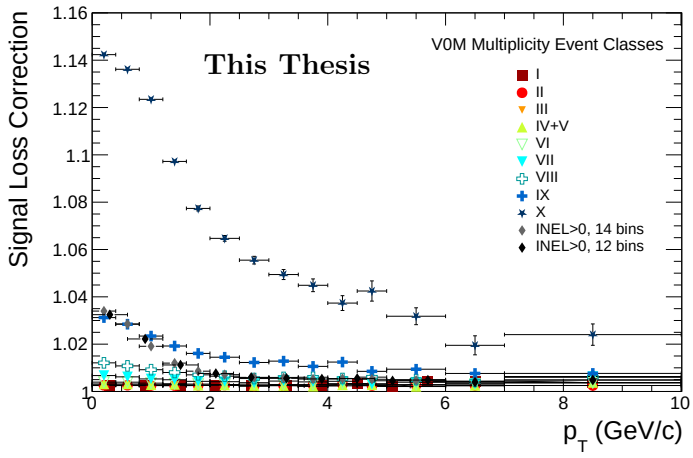

Figure 8.3: Signal-loss correction factors ($\mathrm{f_{SL}}$) as a function of p_{T} for each multiplicity class.

Chapter 9

Systematic uncertainties

For the $K^{*\pm}$ p_T spectra the following sources of systematic uncertainty were considered:

- global tracking uncertainty;
- material budget;
- hadronic interaction;
- primary track selection, PID cut for primary pions;
- secondary track selection, PID and topological cuts for K^0_S;
- primary vertex selection;
- signal extraction;

9.1 Global tracking uncertainty

The global tracking uncertainty in ITS-TPC matching for tracks in the runs used for this analysis was estimated using data listed in the tables from Ref. [75]. In particular since different LHC periods were considered, the uncertainty on each p_T bin was computed as a weighted mean of the corresponding values reported in the tables for all the runs analyzed, using as weight the number of events of each child considered.

9.2 Material budget

The systematic uncertainty, due to the not perfect description of the ALICE detector material budget in the software replica of the detector constructed by GEANT3, was computed for the $\mathrm{K}^{*\pm}$ using the material budget uncertainty p_{T} distributions of the decay daughters ($\pi^{\pm}$ and $\mathrm{K}^0_{\mathrm{S}}$) estimated in other ALICE analyses. In particular the $\pi^{\pm}$ uncertainty was inherited from the analysis of identified charged hadrons for p–Pb (2013 data) [76], used also for other resonances analyses, while the uncertainty connected to $\mathrm{K}^0_{\mathrm{S}}$ was derived from the strange particle analysis in pp collisions at $\sqrt{s} = 13$ TeV [38].

The $\mathrm{K}^{*\pm}$ uncertainty was obtained from the daughter uncertainties, weighting them by their p_{T} distributions. The p_{T} distributions of $\pi^{\pm}$ and $\mathrm{K}^0_{\mathrm{S}}$ as a function of $\mathrm{K}^{*\pm}$ transverse momentum was found using the same Monte Carlo simulation production exploited for the acceptance×efficiency calculation. These distributions are used to estimate the weighted average of the material budget uncertainty for each $\mathrm{K}^{*\pm}$ p_{T} bin. Let consider:

- $w(p_{\mathrm{T}\,K^{*\pm}})$ as the ratio between the measured and generated $\mathrm{K}^{*\pm}$ p_{T} spectra;
- $up(p_{\mathrm{T}})$ and $uk(p_{\mathrm{T}})$ as the pion and $\mathrm{K}^0_{\mathrm{S}}$ material budget uncertainty, respectively;
- $p_{\mathrm{T}\pi}$ and $p_{\mathrm{T}\mathrm{K}^0_{\mathrm{S}}}$ as the transverse momenta of the $\pi^{\pm}$ and $\mathrm{K}^0_{\mathrm{S}}$ decay daughters of each simulated $\mathrm{K}^{*\pm}$;
- $N(p_{\mathrm{T}\mathrm{K}^{*\pm}}, p_{\mathrm{T}\pi}, p_{\mathrm{T}\mathrm{K}^0_{\mathrm{S}}})$ as the number of $\mathrm{K}^{*\pm}$ with a given $p_{\mathrm{T}\mathrm{K}^{*\pm}}$ that decay into a $\pi^{\pm}$ and $\mathrm{K}^0_{\mathrm{S}}$ with transverse momentum equal to $p_{\mathrm{T}\pi}$ and $p_{\mathrm{T}\mathrm{K}^0_{\mathrm{S}}}$, respectively.

For each p_{T} bin, the two-particle uncertainty $u(p_{\mathrm{T}})$ is given, for all the generated $\mathrm{K}^{*\pm}$ mesons, by:

$$u(p_{\mathrm{T}}) = \frac{\sum N(p_{\mathrm{T}\mathrm{K}^{*\pm}}, p_{\mathrm{T}\pi}, p_{\mathrm{T}\mathrm{K}^0_{\mathrm{S}}}) w(p_{\mathrm{T}\mathrm{K}^{*\pm}}) [up(p_{\mathrm{T}}) + uk(p_{\mathrm{T}})]}{\sum N(p_{\mathrm{T}\mathrm{K}^{*\pm}}, p_{\mathrm{T}\pi}, p_{\mathrm{T}\mathrm{K}^0_{\mathrm{S}}}) w(p_{\mathrm{T}\mathrm{K}^{*\pm}})} \tag{9.1}$$

The calculation assumes that the uncertainties of the two decay daughters are fully correlated. The obtained distribution is reported in Fig. 9.1.

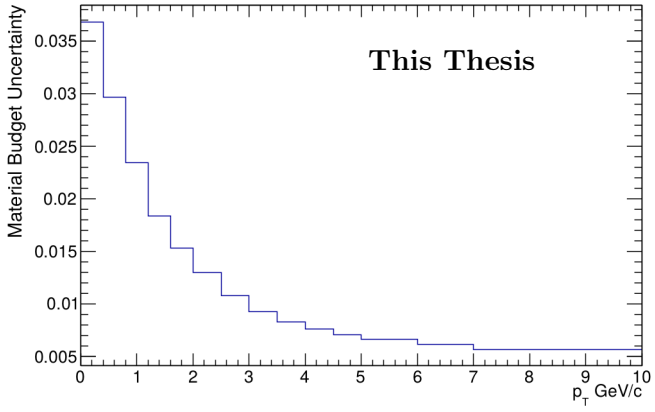

Figure 9.1: Material budget uncertainty p_{T} distribution for $\mathrm{K}^{*\pm}$.

9.3 Hadronic interaction

The same procedure used for the material budget uncertainty calculation was followed also for estimating the systematic uncertainty due to the hadronic interaction. The hadronic interaction uncertainty for pions was taken from the p–Pb (2013 data) analysis [76]. The hadronic interaction uncertainty for $\mathrm{K}^0_{\mathrm{S}}$ is negligible, therefore in this case $uk(p_{\mathrm{T}})$ in Eq. 9.1 is considered equal to 0. The obtained distribution is shown in Fig. 9.2

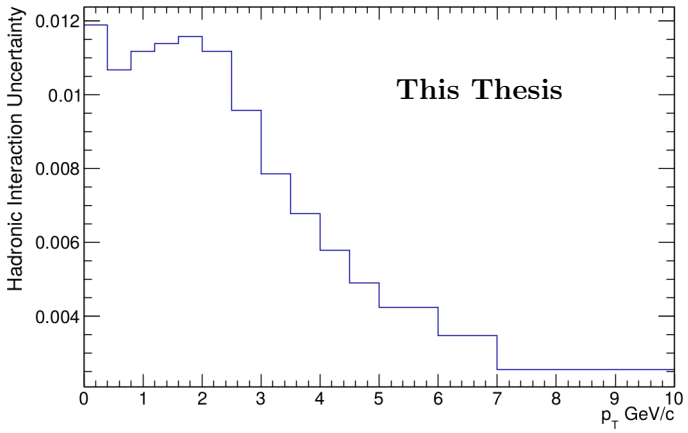

Figure 9.2: Hadronic interaction uncertainty p_{T} distribution for $\mathrm{K}^{*\pm}$.

9.4 Systematic uncertainties using grouping method

For each multiplicity class the systematic uncertainties due to the primary pion selection (group I), secondary tracks and K^0_S identification (group II), and primary vertex selection (group III) were evaluated with the grouping method. For each cut of a group, one or two variations from the standard selection criteria were considered, applying them one by one. In Tables 9.1, 9.2, and 9.3 are listed the different cuts considered, together with the standard cuts. In addition the parameters of the signal extraction procedure were varied too. For each cut (standard or variation) and for each p_{T} bin in a given multiplicity class, the signal was extracted 12 times (11 variations + 1 standard), by changing one parameter and keeping the others fixed. The standard and modified values used for the signal extraction parameters are listed in Tab. 9.4.

Table 9.1: Standard and modified cuts for primary pion selection.

Selection criteria	Standard	Variation 1	Variation 2
TPC crossed rows	> 70	> 100	> 80
Crossed rows/Findable clusters	> 0.8	> 0.9	-
TPC χ^2	< 4.0	< 2.3	-
ITS χ^2	< 36	< 25	< 4
Global χ^2	36	25	-
No. SPD clusters	> 1	> 0	-
$\mathrm{DCA_z}$ (cm)	< 2	< 1	< 0.2
$\mathrm{DCA_r}$ (σ)	< 7	< 4	-
TPC PID Primary π (σ)	< 3	< 3.5	< 2.5

Therefore for each cut (35 in total: 34 variations + 1 standard) 12 different yield spectra have been estimated, i.e. for each p_{T} bin 12 fits were done, each with a given probability. The used procedure is described in the following and was performed for each multiplicity class:

- For each cut (index j) in a group the weighted mean (V_{meanj}) of the 12 different spectra was calculated using the probability of the fit as weight:

$$V_{meanj} = \frac{\sum_i V_i p_i}{\sum_i p_i} \tag{9.2}$$

where V_i and p_i are respectively the efficiency corrected yield and the corresponding fit probability from the 12 different settings for the signal extraction.

- A Barlow check (or consistency check) was done for all the 12 variations of signal extraction of a particular cut, compared to those of the standard cut. The cuts which passed the Barlow check are not considered in the final systematic uncertainties.

- The systematic uncertainty for each cut (U_{SXj}) is the RMS of $V_{meanj} - V_i$.

- The systematic uncertainty connected to the signal extraction procedure (U_{MSX}) is given by the weighted mean of the systematic uncertainties of all the cuts which fail the Barlow check:

$$U_{MSX} = \frac{\sum_j U_{SXj} p_{meanj}}{\sum_j p_{meanj}} \tag{9.3}$$

where $p_{meanj} = \langle p_i \rangle$.

- For each group the weighted mean of the mean yields V_{meanj} estimated with the standard selection criteria and with the cuts which fail the Barlow check was computed:

$$V_{MEAN} = \frac{\sum_j V_{meanj} p_{meanj}}{\sum_j p_{meanj}} \tag{9.4}$$

In Fig. 9.3, and 9.4 are shown as an example the V_{meanj} p_{T} spectra, together with the V_{MEAN} p_{T} distribution, of the used cuts for the primary pion, secondary tracks and $\mathrm{K}^0_{\mathrm{S}}$ selection, and primary vertex identification respectively.

- Then the systematic uncertainty for each group (U_{RSX}) is given by the RMS of $V_{MEAN} - V_{meanj}$.

Table 9.2: Standard and modified cuts for secondary tracks and K^0_S identification.

Selection criteria	Standard	Variation 1	Variation 2
TPC crossed rows	> 70	> 100	> 80
Crossed rows/Findable clusters	> 0.8	> 0.9	-
DCA tracks to PV (cm)	> 0.06	> 0.07	> 0.05
PID secondary π (σ)	< 5	< 4.5	< 4
V^0 decay radius (cm)	> 0.5	> 0.7	> 0.3
Cosine PA	> 0.97	> 0.99	> 0.95
DCA V^0 daughters (σ)	< 1	< 1.25	< 0.75
Lifetime (cm)	< 20	< 12	-
Competing V^0 rejection $\lvert M_{\pi p} - M_{\Lambda}\rvert$ (MeV/c^2)	< 4.3	< 5.4	< 3.2
V^0 mass tolerance $\lvert M_{K^0_S} - 497.611\rvert$ (MeV/c^2)	< 30	< 40	< 20
K^0_S rapidity	< 0.8	< 0.9	< 0.7

Table 9.3: Standard and modified cuts for primary vertex identification.

Selection criteria	Standard	Variation 1	Variation 2
Primary vertex (cm)	< 10	< 12	< 8

Table 9.4: Standard and modified parameters for signal extraction.

Signal extraction parameters	Standard	Variation 1	Variation 2	Variation 3
Fit function	Expol	Polynomial 2	Polynomial 3	-
Normalization range (GeV/c^2)	1.1-1.2	1.1-1.3	1.1-1.4	-
Fit range (GeV/c^2)	0.66-1.1	0.7-1.05	0.65-1.15	-
Bin counting range (GeV/c^2)	0.79-0.99	0.8-0.98	0.78-1.0	-
Width (GeV/c^2)	0.0508	0.0517	0.0499	freewidth

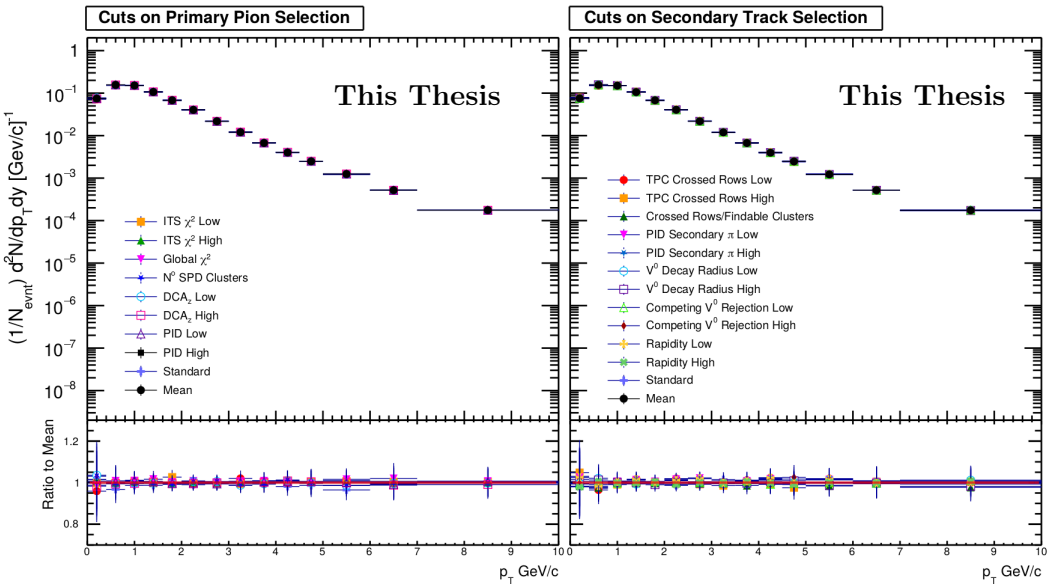

Figure 9.3: The V_{meanj} p_{T} spectra of the cuts used for systematic uncertainty estimation in the primary pion identification **(left panel)** and in the secondary tracks and $\mathrm{K}^0_{\mathrm{S}}$ selection **(right panel)** in the III V0M class. The V_{MEAN} p_{T} distribution is also reported. **Lower panels:** V_{meanj}/V_{MEAN} ratios as a function of p_{T} bins.

9.4.1 Barlow check

As described in [77], since the default and alternative measurements use (mostly) overlapping data sets, the agreement within the statistical uncertainties is not sufficient. Instead the agreement within the difference in quadrature of the statistical uncertainties is required. Indeed if two measurement are consistent within the difference in quadrature of their statistical uncertainties, it is not necessary taking into account the differences between them in the systematic uncertainties. For example, let consider two p_{T} spectra, one obtained with the default event selection criteria (y_{def}), the other obtained with an alternative setting (y_{al}). Their statistical uncertainties are σ_{def} and σ_{al}, respectively. The Barlow check histogram will be filled with Δ/σ_{cc}, where Δ is the yield deviation from the default measurements ($\Delta = y_{def} - y_{al}$) and σ_{cc} is the difference in quadrature between the statistical uncertainties ($\sigma_{cc} = \sqrt{|\sigma^2_{def} - \sigma^2_{al}|}$). This is done for all the 12 variations (index i) of signal

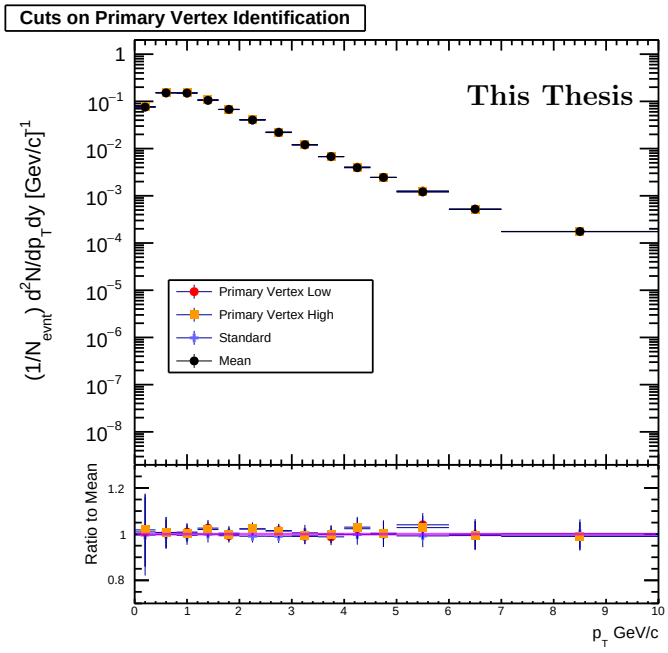

Figure 9.4: The V_{meanj} p_{T} spectra of the cuts used for systematic uncertainty estimation in the primary vertex identification in the III V0M class. The V_{MEAN} p_{T} distribution is also reported. Lower panel: V_{meanj}/V_{MEAN} ratio as a function of p_{T} bins.

extraction of each cut compared to the corresponding yield variations of the default cut. Therefore for the generic j^{th} cut the Barlow check histogram is filled with:

$$\frac{\Delta_j}{\sigma_{ccj}} = \frac{\sum_i (y_{def_i} - y_{al_i})}{\sum_i \sqrt{|\sigma_{def_i}{}^2 - \sigma_{al_i}^2|}} \qquad i = 1 - 12 \tag{9.5}$$

The selection criteria involving two variations were computed in the same Barlow check histogram. In this analysis a cut is not considered as a systematic source if at least 3 of the following 4 criteria of the Barlow check histogram are satisfied:

1. $|\Delta/\sigma_{cc}| \leq 0.2$;

2. standard deviation ≤ 1.3;

3. fraction of entries within $\pm 1 \geq 0.55$ ($I_1 \geq 0.55$);

4. fraction of entries within $\pm 2 \geq 0.75$ ($I_2 \geq 0.75$).

In Fig. 9.5 is shown an example of Barlow check histograms which passed (**a**) and failed (**b**) the consistency check.

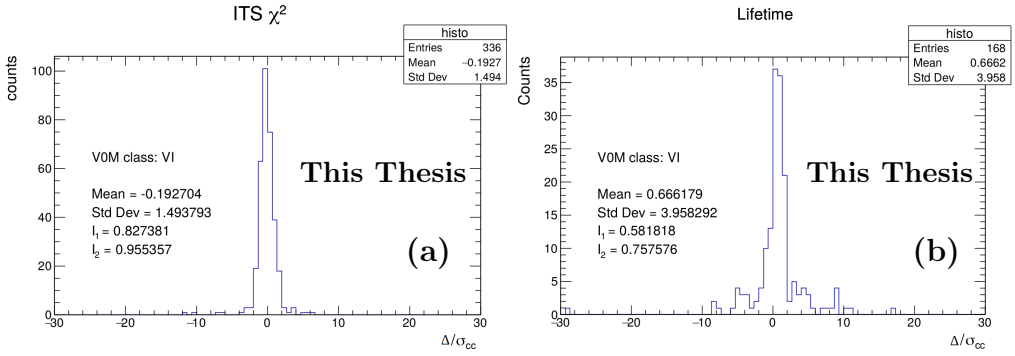

Figure 9.5: Barlow check histograms for ITS χ^2 (primary pion identification) (**a**) and lifetime (K^0_S selection) (**b**) cuts in the VI V0M multiplicity class. **Left panel:** the Barlow check histogram for the ITS χ^2 cut satisfies 3 of the 4 consistency criteria and therefore passed the check. Since for this cut two different variations were considered (see Tab. 9.1) the number of entries is 336 = 14 (the n° of p_T bins) × 12 (the total signal extraction configurations) × 2 (the n° of the cut variations). **Right panel:** the lifetime histogram failed the Barlow check (only 2/4 criteria satisfied). In this case, since only one variation was considered (see Tab. 9.2) the number of entries is 168.

9.5 Smoothing procedure for systematic uncertainties

Since the systematic uncertainty distributions as a function of p_T exhibit some fluctuations from bin to bin, each source of systematic uncertainty was smoothed individually (the total systematic uncertainty was not directly smoothed). The following smoothing procedure was applied. For the j^{th} p_T bin the uncertainty σ_j^{fin} was obtained averaging the initial uncertainty σ_j^{in} with $\sigma_{j\pm1}^{in}$:

$$\sigma_j^{fin} = \frac{\sigma_{j-1}^{in} + \sigma_j^{in} + \sigma_{j+1}^{in}}{3} \tag{9.6}$$

9.6 Total systematic uncertainty

The systematic uncertainties from the different sources were added in quadrature to obtain the total systematic uncertainty. An example of the p_{T} distributions of the systematic uncertainty from the different sources previously described is shown in Fig. 9.6. In the same figure the total systematic uncertainty p_{T} distribution is also shown.

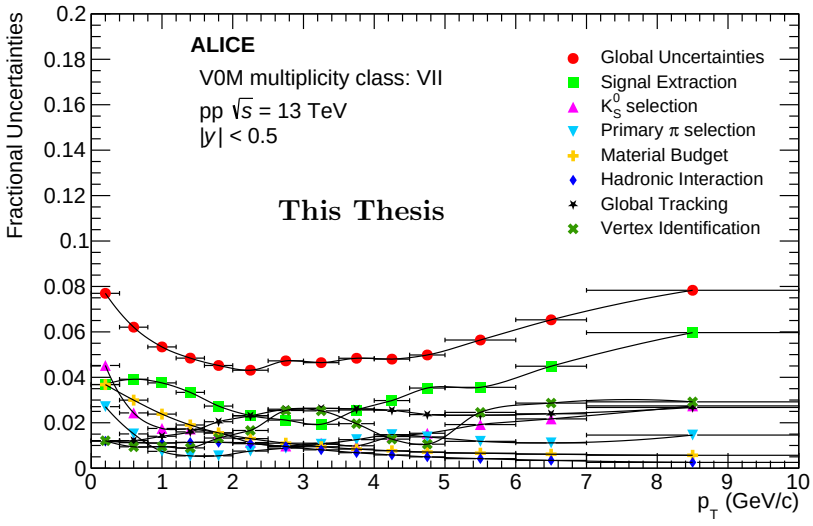

Figure 9.6: The p_{T} distributions of the systematic uncertainty from the different sources in the VII V0M class. The p_{T} distribution of the total systematic uncertainty obtained by adding in quadrature the several sources is also shown.

9.7 Systematic uncertainties uncorrelated with multiplicity

In order to compute the fraction of systematic uncertainty which is uncorrelated with multiplicity, the same procedure adopted in the multiplicity dependent analysis of (multi-)strange hadron production in pp collisions at $\sqrt{s} = 13$ TeV [78], as well as other analyses, was followed. The procedure starts from the computation of the R-factor defined as:

$$R = \frac{Y_{var}^{mult-i}}{Y_{def}^{mult-i}} \Bigg/ \frac{Y_{var}^{MB}}{Y_{def}^{MB}} \tag{9.7}$$

where Y^{mult-i} is the signal measured in the multiplicity class i while Y^{MB} is the signal measured in the 0-100% class. The subscripts def and var refer to the default and the alternate variations, respectively. The compatibility of R with unity means that the systematic uncertainty under study is "correlated" with multiplicity, i.e. it is not dependent on multiplicity. The computation of the R-factor is performed by using wider $p_{\rm T}$ bins and multiplicity ranges in order to reduce as much as possible the impact of statistical fluctuations. The new $p_{\rm T}$ binning (GeV/c) used is: 0.0, 0.8, 1.6, 2.5, 4.0, 6.0, 10.0 while the new multiplicity classes (%) considered are: 0-5, 5-20, 20-50, 50-100. The errors on R are computed following the Roger Barlow's prescription (σ_{RB}^{R}) [77]. Fig. 9.7 shows an example of the different R-factor distributions as a function of charged-particle multiplicity in several $p_{\rm T}$ slices computed for a variation on the primary pion, $\rm K^0_s$ and secondary tracks, and primary vertex selection criteria, and on the signal extraction parameters, respectively. Similar plots have been obtained for all the variations.

The fraction of uncorrelated systematic is obtained by adding in quadrature all the |R−1| factors (in each $p_{\rm T}$ bin and multiplicity class) that satisfy the condition $|{\rm R}-1| > \sigma_{RB}^{R}$. The uncorrelated uncertainties obtained in each multiplicity class are shown in Fig. 9.8. Since the uncorrelated uncertainties as a function of $p_{\rm T}$ change with multiplicity, the maximum value in each $p_{\rm T}$ bin among the multiplicity classes was considered as final value (it corresponds to the yellow highlighted region in Fig. 9.8).

Fig. 9.9 shows an example of the fraction of uncorrelated uncertainties with respect to the total systematic uncertainty in the case of the VII V0M class.

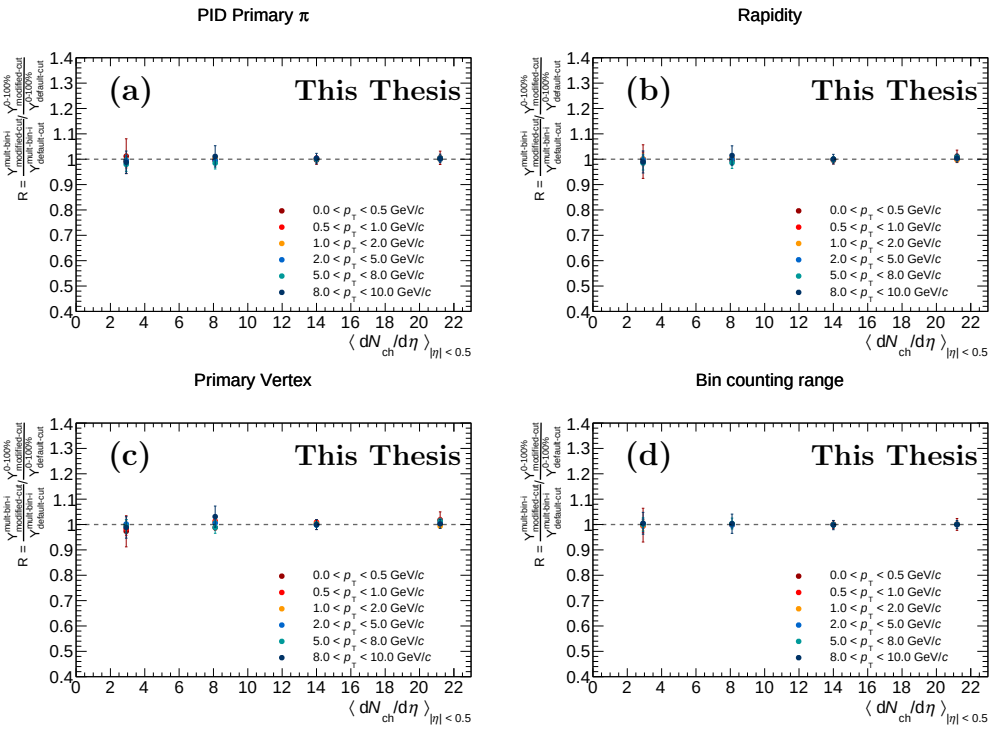

Figure 9.7: The R-factor computed for a variation on primary pion (**a**), K^0_s, (**b**), and primary vertex (**c**) selection criteria, and on the signal extraction parameters (**d**) as a function of charged-particle multiplicity in several p_T slices.

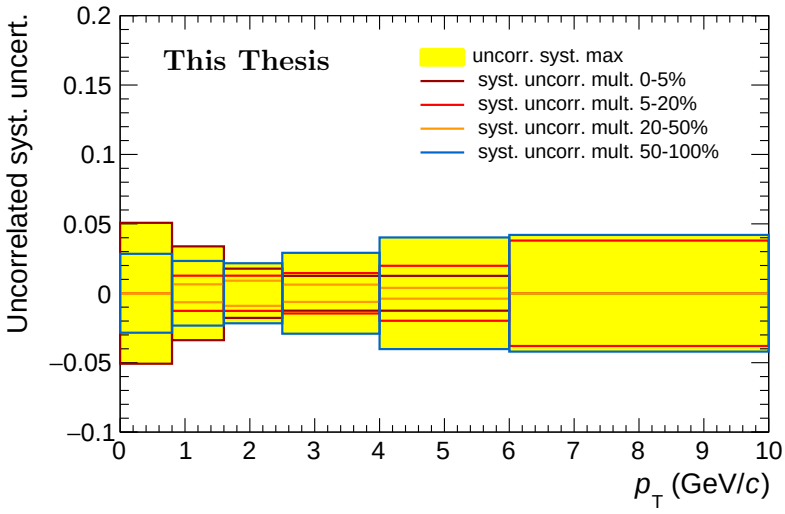

Figure 9.8: Uncorrelated uncertainties as a function of p_{T} in several multiplicity classes (colored lines). The yellow band represents the maximum value among all the multiplicity classes.

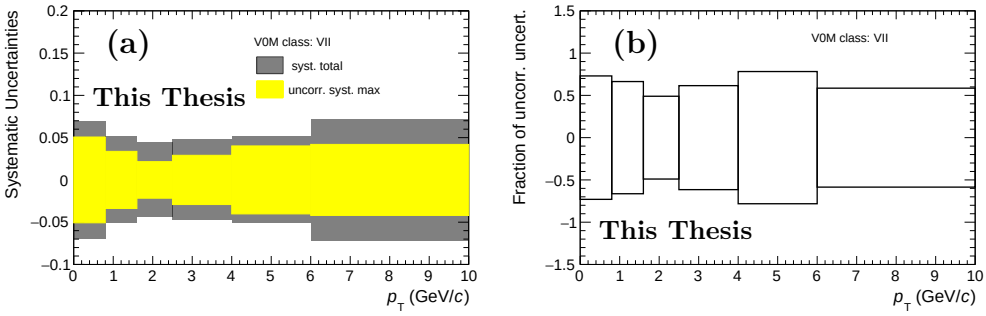

Figure 9.9: Uncorrelated uncertainties (left panel) and fraction of uncorrelated uncertainties as a function of p_{T} w.r.t total systematic uncertainty for the VII V0M class.

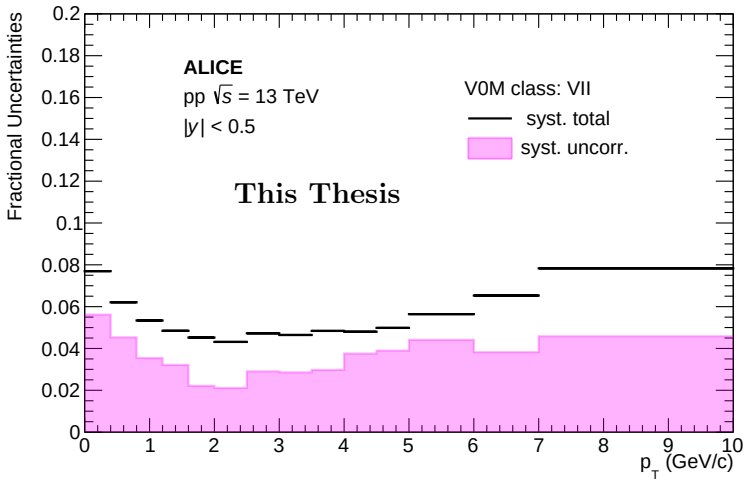

Figure 9.10: The p_{T} distribution of the systematic uncertainty in the VII V0M class. The shaded pink area is the uncertainty uncorrelated with multiplicity.

Then, in order to obtain the uncorrelated uncertainties in the p_{T} bins used in this analysis, the fractions of uncorrelated uncertainties of each multiplicity class, were multiplied by the corresponding total systematic uncertainties, computed with the default p_{T} bin sizes. In Fig. 9.10 the distribution obtained for the VII V0M class is shown. The shaded pink area represents the uncertainty uncorrelated with multiplicity.

Chapter 10

Results

10.1 Corrected p_{T} spectra

In order to obtain the corrected p_{T} spectra in the various multiplicity intervals, raw counts were corrected for:

1. BR: the decay Branching ratio for $\mathrm{K}^{*\pm} \rightarrow \pi^{\pm} + \mathrm{K}^{0}_{\mathrm{S}}$ (BR = 33.3 % i.e. $0.66 \times 0.5 = 0.33$);
2. ϵ_{rec}: the geometrical acceptance and detector efficiency;
3. $\mathrm{f_{SL}}$: signal-loss correction factor;
4. $\mathrm{f_{norm}}$: the efficiency of trigger selection for inelastic pp collisions [79];
5. $\mathrm{f_{vertex}}$: the signal loss introduced by the requirement to reconstruct a primary vertex [79].

For each multiplicity class the yield was then estimated using the following formula:

$$\frac{d^2N}{dydp_T} = \frac{Raw\,Counts}{N_{evt} \times BR \times \Delta y \times \Delta p_T} \frac{f_{SL}}{\epsilon_{rec}} \times f_{norm} \times f_{vertex} \tag{10.1}$$

Where $\mathrm{N_{evt}}$ is the number of accepted events, Δp_{T} is the transverse momentum step and Δy is the rapidity interval ($\Delta y = 1$).

The inelastic normalization factor $\mathrm{f_{norm}}$ takes into account how many true INEL>0 events are obtained with the kINT7 trigger. It can be written as:

$$f_{norm} = \frac{N^{Events}_{INT7|TrueINEL>0}}{N^{Events}_{TrueINEL>0}} \tag{10.2}$$

The factor f_{vertex} accounts how many good vertex events are obtained after the good vertex selection (SPD vertex-z resolution < 0.25 cm, z-position difference between track and SPD vertex < 0.5 cm). It can be written as:

$$f_{vertex} = \frac{N^{Events}_{Vertex|INT7|TrueINEL>0}}{N^{Events}_{TrueINEL>0}} \tag{10.3}$$

The values of f_{norm} and f_{vertex} considered are referred to the LHC16+17+18 periods and are listed in Tab. 10.1.

Table 10.1: f_{norm} and f_{vertex} values for LHC16+17+18 periods for each multiplicity interval.

V0M class	f_{norm}	f_{vertex}
I	0.99957	0.999886
II	0.999708	0.999906
III	0.99952	0.999858
IV + V	0.999528	0.999636
VI	0.99932	0.999465
VII	0.998658	0.99887
VIII	0.996589	0.997752
IX	0.987297	0.994484
X	0.885539	0.986729
INEL> 0	0.947794	0.993216

The obtained p_{T} spectra for $\mathrm{K}^{*\pm}$ and the ratios of these spectra to the inclusive one are shown in Fig. 10.1. The p_{T} distributions get harder with increasing multiplicity, passing from low to high multiplicity event classes. In addition for higher multiplicity classes the position of the peak at low p_{T} shifts towards higher momenta. This trend is qualitatively similar to the behaviour observed in heavy-ion collisions [12,13,21] and attributed to a collective radial expansion of the system (radial flow), although as seen in section 3.1.1 the colour reconnection mechanism seems to mimic collective-like effects in small systems [29]. The increasing trend is significant for $p_{\mathrm{T}} \lesssim 5$ Gev/c while for higher p_{T} values the spectral shape is the same for all multiplicity classes,

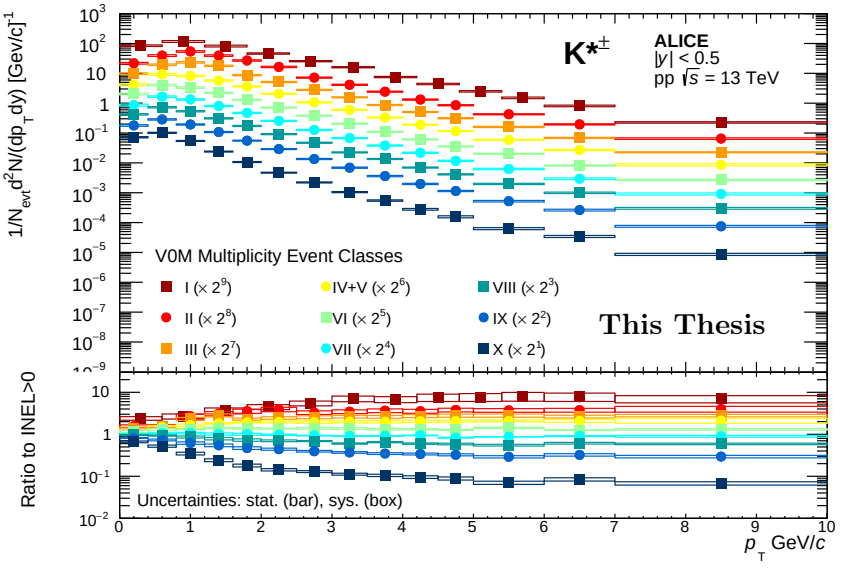

Figure 10.1: The $K^{*\pm}$ p_T spectra in pp collisions at $\sqrt{s} = 13$ TeV for the different multiplicity classes studied, scaled by the indicated factors. **Lower panel:** ratios of the p_T spectra to the INEL> 0 spectrum.

suggesting a low p_T dominant effect.
The results here reported have many qualitative similarities to those obtained for longer lived hadrons in pp collisions [38, 39], and are consistent with previous measurements of hadronic resonances in small collisions systems [17, 20, 41].

10.2 Integrated yield and mean p_T spectra

The corrected measured spectra are fitted with a Levy-Tsallis function, which describes both the exponential and power law shape of the spectra at low and high transverse momentum, in the fit range $0 < p_T < 10$ GeV/c.

$$\frac{d^2N}{dp_T dy} = p_T \frac{dN}{dy} \frac{(n-1)(n-2)}{nT[nT + m(n-2)]} \left(1 + \frac{\sqrt{m^2 + {p_T}^2} - m}{nT}\right)^{-n} \tag{10.4}$$

The integrated yield $\mathrm{d}N/\mathrm{d}y$ is obtained by integrating the spectra in the measured range and extrapolating to zero p_{T} and to higher p_{T} by the Levy-Tsallis function. Then the $\mathrm{d}N/\mathrm{d}y$ is defined as:

$$\frac{dN}{dy} = I_{hist} + I_{extrapolated} \tag{10.5}$$

where:

$$I_{hist} = \sum 2\pi p_{\mathrm{T}} f(p_{\mathrm{T}}, y) dp_{\mathrm{T}} \quad \text{and} \quad I_{extrapolated} = \int 2\pi f(p_{\mathrm{T}}, y) p_{\mathrm{T}} dp_{\mathrm{T}} \tag{10.6}$$

are computed in the measured range and in the extrapolated region, respectively. Similarly the the mean p_{T} ($\langle p_{\mathrm{T}} \rangle$) is defined as:

$$\langle p_{\mathrm{T}} \rangle = \frac{\sum 2\pi {p_{\mathrm{T}}}^2 f(p_{\mathrm{T}}, y) dp_{\mathrm{T}} + \int 2\pi f(p_{\mathrm{T}}, y) p_{\mathrm{T}}^2 dp_{\mathrm{T}}}{I_{hist} + I_{extrapolated}} \tag{10.7}$$

where $f(p_{\mathrm{T}}, y)$ is the invariant yield.
Usually, the systematic uncertainties have two parts: one coming from systematic uncertainties of the spectrum and a second originated from the extrapolation of the spectrum to the unmeasured regions. However due to the fact that the limits of the measured spectrum are (0, 10) GeV/c the $\mathrm{d}N/\mathrm{d}y$ and $\langle p_{\mathrm{T}} \rangle$ are estimated using only the measured points.

In Fig.10.2 the $\mathrm{d}N/\mathrm{d}y$ and the $\langle p_{\mathrm{T}} \rangle$ spectra for $\mathrm{K}^{*\pm}$ are shown as a function of charged-particle multiplicity density $\langle \mathrm{d}N_{ch}/\mathrm{d}\ \eta \rangle_{|\eta|<0.5}$, while in Tab. 10.2 the corresponding values are listed.

Table 10.2: $\mathrm{d}N/\mathrm{d}y$ and $\langle p_{\mathrm{T}} \rangle$ values for $\mathrm{K}^{*\pm}$ listed from low to high multiplicity.

V0M class	$\mathrm{d}N/\mathrm{d}y$ ± stat ± sys tot (sys uncorr)	$\langle p_{\mathrm{T}} \rangle$ ± stat ± sys tot (sys uncorr)
X	0.054910 ± 0.000539 ± 0.002304 (0.000978)	0.781689 ± 0.004455 ± 0.008365 (0.007206)
IX	0.089516 ± 0.001009 ± 0.004572 (0.001704)	0.959189 ± 0.006523 ± 0.013635 (0.009963)
VIII	0.120904 ± 0.001902 ± 0.006098 (0.002207)	1.037080 ± 0.009569 ± 0.013063 (0.009605)
VII	0.145327 ± 0.003283 ± 0.008260 (0.002823)	1.112470 ± 0.019037 ± 0.017776 (0.012314)
VI	0.186504 ± 0.003162 ± 0.011089 (0.003829)	1.167430 ± 0.014570 ± 0.018422 (0.012298)
IV+V	0.229539 ± 0.003517 ± 0.013824 (0.004432)	1.256380 ± 0.014034 ± 0.020782 (0.013755)
III	0.293048 ± 0.005224 ± 0.015898 (0.004667)	1.294870 ± 0.017345 ± 0.016203 (0.010241)
II	0.350060 ± 0.005117 ± 0.020961 (0.005311)	1.383670 ± 0.014948 ± 0.018734 (0.011228)
I	0.456782 ± 0.012000 ± 0.028567 (0.008318)	1.440800 ± 0.024477 ± 0.023573 (0.016124)

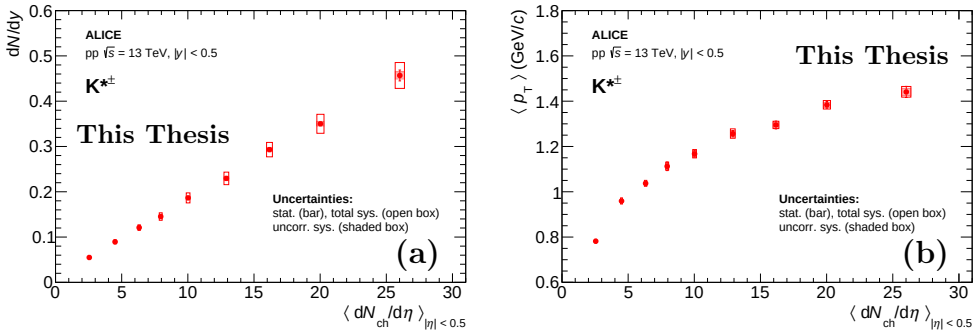

Figure 10.2: Integrated yields $\mathrm{d}N/\mathrm{d}y$ (**a**) and mean transverse momenta $\langle p_{\mathrm{T}} \rangle$ (**b**) for $\mathrm{K}^{*\pm}$ as a function of $\langle \mathrm{d}N_{ch}/\mathrm{d}\eta \rangle_{|\eta|<0.5}$. Bars represent statistical uncertainties, open boxes represent total systematic uncertainties, and shaded boxes are the systematic uncertainties uncorrelated with multiplicity.

10.2.1 Ratios of p_{T}-integrated particle yields

The ratio of resonance p_{T}-integrated yields to the production of their non-resonant hadronic states, is an important tool to verify the presence of a suppression in resonances production and its dependence on the system size. Figure 10.3 shows the $\mathrm{K}^{*\pm}/\mathrm{K}^{0}_{\mathrm{S}}$ ratio, where an intriguing decreasing trend is observed passing from low to high multiplicity pp collisions. The suppression is significant at 6.7σ level ($S = |Y_{high} - Y_{low}|/\sqrt{\sigma^2_{high} + \sigma^2_{low}}$) taking into account the fraction of systematic uncertainties uncorrelated with multiplicity (values are listed in Tab. 10.3). In heavy-ion collisions this indicates the dominance of re-scattering mechanism over the regeneration during the hadronic phase. Since a hadronic phase is not expected in pp collisions, it is still an open question if this decrease, observed also in small collision systems, can be related to the same mechanism.

Another interesting aspect to consider is the $\mathrm{K}^{*\pm}/\mathrm{K}^{0}_{\mathrm{S}}$ double ratio, i.e. the high multiplicity $\mathrm{K}^{*\pm}/\mathrm{K}^{0}_{\mathrm{S}}$ p_{T} spectrum divided by the low multiplicity one, with the $\mathrm{K}^{0}_{\mathrm{S}}$ p_{T} spectra obtained from the strange particle analysis in pp collisions at $\sqrt{s} = 13$ TeV [38]. As shown in Fig. 10.4 the ratios increase at low p_{T} and become flat for $p_{\mathrm{T}} \gtrsim 2.5$ GeV/c, with the $\mathrm{K}^{*\pm}/\mathrm{K}^{0}_{\mathrm{S}}$ ratio computed in the high multiplicity class (II) being smaller than the low multiplicity one (X). This behaviour is consistent with the results obtained from the K^{*0} analyses in pp [41] and Pb–Pb [42] collisions, as described in

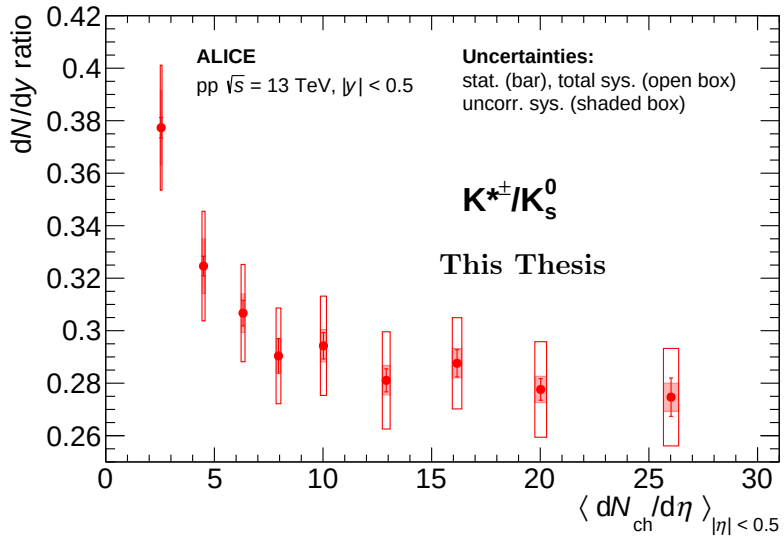

Figure 10.3: The $\mathrm{K}^{*\pm}/\mathrm{K}^{0}_{\mathrm{S}}$ ratios as a function of $\langle \mathrm{d}N_{ch}/\mathrm{d}\,\eta \rangle_{|\eta|<0.5}$.

Table 10.3: Values of the $\mathrm{d}N/\mathrm{d}y$ $\mathrm{K}^{*\pm}/\mathrm{K}^{0}_{\mathrm{S}}$ ratio listed from low to high multiplicity.

V0M class	$\mathrm{K}^{*\pm}/\mathrm{K}^{0}_{\mathrm{S}}$ ± stat ± sys tot (sys uncorr)
X	0.377335 ± 0.003877 ± 0.023816 (0.014246)
IX	0.324617 ± 0.003751 ± 0.020859 (0.010468)
VIII	0.306710 ± 0.004886 ± 0.018530 (0.007418)
VII	0.290407 ± 0.006602 ± 0.018232 (0.006143)
VI	0.294242 ± 0.005023 ± 0.018920 (0.006258)
IV+V	0.281069 ± 0.004387 ± 0.018521 (0.005591)
III	0.287574 ± 0.005173 ± 0.017380 (0.005623)
II	0.277607 ± 0.004115 ± 0.018202 (0.005065)
I	0.274678 ± 0.007307 ± 0.018573 (0.005400)

section 3.2. To verify the decrease in these ratios the middle panel of Fig. 10.4 shows the double ratio. It is consistent with unity for $p_{\mathrm{T}} \gtrsim 2.5$ GeV/c while for $p_{\mathrm{T}} \lesssim 2.5$ GeV/c the suppression from low to high-multiplicity collisions is appreciable. This is quantified in the lower panel where the significance of the deviations of the double ratio from unity is shown ($\sigma = |1 - R|/\Delta R$

where $R = classII/classX$). For $p_{\mathrm{T}} \lesssim 2$ GeV/c the deviation is measured at more than 3σ level. Since an important suppression at low p_{T} is considered in heavy-ion collisions as a signature of re-scattering effects, this evidence could be a hint of a hadronic phase in small collision systems too.

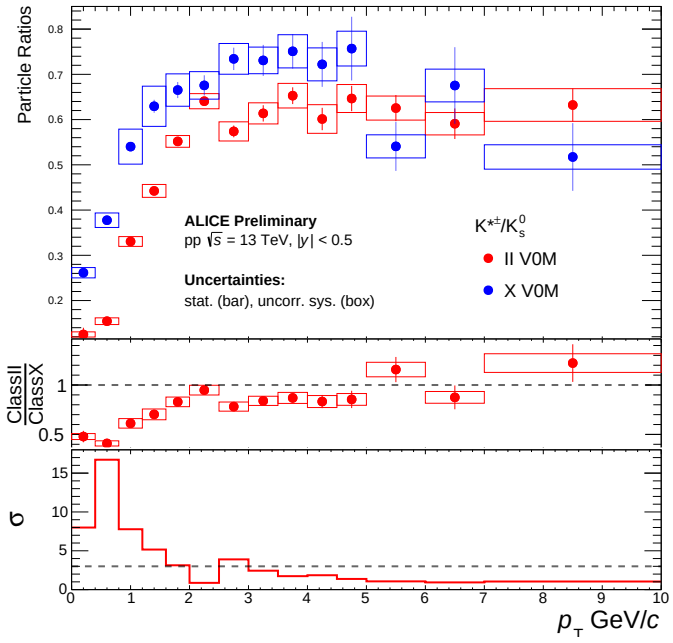

Figure 10.4: **Upper panel:** ratios of $\mathrm{K}^{*\pm}/\mathrm{K}^{0}_{\mathrm{S}}$ p_{T} spectra for low (X) and high (II) multiplicity classes. **Middle panel:** high multiplicity $\mathrm{K}^{*\pm}/\mathrm{K}^{0}_{\mathrm{S}}$ p_{T} spectrum divided by the low multiplicity one (double ratio). **Lower panel:** significance of the deviation of the double ratio from unit. The dashed black line indicates a deviation at the 3σ level. Bars represent the statistical uncertainties, while boxes represent the part of the systematic uncertainty that is uncorrelated between the multiplicity classes.

10.3 Comparison with K^{*0} results and model predictions

Results on $K^{*\pm}$ multiplicity dependent analysis in pp collisions at $\sqrt{s} = 13$ TeV (this work) are compared with those obtained from the K^{*0} multiplicity dependent analysis for the same collision system and energy as well as with results from several model predictions computed for K^{*0} measurements [41]. In Fig. 10.5 a comparison between the $K^{*\pm}$ and K^{*0} p_T spectra is shown. A very good agreement is observed between the charged and neutral $K^*(892)$ spectra. In Fig. 10.6 the ratios of $K^{*\pm}/K^{*0}$ as a function of p_T for the different multiplicity classes are also shown.

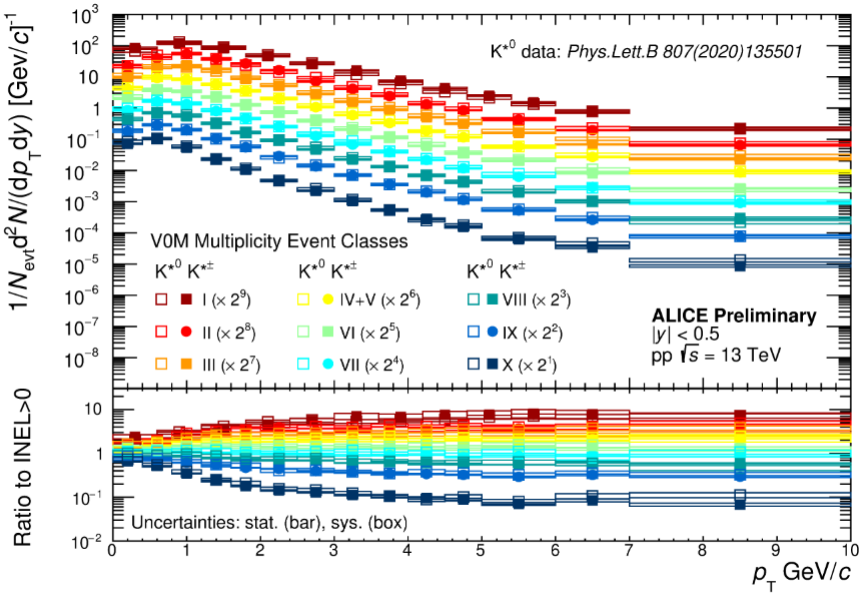

ALI-PREL-503116

Figure 10.5: The $K^{*\pm}$ and K^{*0} p_T spectra in pp collisions at $\sqrt{s} = 13$ TeV for different multiplicity classes studied, scaled by the indicated factors. **Lower panel:** ratios of the p_T spectra to the INEL> 0 spectrum.

Fig. 10.7 shows the $K^{*\pm}$ and K^{*0} comparison for the p_T-integrated yields and the mean p_T spectra, together with predictions from different event generators (PYTHIA6, Perugia 2011 tune [26]; PYTHIA8, Monash 2013 tune both with and without colour reconnection [27, 28]; EPOS-LHC [32];

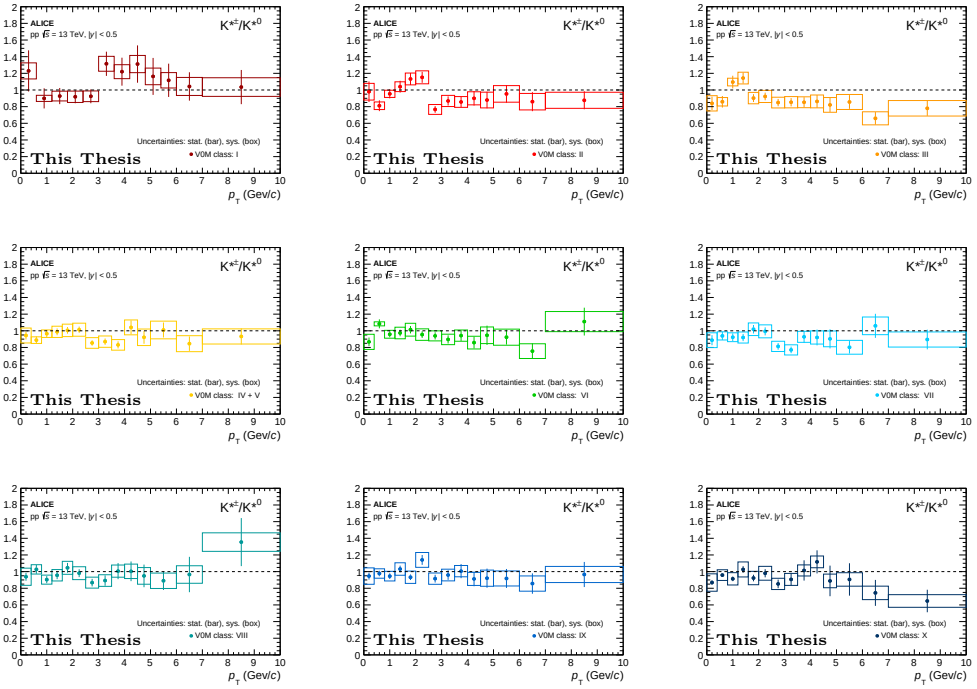

Figure 10.6: The $K^{*\pm}/K^{*0}$ ratios as a function of p_T for the different multiplicity classes.

and DIPSY[1] [80]) computed for K^{*0} results. The slightly differences in the $\langle dN_{ch}/d\eta \rangle_{|\eta|<0.5}$ values are due to the different data periods analyzed (the K^{*0} analysis was performed on the LHC15f data sample). The results obtained are fully in agreement within the systematic and statistical uncertainties. In addition, as expected, $K^{*\pm}$ results exhibit lower systematic uncertainties than K^{*0} one. Therefore $K^{*\pm}$ data not only confirm but also improve the previous results, fulfilling the goal of this analysis.
For the dN/dy values EPOS-LHC and PYTHIA8 without colour reconnection provide the best description, while the other PYTHIA calculations and DIPSY tend to overestimate the K^* results.

[1]DIPSY (Dipole evolution in Impact Parameter Space and rapiditY) is a MC event generator where PDFs are replaced with dipole evolution. Two dipole cascades are generated from the projectile and the target. In each step of the dipole cascade evolution, a dipole can split into two new dipoles. DIPSY offers a different view on MPIs, built on Mueller dipole model [81], where multiple interactions produce loops of dipole chains.

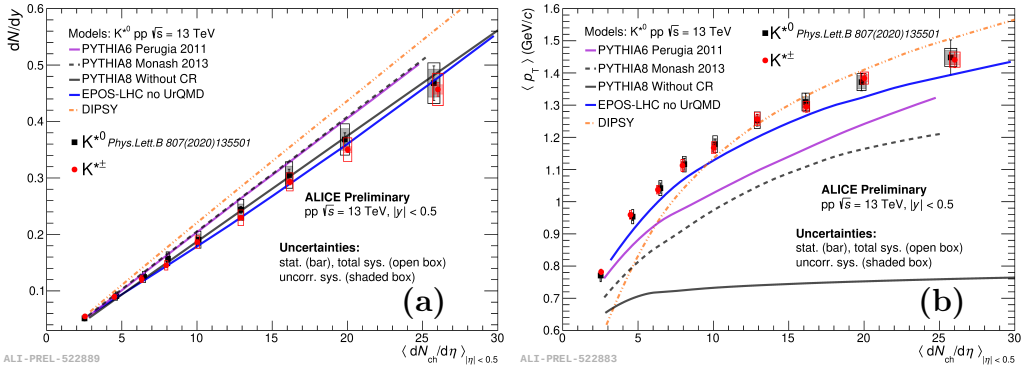

Figure 10.7: Integrated yields $\mathrm{d}N/\mathrm{d}y$ (**a**) and mean transverse momenta $\langle p_{\mathrm{T}} \rangle$ (**a**) for $\mathrm{K}^{*\pm}$ and K^{*0} as a function of $\langle \mathrm{d}N_{ch}/\mathrm{d}\eta \rangle_{|\eta|<0.5}$. The $\langle \mathrm{d}N_{ch}/\mathrm{d}\eta \rangle_{|\eta|<0.5}$ values used for the K^{*0} analysis are referred to the LHC15 period [38]. Bars represent statistical uncertainties, open boxes represent total systematic uncertainties, and shaded boxes are the systematic uncertainties uncorrelated with multiplicity. The measurements are also compared to several model predictions [26–28, 32, 80].

Regarding the mean p_{T} results PYTHIA8 without colour reconnection provides an almost constant $\langle p_{\mathrm{T}} \rangle$ with increasing event multiplicity. Turning on the colour reconnection there is a better qualitative agreement, even though the calculations are underestimated as well as for PYTHIA6. EPOS-LHC predictions are consistent with the measured values although they are slightly underestimated. Instead DIPSY describes a more pronounced increase in mean p_{T} from low to high multiplicity than data.
In Tables 10.4 and 10.5 the values of $\mathrm{d}N/\mathrm{d}y$ and $\langle p_{\mathrm{T}} \rangle$ for $\mathrm{K}^{*\pm}$ and K^{*0} with the corresponding uncertainties are listed.

Table 10.4: The dN/dy values for $K^{*\pm}$ and K^{*0} listed from low to high multiplicity.

V0M class	$K^{*\pm}$ dN/dy ± stat ± sys tot (sys uncorr)	K^{*0} dN/dy ± stat ± sys tot (sys uncorr)
X	0.054910 ± 0.000539 ± 0.002304 (0.000978)	0.051357 ± 0.000862 ± 0.004657 (0.002061)
IX	0.089516 ± 0.001009 ± 0.004572 (0.001704)	0.090864 ± 0.001856 ± 0.007362 (0.003848)
VIII	0.120904 ± 0.001902 ± 0.006098 (0.002207)	0.124788 ± 0.003357 ± 0.009941 (0.005893)
VII	0.145327 ± 0.003283 ± 0.008260 (0.002823)	0.156851 ± 0.004219 ± 0.012307 (0.006861)
VI	0.186504 ± 0.003162 ± 0.011089 (0.003829)	0.190673 ± 0.004289 ± 0.014954 (0.010283)
IV+V	0.229539 ± 0.003517 ± 0.013824 (0.004432)	0.243606 ± 0.005848 ± 0.018615 (0.010261)
III	0.293048 ± 0.005224 ± 0.015898 (0.004667)	0.305269 ± 0.010304 ± 0.023407 (0.015699)
II	0.350060 ± 0.005117 ± 0.020961 (0.005311)	0.368211 ± 0.011749 ± 0.027729 (0.019155)
I	0.456782 ± 0.012000 ± 0.028567 (0.008318)	0.467922 ± 0.030565 ± 0.035911 (0.024693)

Table 10.5: The $\langle p_{\mathrm{T}} \rangle$ values for $K^{*\pm}$ and K^{*0} listed from low to high multiplicity.

V0M class	$K^{*\pm}$ $\langle p_{\mathrm{T}} \rangle$ ± stat ± sys tot (sys uncorr)	K^{*0} $\langle p_{\mathrm{T}} \rangle$ ± stat ± sys tot (sys uncorr)
X	0.781689 ± 0.004455 ± 0.008365 (0.007206)	0.770652 ± 0.007544 ± 0.019076 (0.007982)
IX	0.959189 ± 0.006523 ± 0.013635 (0.009963)	0.953443 ± 0.011417 ± 0.022007 (0.012578)
VIII	1.037080 ± 0.009569 ± 0.013063 (0.009605)	1.042160 ± 0.015877 ± 0.023255 (0.011207)
VII	1.112470 ± 0.019037 ± 0.017776 (0.012314)	1.116660 ± 0.018128 ± 0.024168 (0.012790)
VI	1.167430 ± 0.014570 ± 0.018422 (0.012298)	1.178730 ± 0.016169 ± 0.026217 (0.016781)
IV+V	1.256380 ± 0.014034 ± 0.020782 (0.013755)	1.253250 ± 0.018564 ± 0.025609 (0.013384)
III	1.294870 ± 0.017345 ± 0.016203 (0.010241)	1.309700 ± 0.027029 ± 0.027682 (0.016598)
II	1.383670 ± 0.014948 ± 0.018734 (0.011228)	1.371670 ± 0.027038 ± 0.026295 (0.020754)
I	1.440800 ± 0.024477 ± 0.023573 (0.016124)	1.448180 ± 0.054298 ± 0.028220 (0.021886)

Figure 10.8 shows the p_{T} integrated yield ratios of $K^{*\pm}$ and K^{*0} to K^0_S. The decreasing trend passing from low to high multiplicity pp collisions, already outlined by the K^{*0} analysis [41] has been confirmed by the $K^{*\pm}$ results with smaller systematic uncertainties. In addition the $K^{*\pm}/K^0_S$ suppression measured considering the values at lowest and highest multiplicity is verified even accounting for the systematic uncertainties, improving the precision of previous K^{*0} results. Indeed the K^{*0}/K^0_S ratio in the highest multiplicity class was below the low multiplicity value at the 2.7σ level, while the same calculation applied to the $K^{*\pm}/K^0_S$ ratio provides a significance at the 6.7σ level (considering only the multiplicity-uncorrelated uncertainties). The values are listed in Tables 10.6. Data are compared with the same models considered for the dN/dy and the $\langle p_{\mathrm{T}} \rangle$. In addition the canonical statistical model with the strangeness saturation factor (γ_S-CSM) [82] is also included. EPOS-LHC gives the best agreement with the measured data, well reproducing the decreasing trend. PYTHIA6 , PYTHIA8 (both with and without the colour reconnection), and DIPSY tend to overestimate the ratio at high

multiplicities and exhibit a fairly flat trend. The γ_S-CSM model describes a moderated suppression overestimating high multiplicity data.

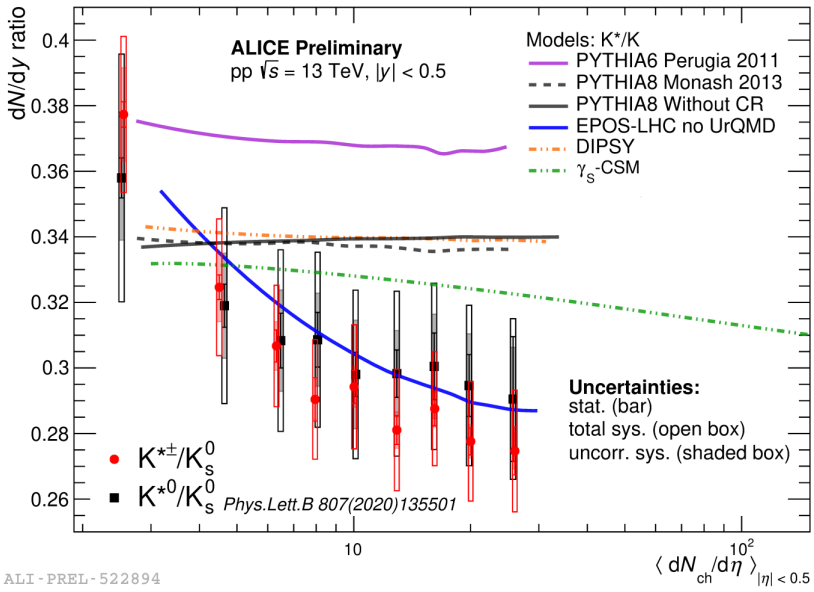

Figure 10.8: Ratios of $\mathrm{K}^{*\pm}/\mathrm{K}^0_\mathrm{S}$ and $\mathrm{K}^{*0}/\mathrm{K}^0_\mathrm{S}$ as a function of multiplicity. Bars represent statistical uncertainties, open boxes represent total systematic uncertainties, and shaded boxes are the systematic uncertainties uncorrelated with multiplicity. The measurements are also compared to several model predictions [26–28, 32, 80, 82].

Table 10.6: Values of the $\mathrm{d}N/\mathrm{d}y$ $\mathrm{K}^{*\pm}/\mathrm{K}^0_\mathrm{S}$ and $\mathrm{K}^{*0}/\mathrm{K}^0_\mathrm{S}$ ratios listed from low to high multiplicity.

V0M class	$\mathrm{K}^{*\pm}/\mathrm{K}^0_\mathrm{S}$ ± stat ± sys tot (sys uncorr)	$\mathrm{K}^{*0}/\mathrm{K}^0_\mathrm{S}$ ± stat ± sys tot (sys uncorr)
X	0.377335 ± 0.003877 ± 0.023816 (0.014246)	0.357966 ± 0.006103 ± 0.037780 (0.018987)
IX	0.324617 ± 0.003751 ± 0.020859 (0.010468)	0.318999 ± 0.006573 ± 0.029856 (0.016051)
VIII	0.306710 ± 0.004886 ± 0.018530 (0.007418)	0.308348 ± 0.008348 ± 0.027701 (0.015460)
VII	0.290407 ± 0.006602 ± 0.018232 (0.006143)	0.308613 ± 0.008343 ± 0.026687 (0.014204)
VI	0.294242 ± 0.005023 ± 0.018920 (0.006258)	0.298036 ± 0.006737 ± 0.025711 (0.016569)
IV+V	0.281069 ± 0.004387 ± 0.018521 (0.005591)	0.298269 ± 0.007214 ± 0.025146 (0.013175)
III	0.287574 ± 0.005173 ± 0.017380 (0.005623)	0.300482 ± 0.010169 ± 0.025371 (0.015956)
II	0.277607 ± 0.004115 ± 0.018202 (0.005065)	0.294649 ± 0.009431 ± 0.024487 (0.015796)
I	0.274678 ± 0.007307 ± 0.018573 (0.005400)	0.290522 ± 0.019017 ± 0.024505 (0.015795)

Chapter 11

Conclusions

Results of $K^{*\pm}$ resonance production at mid-rapidity in pp collisions at $\sqrt{s} = 13$ TeV in different multiplicity classes have been reported here.
For $p_T \lesssim 5$ GeV/c $K^{*\pm}$ differential p_T spectra get harder with increasing multiplicity, while for higher p_T values the same spectral shape can be noticed for all multiplicity classes. This behaviour is qualitatively similar to the trend observed in heavy-ion collisions, where this effect is attributed to the collective expansion of the fireball. However, in small collision systems, colour re-connection mechanism can mimic flow-like patterns.
Both the p_T-integrated yields and the mean transverse momenta were computed as a function of the charged-particle multiplicity density and exhibit an approximately linear increase from low to high multiplicity.
Considering the p_T-integrated particle yields ratios, a suppression of the $K^{*\pm}/K^0_S$ at a $\sim 7\sigma$ level is observed passing from low to high multiplicity pp collisions. This is the first evidence of a clear K^*/K suppression measured in pp collisions. The $K^{*\pm}/K^0_S$ multiplicity evolution is consistent with the hypothesis of the re-scattering of the short-lived resonances decay daughters typical of heavy-ion collisions and therefore seems to suggest the presence of a non zero lifetime hadronic phase in small systems too. However EPOS-LHC without the UrQMD hadronic afterburner is able to reproduce fairly well the measured decreasing trend. This is explained as a consequence of core/corona interplay with the formation of a mini plasma in pp collision due to multiple partonic interactions (see section 3.1.2).
The study on the ratio of the high multiplicity $K^{*\pm}/K^0_S$ differential p_T distribution to the low multiplicity one (double ratio) helped to quantify the decrease in the particle ratios. For $p_T \lesssim 2$ GeV/c the $K^{*\pm}/K^0_S$ double ratio

deviates from unity by more than 3σ suggesting a low p_{T} dominant process, as in the case of rescattering effect.
A comparison with the neutral K^{*} results was evaluated too. The yields of both $\mathrm{K}^{*\pm}$ and K^{*0} were computed in the same p_{T} bins and multiplicity classes. A very good agreement, within the statistical and systematic uncertainties, was found. Moreover $\mathrm{K}^{*\pm}$ results show lower systematic uncertainties than K^{*0} measurements. This is an important statement as previous K^{*0} results have been corroborated and improved thanks to the higher precision reached, fulfilling the goal of this analysis.

Bibliography

[1] F. Wilczek, *"Quantum field theory"*. Rev. Mod. Phys. 71 (1999) S85
https://doi.org/10.1103/RevModPhys.71.S85

[2] H. W. Lin and H. B. Meyer, *"Lattice QCD for Nuclear Physics"*. Springer Cham, Volume 889 (2015)
https://doi.org/10.1007/978-3-319-08022-2

[3] T. Iritani et al., *"Lattice study on QCD-like theory with exact center symmetry"*. JHEP, 11 (2015) 159
https://doi.org/10.1007/JHEP11(2015)159

[4] K. Adcox et al., *"Formation of dense partonic matter in relativistic nucleus–nucleus collisions at RHIC: Experimental evaluation by the PHENIX Collaboration"*. Nuclear Physics A, 757 (2005) 184-283
DOI:10.1016/j.nuclphysa.2005.03.086

[5] P. Foka and M. A. Janik, *"An overview of experimental results from ultra-relativistic heavy-ion collisions at the CERN LHC: Bulk properties and dynamical evolution"*. Reviews in Physics, 1 (2016) 154-171
https://doi.org/10.1016/j.revip.2016.11.002.

[6] P. Koch, Müller et al., *"From strangeness enhancement to quark–gluon plasma discovery"*. Int. J. Mod. Phys. A, 32 (2017) 1730024
https://doi.org/10.1142/S0217751X17300241

[7] ALICE Collaboration: J. Adam et al., *"Enhanced production of multi-strange hadrons in high-multiplicity proton–proton collisions"*. Nat. Phys., 13 (2017) 535–539
https://doi.org/10.1038/nphys4111

[8] ALICE Collaboration: B. B. Abelev et al., *"Centrality dependence of π, K, p production in Pb–Pb collisions at $\sqrt{s_{\rm NN}} = 2.76$ TeV"*. Nat. Phys., 13 (2017) 535–539
https://doi.org/10.1103/PhysRevC.48.2462

[9] ALICE Collaboration: B. B. Abelev et al., *"K^0_S and Λ production in Pb–Pb collisions at $\sqrt{s_{\rm NN}}$" = 2.76 TeV"*. Phys. Rev. Lett., 111 (2013) 222301
https://doi.org/10.1103/PhysRevLett.111.222301

[10] ALICE Collaboration: B. B. Abelev et al., *"$K^*(892)^0$ and $\phi(1020)$ production in Pb–Pb collisions at $\sqrt{s_{\rm NN}} = 2.76$ TeV"*. Phys. Rev. C, 91 (2015) 024609
https://doi.org/10.1103/PhysRevC.91.024609

[11] D. Sahu et al., *"Role of event multiplicity on hadronic phase lifetime and QCD phase boundary in ultrarelativistic collisions at energies available at the BNL Relativistic Heavy Ion Collider and CERN Large Hadron Collider"*. Phys. Rev. C, 101 (2020) 014902
https://doi.org/10.1103/PhysRevC.101.014902

[12] ALICE Collaboration: S. Acharya et al., *"Production of the $\rho(770)^0$ meson in pp and Pb–Pb collisions at $\sqrt{s_{NN}} = 2.76$ TeV "*. Phys. Rev. C, 99 (2019) 064901
https://doi.org/10.1103/PhysRevC.99.064901

[13] ALICE Collaboration: S. Acharya et al., *"Evidence of rescattering effect in Pb–Pb collisions at the LHC through production of $K^*(892)^0$ and $\phi(1020)$ mesons"*. Phys. Lett. B, 802 (2020) 135225
https://doi.org/10.1016/j.physletb.2020.135225

[14] ALICE Collaboration: J. Adam et al., *"Production of $K^*(892)^0$ and $\phi(1020)$ in p–Pb collisions at $\sqrt{s_{\rm NN}} = 5.02$ TeV"*. Eur. Phys. J. C, 76 (2016) 245
https://doi.org/10.1140/epjc/s10052-016-4088-7

[15] ALICE Collaboration: B. Abelev et al., *"Production of $K^*(892)^0$ and $\phi(1020)$ in pp collisions at $\sqrt{s} = 7$ TeV"*. Eur. Phys. J. C, 72 (2012) 2183
https://doi.org/10.1140/epjc/s10052-012-2183-y

[16] ALICE Collaboration: B. Abelev et al., *"Production of* $\Sigma(1385)^{\pm}$ *and* $\Xi(1530)^{0}$ *in proton–proton collisions at* $\sqrt{s} = 7$ *TeV"*. Eur. Phys. J. C, 75 (2015) 1
https://doi.org/10.1140/epjc/s10052-014-3191-x

[17] ALICE Collaboration: D. Adamová et al., *"Production of* $\Sigma(1385)^{\pm}$ *and* $\Xi(1530)^{0}$ *in p–Pb collisions at* $\sqrt{s_{\rm NN}} = 5.02$ *TeV"*. Eur. Phys. J. C, 77 (2017) 389
https://doi.org/10.1140/epjc/s10052-017-4943-1

[18] ALICE Collaboration: K. Aamodt et al., *"*$\Sigma(1385)^{\pm}$ *resonance production in Pb–Pb collisions at* $\sqrt{s_{\rm NN}} = 5.02$ *TeV"*; arXiv:2205.13998 [nucl-ex] (2022)
https://doi.org/10.48550/arXiv.2205.13998

[19] STAR Collaboration: B. Abelev et al., *"Strange Baryon Resonance Production in* $\sqrt{s_{NN}} = 200$ GeV $p+p$ *and* Au+Au *Collisions"*. Eur. Phys. J. C, 77 (2017) 389
https://doi.org/10.1103/PhysRevLett.97.132301

[20] ALICE Collaboration: S. Acharya et al., *"Measurement of* $\Lambda(1520)$ *production in pp collisions at* $\sqrt{s} = 7$ *TeV and p–Pb collisions at* $\sqrt{s_{\rm NN}} = 5.02$ *TeV"*. Eur. Phys. J. C, 80, 160 (2020)
https://doi.org/10.1140/epjc/s10052-020-7687-2

[21] ALICE Collaboration: S. Acharya et al., *"Suppression of* $\Lambda(1520)$ *resonance production in central Pb–Pb collisions at* $\sqrt{s_{NN}} = 2.76$ *TeV"*. Phys.Rev. C, 99 (2019) 024905
https://doi.org/10.1103/PhysRevC.99.024905

[22] A. Knospe et al., *"Hadronic resonance production and interaction in partonic and hadronic matter in EPOS3 with and without the hadronic afterburner UrQMD"*. Phys. Rev. C, 93 (2016) 014911
https://doi.org/10.1103/PhysRevC.93.014911

[23] T. Sjostrand et al., *"PYTHIA 6.4 Physics and Manual"*. JHEP, 05 (2006) 026
https://doi.org/10.1088/1126-6708/2006/05/026

[24] *https://pythia.org/download/talks/SjostrandDesy11.pdf*

[25] B. Andersson et al., *"PartonFragmentation and String Dynamics"*. Phys. Rept., 97 (1983) 31–145
https://doi.org/10.1016/0370-1573(83)90080-7

[26] P. Skands, *"Tuning Monte Carlo generators: the Perugia tunes"*. Phys. Rev. D, 82 (2010) 074018
https://doi.org/10.1103/PhysRevD.82.074018

[27] P. Skands et al., *"Tuning PYTHIA 8.1: the Monash 2013 tune"*. Eur. Phys. J. C, 74 (2014) 3024
https://doi.org/10.1140/epjc/s10052-014-3024-y

[28] R. Acconcia et al., *"Resonance suppression from color reconnection"*. Phys. Rev. D, 97 (2018) 036010
https://doi.org/10.1103/PhysRevD.97.036010

[29] A. Ortiz Velasquez et al., *"Color Reconnection and Flowlike Patterns in pp Collisions"*. Phys. Rev. Lett., 111 (2013) 042001
https://doi.org/10.1103/PhysRevLett.111.042001

[30] K. Werner et al., *"Parton ladder splitting and the rapidity dependence of transverse momentum spectra in deuteron-gold collisions at the BNL Relativistic Heavy Ion Collider"*. Phys. Rev. C, 74 (2006) 044902
https://doi.org/10.1103/PhysRevC.74.044902

[31] H. J. Drescher et al., *"Parton-based Gribov–Regge theory"*. Phys. Rep., 350 (2001) 93
https://doi.org/10.1016/S0370-1573(00)00122-8

[32] T. Pierog et al., *"EPOS LHC: Test of collective hadronization with data measured at the CERN Large Hadron Collider"*. Phys. Rev. C, 92 (2015) 034906
https://doi.org/10.1103/PhysRevC.92.034906

[33] A. Knospe et al., *"Hadronic resonance production and interaction in partonic and hadronic matter in the EPOS3 model with and without the hadronic afterburner UrQMD"*. Phys. Rev. C, 93 (2016) 014911
https://doi.org/10.1103/PhysRevC.93.014911

[34] S. A. Bass et al., *"Microscopic Models for Ultrarelativistic Heavy Ion Collisions"*. Prog. Part. Nucl. Phys., 41 (1998) 225
https://doi.org/10.1016/S0146-6410%2898%2900058-1

[35] M. Bleicher et al., *"Relativistic Hadron-Hadron Collisions in the Ultra-Relativistic Quantum Molecular Dynamics Model (UrQMD)"*. J. Phys. G, 25 (1999) 1859
https://doi.org/10.1088/0954-3899/25/9/308

[36] ALICE Collaboration: B. Abelev et al., *"Long-range angular correlations on the near and away side in p–Pb collisions at* $\sqrt{s_{\rm NN}} = 5.02$ *TeV"*. Phys. Lett. B, 719 (2013) 29
https://doi.org/10.1016/j.physletb.2013.01.012

[37] ALICE Collaboration: J. Adam et al., *"Enhanced production of multi-strange hadrons in high-multiplicity proton–proton collisions"*. Nature Phys., 13 (2017) 535
https://doi.org/10.1038/nphys4111

[38] ALICE Collaboration: S. Acharya et al., *"Multiplicity dependence of (multi-)strange hadron production in proton–proton collisions at* $\sqrt{s} =$ 13 *TeV"*. Eur. Phys. J. C, 80 (2020) 167
https://doi.org/10.1140/epjc/s10052-020-7673-8

[39] ALICE Collaboration: S. Acharya et al., *"Multiplicity dependence of* π*, K, and p production in pp collisions at* $\sqrt{s} = 13$ *TeV"*. Eur. Phys. J. C, 80 (2020) 693
https://doi.org/10.1140/epjc/s10052-020-8125-1

[40] ALICE Collaboration: B. Abelev et al., *"Multiplicity dependence of pion, kaon, proton and lambda production in p–Pb collisions at* $\sqrt{s_{\rm NN}} =$ 5.02 *TeV"*. Phys. Lett. B, 728 (2014) 25-38
https://doi.org/10.1016/j.physletb.2013.11.020.

[41] ALICE Collaboration: S. Acharya et al., *"Multiplicity dependence of* $K^*(892)^0$ *and* $\phi(1020)$ *production in pp collisions at* $\sqrt{s} = 13$ *TeV"*. Phys. Lett. B, 807 (2020) 135501
https://doi.org/10.1016/j.physletb.2020.135501.

[42] ALICE Collaboration: B. Abelev et al., *"*$K^*(892)^0$ *and* $\phi(1020)$ *production in Pb–Pb collisions at* $\sqrt{s_{NN}} = 2.76$ *TeV"*. Phys. Rev. C 91 (2015)

024609
https://link.aps.org/doi/10.1103/PhysRevC.91.024609.

[43] L. Rossi and O. Brüning, *"The High Luminosity Large Hadron Collider"*. Chapter 1: *"Introduction to the HL-LHC Project*, 1-17 (2015)
https://www.worldscientific.com/doi/abs/10.1142/9789814675475_0001

[44] D. Colella, *"Upgrade of the ALICE experiment beyond LHC Run 3"* arXiv:2206.13247 [hep-ex] (2022)
https://doi.org/10.48550/arXiv.2206.13247

[45] ALICE Collaboration: K. Aamodt et al., *"The ALICE experiment at the CERN LHC"*. JINST, 3 (2008) 8002
DOI: 10.1088/1748-0221/3/08/s08002

[46] ALICE Collaboration: K. Aamodt et al., *"Performance of the ALICE experiment at the CERN LHC"*, Int. J. Mod. Phys. A, 29 (2014) 1430044
https://doi.org/10.1142/S0217751X14300440

[47] ALICE Collaboration: G. Dellacasa et al., *"ALICE Inner Tracking System (ITS): Technical Design Report*, Technical Design Report ALICE, CERN, Geneva, 1999.

[48] ALICE Collaboration: G. Dellacasa et al., *"ALICE Time Projection Chamber: Technical Design Report*, Technical Design Report ALICE, CERN, Geneva, 1999.

[49] E. Hellbär, *"The ALICE TPC: Optimization of the Performance in Run 2 and Developments for the Future"*, PoS LHCP2019 (2019) 240
https://doi.org/10.22323/1.350.0240

[50] ALICE Collaboration: G. Dellacasa et al., *"ALICE Time-Of-Flight system (TOF): Technical Design Report"*, Technical Design Report ALICE, CERN, Geneva, 2000.

[51] ALICE Collaboration: P. Cortese et al., *"ALICE forward detectors: FMD, T0 and V0: Technical Design Report"*, Technical Design Report ALICE, CERN, Geneva, 2004.

[52] ALICE Collaboration: K. Aamodt et al., *"Centrality Dependence of the Charged-Particle Multiplicity Density at Midrapidity in Pb—Pb Collisions at* $\sqrt{s_{\mathrm{NN}}} = 2.76$ *TeV"*, Phys. Rev. Lett., 106 (2011) 032301 https://doi.org/10.1103/PhysRevLett.106.032301

[53] ALICE Collaboration: B. Abelev et al., *"Measurement of visible cross sections in proton–lead collisions at* $\sqrt{s_{\mathrm{NN}}} = 5.02$ *TeV in van der Meer scans with the ALICE detector"*. JINST, 9 (2014) 1100 https://doi.org/10.1088/1748-0221/9/11/P11003

[54] ALICE Collaboration: G. Dellacasa et al., *"ALICE Zero Degree Calorimeter (ZDC): Technical Design Report"*, Technical Design Report ALICE, CERN, Geneva, 1999.

[55] ALICE Collaboration: S. Acharya et al., *"Centrality determination in heavy ion collisions"* ALICE-PUBLIC-2018-011.

[56] *https://alice-figure.web.cern.ch/node/11516*

[57] ALICE Collaboration: J. Adam et al., *"Pseudorapidity and transverse-momentum distributions of charged particles in proton–proton collisions at* $\sqrt{s} = 13$ *TeV"*. Phys. Lett. B, 753 (2016) 319-329 https://doi.org/10.1016/j.physletb.2015.12.030

[58] ALICE Collaboration: B. Abelev et al., *"Centrality determination of Pb–Pb collisions at* $\sqrt{s_{\mathrm{NN}}} = 2.76$ *TeV"*. Phys. Rev. C, 88 (2013) 044909 https://doi.org/10.1103/PhysRevC.88.044909

[59] ALICE Collaboration: P. Cortese et al., *"Technical Design Report of the Computing"*, Technical Design Report ALICE, CERN, Geneva, 2005.

[60] I.C. Legrand et al., *"MonALISA: an agent based, dynamic service system to monitor, control and optimize grid based applications"*. Computing in High Energy Physics and Nuclear Physics, (2004) 907 DOI:10.5170/CERN-2005-002.907

[61] R. Brun and F. Rademakers, *"ROOT: An object oriented data analysis framework"*. Nucl. Instrum. Meth. A, 389 (1997) 81–86 https://doi.org/10.1016/S0168-9002(97)00048-X

[62] A. Badalà et al., *"Full 3D Event-by-Event Vertex Reconstruction in ALICE by Pixel Layers"*. ALICE-INT-2001-26 (2001)

[63] P. Billoir, *"Track fitting with multiple scattering: A new method"*. Nucl. Instrum. Meth. A, 225 (1984) 352
https://doi.org/10.1016/0167-5087(84)90274-6

[64] M. Ivanov et al. *"Track reconstruction in high density environment"*. Nucl. Instrum. Meth. A, 566 (2006) 70-74
https://doi.org/10.1016/j.nima.2006.05.029

[65] ALICE Collaboration: S. Acharya et al., *"Measurement of $K^*(892)^{\pm}$ production in inelastic pp collisions at the LHC"*. Phys. Lett. B, 828 (2022) 137013
https://doi.org/10.1016/j.physletb.2022.137013

[66] R.L. Workman et al., *"Particle Data Group"*,Prog. Theor. Exp. Phys. (2022) 083C01
https://pdg.lbl.gov/#home

[67] ALICE Collaboration: J. Adam et al., *"Pseudorapidity and transverse-momentum distributions of charged particles in proton–proton collisions at $\sqrt{s} = 13$ TeV"*. Phys. Lett. B, 753 (2016) 319-329
https://doi.org/10.1016/j.physletb.2015.12.030

[68] STAR Collaboration: J. Adams et al., *"K(892)* resonance production in Au+Au and p+p collisions at $\sqrt{s_{NN}} = 200$ GeV at STAR"*. Phys. Rev. C, 71 (2005) 064902
https://doi.org/10.1103/PhysRevC.71.064902

[69] A. G. Knospe, *"Hadronic Resonances in Heavy-Ion Collisions at ALICE"*. EPJ Web of Conferences, 36 (2012) 00013
DOI: 10.1051/epjconf/20123600013

[70] G.E. Brown and M. Rho, *"On the manifestation of chiral symmetry in nuclei and dense nuclear matter"*. Phys. Rep., 363 (2002) 85
https://doi.org/10.1016/S0370-1573(01)00084-9

[71] R. Rapp et al., *"The Chiral Restoration Transition of QCD and Low Mass Dileptons"*. SpringerMaterials, Landolt-Börnstein - Group I Elementary Particles, Nuclei and Atoms 23 (2010), (Relativistic Heavy Ion

Physics)
https://doi.org/10.1007/978-3-642-01539-7_6

[72] E. Fragiacomo, *"Hadronic resonances in pp and PbPb with Alice"*. PoS(EPS-HEP 2013), 174 (2014)
doi = 10.22323/1.180.0174

[73] A. Knospe, *"An overview of resonance measurements at the ALICE experiment"*. EPJ Web of Conferences, 117 (2016) 03002
doi = 10.1051/epjconf/201611703002

[74] R. Brun et al., *"GEANT3"*. CERN-DD-EE-84-1, 1987
https://cds.cern.ch/record/1119728

[75] *https://twiki.cern.ch/twiki/bin/view/ALICE/AliDPGtoolsTrackSystematicUncertaintyBookkeping?rev=18*

[76] *https://twiki.cern.ch/twiki/bin/view/ALICE/PWG2Resonances#Material_budget_and_hadronic_int*

[77] R. Barlow, *"Systematic Errors: facts and fictions"*; arXiv:hep-ex/0207026v1[hep-ex](2002)
https://doi.org/10.48550/arXiv.hep-ex/0207026

[78] M. Floris and F. Fionda, *"Multiplicity dependent analysis of (multi-)strange hadron production in pp collisions at* $\sqrt{s}$ *= 13 TeV"*
https://alice-notes.web.cern.ch/system/files/notes/analysis/478.

[79] *https://indico.cern.ch/event/1001718/contributions/4218507/attachments/2183582/3689068/210203_Resonance_BHLIM.pdf*

[80] C. Flensburg et al., *"Inclusive and Exclusive observables from dipoles in high energy collisions"*. J. High Energy Phys., 8 (2011) 103
https://doi.org/10.1007/JHEP08(2011)103

[81] A.H. Mueller and B. Patel, *"Single and Double BFKL Pomeron Exchange and a Dipole Picture of High Energy Hard Processes"*. Nucl. Phys. B, 425 (1994) 471-488
https://doi.org/10.1016/0550-3213%2894%2990284-4

[82] V. Vovchenko et al., *"Canonical statistical model analysis of p–p, p–Pb, and Pb–Pb collisions at energies available at the CERN Large Hadron Collider"*. Phys. Rev. C, 100 (2019) 054906
https://doi.org/10.1103/PhysRevC.100.054906